

MULTISCALE CHARACTERIZATION AND MODELING OF PROGRESSIVE FAILURE  
IN NANO-GRAPHENE REINFORCED  
CARBON/EPOXY COMPOSITES

by

ABHISHEK KUMAR

SAMIT ROY, COMMITTEE CHAIR

MARK E. BARKEY  
VINU UNNIKRISHNAN  
ANWARUL HAQUE  
KIM LACKEY

A DISSERTATION

Submitted in partial fulfillment of the requirements  
for the degree of Doctor of Philosophy  
in the Department of Aerospace Engineering and Mechanics  
in the Graduate School of  
The University of Alabama

TUSCALOOSA, ALABAMA

2016

Copyright Abhishek Kumar 2016  
ALL RIGHTS RESERVED

## ABSTRACT

This dissertation studies the dispersion of nano graphene platelets in thermoset epoxy polymers for improving the mechanical and hygrothermal properties of nano composites and carbon fiber laminates. Barrier properties of graphene were investigated experimentally by adding 0.1-3 weight percentage of nano graphene to EPON 862 polymer and an analytical model for moisture diffusion in presence of nano graphene was derived assuming time-dependent diffusivity and moisture boundary conditions. Experimental studies were conducted for characterizing the fracture properties of 0.1 and 0.5 weight percentage nano graphene reinforced EPON 862 polymer in comparison to the unreinforced polymer. Pure Mode I, mixed mode and pure Mode II fracture experiments were performed. Remarkable improvement in fracture toughness across all modes was observed.

Hydrogen passivation of graphene was employed to improve dispersion of nano graphene in epoxy. Graphene alignment was studied under an alternating current electric field. Mode I delamination experiments were conducted on unidirectional carbon fiber laminates with the polymer phase reinforced with small weight percentage of nano graphene. Significant improvements in initiation fracture energy and resistance to crack propagation was observed in nano graphene reinforced laminates.

A theory that accounts for ductile to brittle transition in failure mode was developed to explain the nano scale toughness improvements observed in experiments. An analytical model for determining nano graphene size and orientation for maximum toughness enhancement

depending on structural loading was derived and implemented in MATLAB. A hierarchical multiscale modeling technique was used to synergistically couple three different length regimes, nano scale (Molecular Dynamics), micro scale (Generalized Method of Cells) and macro scale (Finite Element Analysis), to capture the physics and length scale effects in a general structural problem (e.g. Open Hole Tension specimen). This work lays the foundation for the use of nano graphene composites for structural light weighting in future aerospace and automobile applications.

## DEDICATION

This dissertation is dedicated to my family and friends who were always confident that I had it in me to achieve this milestone. I am really thankful for their support and help through this journey and making it one of the most valuable experiences of my life.

## LIST OF ABBREVIATIONS AND SYMBOLS

TGDDM	Tetraglycidyl 4,4'-diaminodiphenylmethane
PEEK	Polyether Ether Ketone
PB	Poly Butylene
ABS	Acrylonitrile Butadiene Styrene
PLA	Poly Lactic Acid
MWCNTs	Multi Walled Carbon Nano Tubes
SWCNT	Single walled Carbon Nano Tube
PMMA	Poly methyl methacrylate
PS	Polystyrene
PVA	Poly vinyl alcohol
DMF	Dimethylformamide
PU	Polyurethane
MMT	Montmorillonite
$K_{IC}$	Mode I critical stress intensity factor
$G_{IC}$	Mode I critical strain energy release rate
DWCNTs	Double walled CNTs
CVD	Chemical Vapor Deposition
UTS	Ultimate tensile strength
wt%	Weight percent

VARTM	Vacuum Assisted Resin Transfer Molding
NGP	Nano-graphene platelets
$T_g$	Glass transition temperature
TVD	Time Varying Diffusivity
TVC	Time Varying Concentration
$C$	Moisture concentration
$T$	Temperature
$\mu(t)$	Chemical potential of vapor
$\zeta$	Aspect ratio of platelets
CT	Compact tension
kV	Kilo volts
AC	Alternating current
$K_{IIc}$	Mode II critical stress intensity factor
$B^*$	Effective elastic stiffness tensor

## ACKNOWLEDGMENTS

I am pleased to have this opportunity to thank all my colleagues, friends, and faculty members who have helped me with this research project. I am indebted to Dr. Samit Roy, my advisor, for being immensely helpful for the four years of my research and guiding me every step of the way. I would also like to thank all of my committee members, Mark Barkey, Vinu Unnikrishnan, Anwarul Haque and Kim Lackey for their invaluable input, inspiring questions, and support of both the dissertation and my academic progress. I would like to thank Dr. Barkey for his guidance on experimental analysis and Dr. Lackey for her help with microscopy analysis and for always being there when I needed guidance. I acknowledge the support of this work by the NASA Aeronautical Sciences NRA, Contract NNX11AI32A, with Dr. Brett Bednarcyk as Technical Monitor.

This research would not have been possible without the support of my friends and fellow graduate students. I am grateful to my colleagues Priyank Upadhyay, Avinash Reddy Akepati, Ankit Srivastav, Shibo Li and Pruthul Kokkada Ravindranath for always lending a helping hand during experiments and motivating me throughout this research. I am thankful to Dr. Trupti Kotbage for her help with characterization studies of graphene for improving dispersions in polymer. I am grateful to my friend and fellow graduate student Shoeib Shaik, for his help with Atomic Force Microscopy and expert guidance on alignment of graphene. Finally I thank my family for always believing in me and their support during the course of this dissertation.

## CONTENTS

ABSTRACT .....	ii
DEDICATION .....	iv
LIST OF ABBREVIATIONS AND SYMBOLS .....	v
ACKNOWLEDGMENTS .....	vii
LIST OF TABLES .....	xiii
LIST OF FIGURES .....	xv
CHAPTER 1. INTRODUCTION .....	1
<b>1.1 Methods for Processing Nanocomposites and Dispersion of nano carbon fillers</b> .....	<b>3</b>
<b>1.2 Carbon nano materials</b> .....	<b>5</b>
<i>1.2.1 Nano Clay</i> .....	5
<i>1.2.2 Carbon Nano Tubes (CNTs)</i> .....	7
<i>1.2.3 Graphene</i> .....	10
CHAPTER 2. MODELING OF ANOMALOUS MOISTURE DIFFUSION IN NANOGRAPHENE REINFORCED THERMOSET POLYMERS .....	15
<b>2.1 Summary</b> .....	<b>15</b>
<b>2.2 Experimental section</b> .....	<b>18</b>
<b>2.3 Modeling of diffusion in nanocomposite</b> .....	<b>19</b>
<i>2.3.1 Diffusion with Boundary conditions and Diffusivity of time-varying type</i> .....	19
<i>2.3.2 Diffusion Path Tortuosity model</i> .....	22

2.3.3 Model description .....	23
2.3.4 Constant boundary condition solution.....	24
2.3.5 Time-varying Prony series boundary condition solution.....	24
2.3.6 Development of model solution.....	25
2.3.7 Evaluation of diffusivity coefficients .....	25
2.3.8 Model development using fminsearch function in Matlab.....	26
<b>2.4 Results and Discussion.....</b>	<b>27</b>
2.4.1 Diffusion Model Assumptions .....	27
2.4.2 Model Benchmarking and Uptake Prediction.....	27
<b>CHAPTER 3. CHARACTERIZATION OF MODE I FRACTURE PROPERTIES OF NANOGRAFENE REINFORCED EPON 862 THERMOSET POLYMER SYSTEM .....</b>	<b>32</b>
<b>3.1 Summary.....</b>	<b>32</b>
<b>3.2 Experimental Section.....</b>	<b>33</b>
3.2.1 Materials .....	33
3.2.2 Dispersion of NGP.....	33
3.2.3 Curing cycle and specimen preparation .....	34
3.2.4 Testing.....	34
<b>3.3 Results and Discussion.....</b>	<b>36</b>
3.3.1 Unaged Set Results .....	37
3.3.2 Aged set results .....	44
<b>CHAPTER 4. STUDIES ON THE DISPERSION AND ALIGNMENT OF NANOGRAFENE IN EPOXY POLYMER .....</b>	<b>51</b>
<b>4.1 Summary.....</b>	<b>51</b>
<b>4.2 Materials and Methods.....</b>	<b>51</b>

4.2.1 <i>Materials</i> .....	51
4.2.2 <i>Hydrogen passivation setup</i> .....	52
4.2.3 <i>Dispersion in ethanol</i> .....	52
<b>4.3 Microscopy Study</b> .....	52
4.3.1 <i>Optical microscopy study</i> .....	52
4.3.2 <i>TEM study</i> .....	53
<b>4.4 Analysis of hydrogen passivated NGPs</b> .....	56
<b>4.5 Graphene alignment study</b> .....	60
4.5.1 <i>Devices for initial testing</i> .....	62
4.5.2 <i>Graphene dispersion and electric field application</i> .....	63
4.5.3 <i>Results</i> .....	63
 CHAPTER 5. CHARACTERIZATION OF MIXED MODE FRACTURE PROPERTIES OF NGP REINFORCED EPOXY AND MODE I DELAMINATION PROPERTIES OF CARBON FIBER/NGP/ EPOXY UNIDIRECTIONAL LAMINATE .....	
<b>5.1 Summary</b> .....	76
<b>5.2 Experimental section</b> .....	77
5.2.1 <i>Materials</i> .....	77
5.2.2 <i>NGP hydrogen passivation and dispersion</i> .....	77
5.2.3 <i>Specimen preparation</i> .....	77
5.2.3.1 <i>Mixed mode specimens</i> .....	77
5.2.3.2 <i>DCB testing specimens</i> .....	78
5.2.4 <i>Test setup and experimental data analysis</i> .....	79
5.2.4.1 <i>Mixed mode testing</i> .....	79
5.2.4.2 <i>DCB testing</i> .....	80

<b>5.3 Results and Discussion</b> .....	82
5.3.1 <i>Mixed mode test results</i> .....	82
5.3.2 <i>DCB test results</i> .....	84
CHAPTER 6. MECHANISMS FOR TOUGHNESS ENHANCEMENT IN POLYMERS AND COMPOSITES AT THE NANO SCALE .....	
	88
<b>6.1 Summary</b> .....	88
<b>6.2 Nano scale fracture derivation for Mixed-Mode loading</b> .....	91
6.2.1 <i>Critical nano particle length calculation</i> .....	91
6.2.2 <i>NGP wt% calculation</i> .....	94
6.2.3 <i>Damage evolution</i> .....	96
6.2.4 <i>Computation in Matlab</i> .....	98
6.2.5 <i>Case study: Compact Tension test</i> .....	99
CHAPTER 7. MULTISCALE MODELING OF NANO GRAPHENE/CARBON FIBER REINFORCED EPON 862 COMPOSITES .....	
	104
<b>7.1 Summary</b> .....	104
<b>7.2 Atomistic Level Analysis using Molecular Dynamics (MD)</b> .....	106
<b>7.3 Micro-mechanics Level Analysis using the Generalized Method of Cells</b> .....	107
<b>7.4 Nano scale averaging law</b> .....	110
<b>7.5 Three-Dimensional Ply-Level Analysis Using Finite Element Analysis and Multiscale coupling</b> .....	112
<b>7.6 Results from Multi scale simulation of Open-hole Tension specimen</b> .....	113
CHAPTER 8. SUMMARY AND FUTURE WORK .....	120

REFERENCES .....	123
APPENDIX.....	134

## LIST OF TABLES

<b>2.1</b> Tortuosity factors for baseline and NRPC specimens used for modeling.....	28
<b>2.2</b> Relaxation parameters ( $\beta_r$ ) assumed for modeling.....	28
<b>2.3</b> Diffusion coefficients for baseline and NRPC specimens obtained from diffusion model.....	31
<b>3.1</b> Fracture Load - Critical Displacement Data Comparison.....	38
<b>3.2</b> Average Fracture Toughness ( $K_{IC}$ ) Comparison.....	39
<b>3.3</b> Average Fracture Energy ( $G_{IC}$ ) Comparison .....	40
<b>3.4</b> Average Surface Roughness (Ra) comparison .....	43
<b>3.5</b> Saturation moisture uptake comparison for <i>aged</i> CT specimens.....	46
<b>3.6</b> Average $K_{IC}$ Comparison of aged CT specimens .....	48
<b>3.7</b> Average $G_{IC}$ Comparison of aged CT specimens .....	49
<b>4.1</b> BJH and BET analysis using $N_2$ adsorption isotherm for different temperatures .....	57
<b>4.2</b> Crystallite size calculation for different temperature HP-NGPs.....	59
<b>5.1</b> Calibration parameters used for mixed mode data analysis.....	83
<b>5.2</b> Pure mode II critical stress intensity factors .....	84
<b>5.3</b> Mix mode critical stress intensity factors for $\Psi=57^\circ$ and $\Psi=38^\circ$ mixed mode cases.....	84
<b>5.4</b> Initiation fracture toughness of laminates at 2 inch crack length .....	87
<b>5.5</b> Propagation Fracture toughness of laminates after 1 inch crack propagation .....	87

<b>7.1</b> RUC level properties of subcells .....	116
<b>7.2</b> Stress based failure criterion for baseline and reinforced matrices.....	116

## LIST OF FIGURES

<b>1.1</b> Composite usage in (a) Boeing 787 Dreamliner [1] (b) Airbus 350-XWB [2] .....	3
<b>1.2</b> Chemical structure of nano clays [adapted from 35] .....	6
<b>1.3</b> Structure of (a) SWCNT (b) MWCNT (adapted from [53]).....	8
<b>1.4</b> Molecular Structure of graphene (adapted from [85]) .....	11
<b>2.1</b> Moisture absorption manufactured specimens (a) Baseline (b) 1 wt% NRPC .....	19
<b>2.2</b> Experimental moisture absorption profiles for baseline and NRPC specimens as a function of time.....	20
<b>2.3</b> Dispersion analyses of nanographene platelets for 3 wt% NRPC specimens using TEM.....	20
<b>2.4</b> Tortuous diffusion path due to presence of NGPs in the polymer matrix .....	22
<b>2.5</b> Regression model fits for baseline, 0.5, 1, 3 wt% NGP compared with experimental data .....	30
<b>2.6</b> Regression model predictions for 0.1, 2 wt% NGP compared with experimental data.....	30
<b>2.7</b> Diffusivity variation predicted by model for baseline and NRPC specimens .....	31
<b>3.1</b> (A) Schematic of the supplied nano graphene platelet (NGP) stack (adapted from [117]), Molecular structure (B) EPON 862 (C) DETDA(adapted from [119]) .....	33
<b>3.2</b> CT samples after curing process (a) Baseline (b) 0.1 wt% and (c) 0.5 wt% NGP.....	35

<b>3.3 SEM image showing a) Pre-crack created by tapping b) Magnified pre-crack tip .....</b>	<b>35</b>
<b>3.4 CT test setup (a) baseline (b) 0.1 wt% NGP.....</b>	<b>35</b>
<b>3.5 TEM image showing nanographene platelet dispersion in (A) 0.1 wt%, (B) 0.5 wt% NGP reinforced samples.....</b>	<b>36</b>
<b>3.6 Experimental Load-displacement plot comparison for <i>unaged</i> specimens .....</b>	<b>39</b>
<b>3.7 SEM image showing fracture surface roughness comparison (A) baseline (B) 0.1 wt% (C) 0.5 wt% NGP.....</b>	<b>41</b>
<b>3.8 AFM fracture surface roughness study (A) baseline (B) 0.1 wt% (C) 0.5 wt% NGP .....</b>	<b>42</b>
<b>3.9 SEM image showing graphene platelet pull-out in 0.1 wt% NGP fracture surface.....</b>	<b>43</b>
<b>3.10 SEM image showing void formations in 0.1 wt% NGP fracture surface.....</b>	<b>44</b>
<b>3.11 Comparison of moisture uptake of CT specimens .....</b>	<b>45</b>
<b>3.12 Experimental load-displacement curves for <i>aged</i> CT specimens.....</b>	<b>47</b>
<b>3.13 Comparison of averaged load-displacement curves of <i>unaged</i> &amp; <i>aged</i> CT specimens .....</b>	<b>48</b>
<b>3.14 Normalized <math>K_{IC}</math> comparison of <i>unaged</i> &amp; <i>aged</i> CT specimens .....</b>	<b>49</b>
<b>3.15 Normalized <math>G_{IC}</math> comparison of <i>unaged</i> &amp; <i>aged</i> CT specimens .....</b>	<b>50</b>
<b>4.1 Optical micrograph of drop casted HP-NGPs in ethanol at 4x magnification .....</b>	<b>53</b>
<b>4.2 Optical micrograph of drop casted HP-NGPs in ethanol at 10x magnification .....</b>	<b>54</b>
<b>4.3 Optical micrograph of drop casted HP-NGPs in ethanol at 40x magnification .....</b>	<b>54</b>
<b>4.4 TEM micrograph of unpassivated and passivated NGP in ethanol (2 micron scale).....</b>	<b>55</b>

<b>4.5</b> TEM micrograph of unpassivated and passivated NGP in ethanol (500 nm scale) .....	55
<b>4.6</b> N <sub>2</sub> adsorption-desorption isotherms for different temperature HP-NGPs.....	56
<b>4.7</b> XRD analysis of different temperature HP-NGPs .....	58
<b>4.8</b> G and D bands obtained using Raman spectroscopy of HP-NGPs.....	60
<b>4.9</b> Devices fabricated for initial alignment.....	63
<b>4.10</b> Alignment using silver electrodes at 100V (100, 500, 1000 Hz) for 60 minutes .....	64
<b>4.11</b> Alignment using silver electrodes at 150V (100, 500, 1000 Hz) for 60 minutes .....	65
<b>4.12</b> Alignment using silver electrodes at 200V (100, 500, 1000 Hz) for 60 minutes .....	66
<b>4.13</b> Alignment using aluminum electrodes at 100V (100, 500, 1000 Hz) for 60 minutes .....	67
<b>4.14</b> Alignment using aluminum electrodes at 150V (100, 500, 1000 Hz) for 60 minutes .....	68
<b>4.15</b> Alignment using aluminum electrodes at 200V (100, 500, 1000 Hz) for 60 minutes .....	68
<b>4.16</b> Alignment using steel electrodes at 100V (100, 500, 1000 Hz) for 60 minutes .....	69
<b>4.17</b> Alignment using steel electrodes at 150V (100, 500, 1000 Hz) for 60 minutes .....	69
<b>4.18</b> Alignment using steel electrodes at 200V (100, 500, 1000 Hz) for 60 minutes .....	70
<b>4.19</b> Alignment using steel electrodes at 100V, 150V, 200V (100 Hz) in 20 minutes.....	70
<b>4.20</b> Graphene column formation and agglomeration at 40kV/m for aluminum electrodes .....	71

<b>4.21</b> Comparison of alignment using different electrodes at 100V, 100 Hz for 60 minutes.....	71
<b>4.22</b> Comparison of alignment using different electrodes at 100V, 500 Hz for 60 minutes.....	72
<b>4.23</b> Comparison of alignment using different electrodes at 100V, 1000 Hz in 60 minutes .....	72
<b>4.24</b> Comparison of alignment using different electrodes at 150V, 100 Hz for 60 minutes.....	73
<b>4.25</b> Comparison of alignment using different electrodes at 150V, 500 Hz for 60 minutes.....	73
<b>4.26</b> Comparison of alignment using different electrodes at 150V, 1000 Hz for 60 minutes.....	74
<b>4.27</b> Comparison of alignment using different electrodes at 200V, 100 Hz for 60 minutes.....	74
<b>4.28</b> Comparison of alignment using different electrodes at 200V, 500 Hz for 60 minutes.....	75
<b>4.29</b> Comparison of alignment using different electrodes at 200V, 1000 Hz in 60 minutes .....	75
<b>5.1</b> (a) Mixed mode test specimen (b) DCB test specimen.....	80
<b>5.2</b> Mixed mode test setup .....	81
<b>5.3</b> DCB test setup .....	81
<b>5.4</b> Load displacement plots of mixed mode results for mode mix angle (a) $\psi = 89.5^\circ$ (Mode II), (b) $\psi = 57^\circ$ , and (c) $\psi = 38^\circ$ .....	83
<b>5.5</b> Normalized mixed mode fracture envelop.....	85
<b>5.6</b> Load displacement plot comparison for baseline, 0.1 wt% and 0.5 wt% HP-NGP reinforced epoxy laminates (DCB specimens) .....	86
<b>5.7</b> Crack propagation captured using camera for post processing in DCB testing.....	87

<b>5.8</b> R curves for baseline and NGP reinforced epoxy laminates from DCB testing.....	87
<b>6.1</b> Crack length effect at the nanoscale .....	90
<b>6.2</b> Schematic of the nano particle optimization for fracture toughness enhancement .....	91
<b>6.3</b> RUC of NGP in polymer matrix .....	95
<b>6.4</b> Schematic of crack propagation and damage evolution in presence of NGP .....	96
<b>6.5</b> Platelet length distributions.....	98
<b>6.6</b> Cumulative probability of platelet length distribution.....	98
<b>6.7</b> Schematic of the CT specimen with nano platelet.....	100
<b>6.8</b> Critical nano particle length variation with nano particle orientation .....	102
<b>6.9</b> Principal axis variation with nano particle orientation .....	103
<b>7.1</b> Schematic of a nano-micro-macro hierarchical multiscale model.....	105
<b>7.2</b> Length scales involved in multi-scale modeling.....	106
<b>7.3</b> MAC/GMC RUCs (a) Doubly periodic (b) triply periodic .....	108
<b>7.4</b> Nano scale RVE with nano-graphene platelet .....	111
<b>7.5</b> Euler rotations for local to global transformation.....	112
<b>7.6</b> Micro-macro coupling (MAC-GMC/Abaqus).....	113
<b>7.7</b> OHT FEA model and boundary conditions in laminate).....	114
<b>7.8 (a)</b> Load displacement plot for multiscale OHT simulation for various cases <b>(b)</b> Magnified view at load drop .....	118
<b>7.9</b> von Mises stress contour for individual lamina in IM7/EPON 862 OHT simulation .....	119

## CHAPTER 1

### INTRODUCTION

Composites form the backbone of structural research due to recent advances in materials research and usage. Polymer composites, with the polymer being the matrix phase, have gained popularity due to their capability of cutting costs while pushing performance limits beyond what is possible using metallic structures. The use of polymer composites encompasses fields of aerospace, aviation, automotive and biomedical technology. Boeing and Airbus have made remarkable progress in incorporating more than 50% polymer based composites in their new fleet of aircraft [1,2]. BMW Inc. launched its new i3 series which boasts a full carbon fiber reinforced plastic body, cutting an enormous amount of weight of the model [3]. Usage of polymer matrix composites in prosthetics to treat amputations has shown considerable potential and promise [4]. However, the brittle nature of thermoset polymer matrices puts it at a great disadvantage [5,6]. The high cross link density of a thermoset polymer matrix after curing leads to a reduction in fracture toughness of the composite, which is unacceptable for “damage-tolerant” structural designs due to low resistance to crack growth [7,8]. Argon et al suggested addition of a second reinforcement phase like rubbery particles to brittle polymer matrices which can cavitate and debond prior to plastic flow, for delaying the brittle nature of the matrix [5]. NASA used selective insertion of rubber particles larger than fiber diameter in HX 205 and F185 thermoset epoxy matrices, which led to successful energy absorption due to crack tip blunting, shear deformations and plastic flow [9,10]. Similarly, nano-silica particles mixed with tetraglycidyl 4,4'-diaminodiphenylmethane (TGDDM) epoxy resin gave two-fold increases in

fracture toughness, for about 10 wt% of nano-silica [11]. Although, some significant advances were made in this area, the relatively large wt% of the particles used limit their incorporation in structures due to composite processing issues, such as high resin viscosity leading to poor fiber wet-out.

To tackle this problem, carbon based nano materials have been sought as an alternative additive to the resin matrix. Carbon's inherent properties of being inert over a wide temperature range and resistance to corrosive reagents makes it highly suitable for its application in polymer composites [12]. Nano carbon fillers are extremely attractive to manufacturers due to their length scale and aspect ratio, which provides enormous increase in surface areas compared to micro sized fillers. Several carbon materials have been recognized and are being researched extensively for 'multifunctional' applications, which include carbon nanotubes, nano graphene, nano clay, and carbon nano fibers. Multifunctionality of these components ranges from high specific strength, stiffness, remarkable thermal and electrical properties and chemical stability. Two different epoxy systems have been researched extensively: thermoset and thermoplastic systems. Thermoset systems are pre-polymers in a soft solid or viscous state that changes irreversibly into an infusible, insoluble polymer network by curing. Thermosets are an easy manufacturing option due to their low cost of processing and high molecular weights. Thermoplastics on the other hand are reusable, meaning they can change reversibly from solid to a liquid state. Most commonly used thermoset systems include but are not limited to Polypropylene, Nylon, Polyether Ether Ketone (PEEK), Poly Butylene (PB), Acrylonitrile Butadiene Styrene (ABS), polyester, and polystyrene.

The macro scale properties of polymer based nanocomposites depend on thermodynamic factors which include interfacial energy compatibility of the polymer with the nano-filler phase, and

nano-scale dispersion and distribution of the filler, which in turn depends on the aspect ratio of the filler, dispersion techniques, time of mixing and applied shear, bonding between the filler and the matrix and the volume fraction of the filler, etc. [13-15]. Full advantage of the fillers can only be taken by considering all of the processing factors mentioned above, which would lead to better load transfer between the polymer matrix and the filler surface, leading to superior mechanical properties.

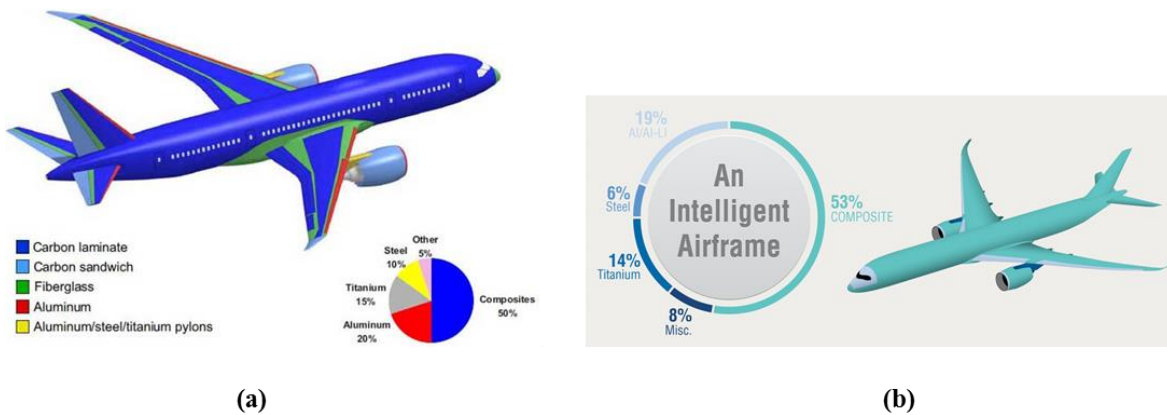


**Figure 1.1** Composite usage in (a) Boeing 787 Dreamliner [1] (b) Airbus 350-XWB [2]

### 1.1 Methods for Processing Nanocomposites and Dispersion of nano carbon fillers

Proper dispersion of nano fillers in the epoxy matrix is one of the most crucial steps in forming high quality polymer composites. Agglomerations of nano filler in the epoxy matrix can lead to problems such as void formation, inadequate curing of the epoxy, shear thinning, and viscosity buildup of the epoxy [16]. Optimal dispersion helps in increasing the mechanical interlocking between the epoxy and the nano filler and induces better performance. Many techniques have been used for efficient dispersion including melt blending, solvent casting and in situ polymerization [17-19]. Melt blending is an industrial process generally used with thermoplastics where a twin screw extruder heats the epoxy and nano filler mixture to form a liquid melt. Solvent casting refers to premixing the nano particles in a solvent using ultra-sonication, shear

mixing or magnetic stirring, and then mixing in the polymer and evaporating the solvent for final curing. In situ polymerization refers to direct dispersion of the nanoparticle in the monomer and curing of the dispersed solution through polymerization and crosslinking. Bao et al used melt blending to disperse graphene sheets in Poly Lactic Acid (PLA) which showed good dispersion of the graphene sheets [20]. Jin et al showed good dispersion of Multi Walled Carbon Nano Tubes (MWCNTs) even at 26 wt% loading in PMMA matrix using melt blending [21]. Gorga et al used twin screw extrusion to form successfully aligned Single walled Carbon Nano Tube (SWCNT) and MWCNT composites with PMMA epoxy [22]. Problems exist with melt blending which can range from increased viscosity of the melt due to the dispersed nano particles, low shear rates during mixing and adhesion of the nano particle to the walls of the mixer. Shen et al used solution mixing in toluene followed by melt blending for different time periods for making graphene/Polystyrene (PS) composites leading to migration of PS chains between gaps in the graphene sheets leading to good mechanical interlocking [23].

Solution mixing is one of the most useful ways of making nano composites. The crucial step of this process is the proper dispersion of the nano particle in the chosen solvent. Different processes such as ultra-sonication for breaking up particle agglomerates, and high shear mixing for dispersion, are used to accomplish this goal. Good control on the intensity of mixing is required, since the amplitude during ultra-sonication and the mixing speed can alter the shape and the length of nano fillers which could lead to performance degradation [24,25]. Both thermoset and thermoplastics can be prepared using this approach. Shaffer et al used water as a solvent for dispersion of CNTs and for efficient PVA based composites [26]. Jang et al used ultrasonication for dispersion of CNTs in acetone before forming a thermoset epoxy composite [27]. Khan et al used DMF and THF solvents to create graphene stock solutions using a water

bath sonicator before final introduction into Polyurethane (PU) matrix which gave an exfoliated dispersion [28]. The major drawback of the solvent mixing method is the time required to evaporate the solvent from the polymer/nanofiller blend. It has also been shown recently that minute traces of solvents left in the blend can cause reduction in crosslinking of the polymer chains [29,30]. Kumar et al used in-situ polymerization for making nano graphene composites with EPON 862 polymer with no solvent requirement, leading close to exfoliated dispersions at low graphene wt% [31]. High shear mixing is generally preferred for direct incorporation of nano carbon into the matrix, which can lead to size variations of the nano filler within the final composite. A variety of epoxies have been used in literature for forming in situ polymerized components [32-34].

## **1.2 Carbon nano materials**

### *1.2.1 Nano Clay*

Clays are hydrous silicates or alumino-silicates and fundamentally consist of silicon, aluminum or magnesium, oxygen and hydroxyl groups with various associated cations. (Fig. 1.2) Clays are naturally found in the form of platelets stacked with a few to as many as few thousand sheets. Chen et al reported the Young's Modulus of single clay platelets to be between 178-265 GPa [36].

Nano clays, especially montmorillonite (MMT) have been immensely researched due to their excellent reinforcement characteristics as reported by Toyota Inc. [36]. In their study, a uniform dispersion of MMT was done in Nylon 6. The clay modified composites showed two times more flexural strength and four times more flexural modulus than the Nylon 6 specimens at 120°C for a 4.7 wt% of loading. The MMT crystal structure is composed of one aluminum hydroxide sheet sandwiched between two silicon oxide sheets. The nominal composition of MMT is

$\text{Na}_{1/3}(\text{Al}_{5/3}\text{Mg}_{1/3})\text{Si}_4\text{O}_{10}(\text{OH})_2$ . The layer thickness of each platelet is of the order of 1 nm, and the lateral dimension is approximately 200 nm [37]. The clay platelets are stacked on top of each other by van der Waal interactions separated by a nanometer gap which is occupied with cations, usually  $\text{Na}^+$  and  $\text{K}^+$ . The key to preparing good quality clay nano composites is to achieve exfoliation of large stacks of MMT layers [38,39]. But since the clays are hydrophilic in nature, the surface of the clays need to be made compatible with polymers for achieving good dispersion. This modification is generally done through ion exchange reactions by replacing the interlayer cations with quaternary alkyl-ammonium or alkyl-phosphonium cations [40].

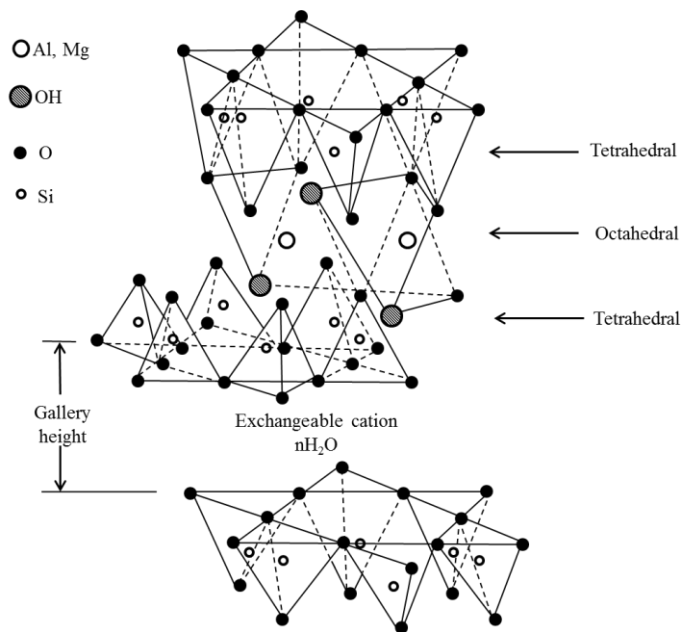


**Figure 1.2** Chemical structure of nano clays (adapted from [35])

Clay platelets have been extensively used to reinforce polymers. Chan et al compared Araldite GY251 resin reinforced with up to 9 wt% of MMT to neat samples. They observed an increase as high as 57% in Young's Modulus for increasing wt% of MMT up to 7 wt% after which it started decreasing for higher wt%. The tensile modulus also followed an increasing trend up to 5 wt% of clay in the system and decreased for higher wt% of clay [41]. Ha et al used aminotriethoxysilane to surface modify the MMT clay platelets and studied the wear behavior of a reinforced and

unreinforced Bisphenol-A epoxy specimen. Better wear characteristics such as lower friction coefficient and specific wear rate was observed using surface modified MMT in the epoxy [42]. Lan et al showed an increase of 10 fold in elastic modulus of EPON 828 epoxy when 15 wt% of exfoliated alkylammonium modified MMT was used in the epoxy [43]. Lin et al used quarternary ammonium chloride to modify Cloisite 30 B nano clay and used 5wt% in a polyester resin. Compressive tests performed revealed 52.8% in compressive yield stress and a 43% increase in Young's modulus and an improved wear behavior in comparison to the neat epoxy specimens [44].

Bashar et al used in situ intercalative polymerization to prepare EPON 826-MMT composites where the MMT was modified using primary and quaternary alkylammonium ions. A 3wt% composite yielded a 19.2% increase in Mode I fracture toughness ( $K_{IC}$ ) of the composite [45]. Qi et al showed an increase of 58% for unmodified MMT-epoxy composites at 10 wt% of loading and a 57% increase for a 5 wt% MMT-CPC/epoxy composites in comparison to the neat epoxy specimens, where MMT-CPC is MMT modified by cetylpyridinium chloride [46]. Becker et al showed 145% increase in  $K_{IC}$  of a DGEBA epoxy for 10 wt% of MMT-I.30E, which is octadecyl ammonium ion-modified MMT [47]. Wang et al used 3-amino propyl trimethoxysilane to modify MMT clay and performed 3 point bend tests to characterize the DGEBA epoxy composites in fracture. Increase in  $K_{IC}$  of about 77% and a 190% increase in  $G_{IC}$  (critical fracture energy) for 2 wt% of nanoclay addition was observed [48].

### *1.2.2 Carbon Nano Tubes (CNTs)*

CNTs are allotropes of carbon which exist as cylindrical hollow structures, with large length to diameter ratios (Fig. 1.3). CNTs have shown considerable capability as nano fillers in polymers and are one of the most widely researched and used nano carbon fillers at present. With

diameters in nanometer scale and lengths which can exceed 1mm, a high aspect ratio leading to an increased surface area, excellent thermal and electrical properties, make CNTs an excellent reinforcement for a polymer matrix [49]. Structurally, CNTs are divided into three types: (1) SWCNTs, (2) double walled CNTs (DWCNTs) and, (3) MWCNTs. Single walled CNTs are reported to have a tensile modulus of 1 TeraPascal (TPa) and a tensile strength of 100 GigaPascal (GPa). Chemical Vapor Deposition (CVD) method, arc discharge method and laser ablation method are generally used for manufacturing CNTs, and selective manufacture of the above types is possible depending on the application [50-52].

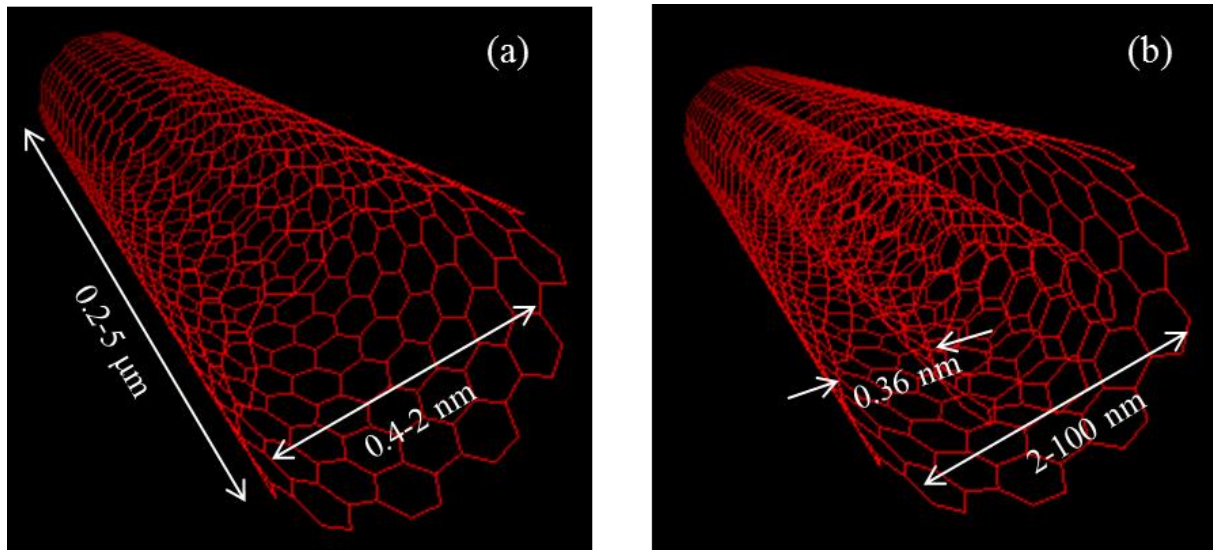


**Figure 1.3** Structure of (a) SWCNT (b) MWCNT (adapted from [53])

Improvements in mechanical properties of epoxy composites using CNTs are well documented in literature. Sun et al showed a 26% increase in modulus and a 16% increase in ultimate tensile strength (UTS) of EPON 862 polymer using 1wt% of SWCNTs [54]. 0.5 wt% of MWCNTs dispersed using an ultrasonic probe in a DGEBA epoxy improved the modulus by 16% [55]. However, some researchers reported a decrease in UTS of the epoxy system with the addition of CNTs [56-58]. Gojny et al proved that the problem lies with the effective stress transfer between the CNTs and epoxy interface which could result from unsatisfactory bonding between epoxy

and CNTs as well as from inadequate dispersion [59]. Functionalization, i.e. creating a bond between the CNT and the polymer, can play a major role in improving the mechanical properties of the CNT/polymer interface, helping in better dispersion of CNTs and improving the adhesion between the polymer and CNTs. Both chemical and physical functionalization has been studied extensively [60-62]. Liu et al showed an increase of 79% in elastic modulus and 47% in UTS with addition of 0.8 wt% of chemically functionalized CNTs with hydroxyl groups in a PVA matrix [63]. Geng et al showed an increase of 145% in modulus by addition of only 1 wt% of fluorinated SWCNTs [64]. The mechanisms behind phenomenal improvement in mechanical properties using functionalization have been explained to be related to the decrease in the intrinsic van der Waals forces between CNTs which helps to reduce agglomeration and achieve better dispersion. Adhesion between the CNTs and the matrix is also improved due to the chemical bonding between the functionalized CNT and matrix [65].

Fracture toughness is an important property desirable for achieving stronger and durable composites for specific applications. Addition of CNTs, in general, has a significant effect on the toughness of epoxies. Gojny et al studied the effect of low wt% CNTs on fracture toughness. They recorded increasing fracture toughness up to 1 wt% CNTs although the samples had a lot of voids. The maximum Mode I fracture toughness improvement at 1 wt% CNT was reported to be ~30% [57]. In another study published by the same author, they observed a 42% increase in Mode I fracture toughness compared with neat epoxies with addition of only 0.3 wt% amino functionalized DWCNTs [59]. Geng et al showed an increase of 60% in Mode I fracture energy due to addition of 0.25 wt% of surfactant treated MWCNTs to EPON 828 epoxy [66]. Ma et al showed a continuous increase in  $K_{IC}$  when up to 0.5 wt% of silane functionalized MWCNTs were added to the same epoxy but observed a steady decline when the CNTs were not

functionalized [67]. Tang et al showed an increase of 110% in fracture toughness due to addition of ozone functionalized MWCNTs to a Bisphenol-A epoxy [68]. Hybrid carbon fiber composites modified using CNTs have been extensively tested for making advanced epoxy composites. Bekyarova et al used Chemical Vapor Deposition (CVD) grown MWCNTs on carbon fiber surface infiltrated by EPON 862 resin using Vacuum Assisted Resin Transfer Molding (VARTM) to show an increase of 30% in interlaminar shear strength [69]. Thostenson et al showed an increase of 15% in interlaminar delamination strength with CNT modified carbon fiber [49]. Boroujeni et al studied the in-plane and out-of-plane mechanical characteristics of the CNT reinforced carbon fiber composites. Around 16% and 19% improvement in properties were observed, respectively [70]. Veedu et al grew a well aligned CNT forest on a two-dimensional SiC fabric to make three-dimensional fabric, then impregnated it with a high temperature epoxy matrix, which showed a 348% improvement in Mode I fracture toughness when compared with non CNT reinforced counterpart, whereas the interlaminar shear strength increased by 54%. Superior performance was explained using SEM micrographs displaying interlocking between the fiber and the matrix due to the CNTs [71].

### *1.2.3 Graphene*

Graphene is another allotrope of carbon: a single layer of carbon atoms bonded densely in a hexagonal honeycomb lattice. (Fig. 1.4) The structure is 2-dimensional, owing to the thinness of the material (1 atom thick), but one of the strongest materials discovered on Earth (200 times stronger than steel) [72]. Graphene has been reported to have a tensile modulus of 1 TPa and a UTS of 130 GPa. It is a great conductor and is a perfect barrier [72]. Graphene's wide range of applications from energy storage applications to immunosensors has made it an ideal test candidate as a filler for polymer systems due to its superior mechanical, electrical and thermal

properties [73,74]. Polymer/nano graphene composites have attracted widespread interest in industry and research due to superior mechanical enhancements at very low filler volume fractions [75-78]. Carbon nanotubes (CNT) have also been widely researched for similar purposes due to their compatibility with various polymer systems and as well as possibility of surface modification of CNTs, but the higher cost of manufacturing high-grade CNTs has made researchers lean towards graphene as a better option for large scale applications and superior epoxy-based composite materials [79-84].

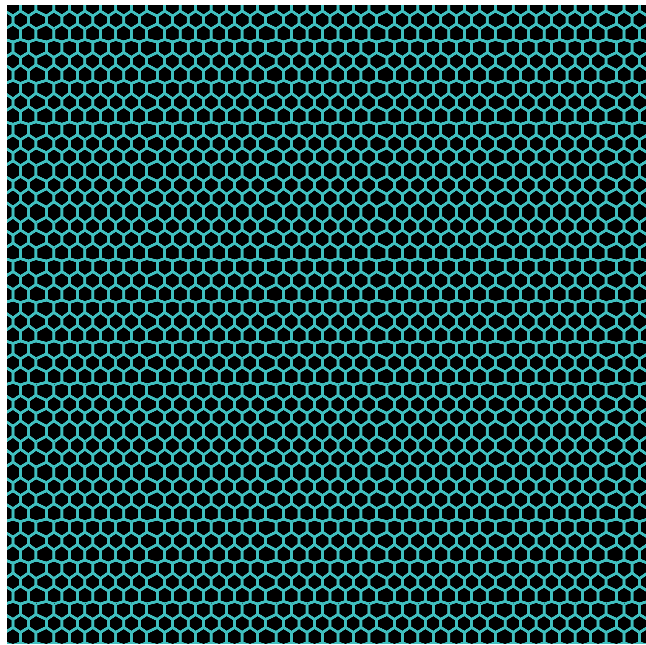


**Figure 1.4** Molecular Structure of graphene (adapted from [85])

Various strategies have been proposed to disperse nano-graphene platelets (NGP) in the polymer matrix with solution mixing and shear mixing being the most widely used processes. Solution mixing involves dispersing the NGPs into suitable organic solvents using sonication and adding the polymer followed by evaporation of the solvent [86-89]. Shear mixing mechanically disrupts the low strength bonds between individual NGPs to disperse the platelets. King [90] reported excellent dispersion of NGPs using purely high shear mixing in epoxy matrix. Chemical

functionalization of the NGPs and the epoxy matrix has been used as another alternative for better dispersion of the filler, which is mainly used to obtain exfoliated NGPs in the matrix [91-93]. Kim achieved good dispersions of NGPs by functionalization in low density polyethylene matrix [94]. Rafiee reported similar dispersion of the NGPs using chemical functionalization of the NGPs through oxidation of bulk graphite in acid, followed by rapid heating in a tube furnace [95,96]. Although this process reduces the agglomeration of the graphene sheets and leads to better phase mixing, it also adds impurities to the system, which are difficult to remove [97]. Graphite oxide sheets have been observed to form stable dispersions in water after ultrasonication which, after de-oxygenation, can be reduced back to graphene. However, most graphene sheets processed using this method exhibit crumpled and wrinkled morphology, which several authors have argued to be an added advantage towards better load transfers and mechanical interlocking between the matrix and the filler [95, 97, 98].

Recent studies using NGPs have reported excellent potential of graphene nanocomposites in improving the elastic modulus, fracture toughness, fracture energy and reduction in fatigue crack propagation rates, for very low (0.1-1) wt% for different thermoset systems [95-103]. Rafiee et al reported approximately 40 % improvement in tensile strength of Bisphenol-A epoxy system with only 0.1 wt% of NGP, compared with only a 11% improvement with the addition of the same wt% of SWCNTs. They also reported a 31% increase in elastic modulus of Bisphenol-A epoxy for 0.1 wt% graphene composites, while very low (<3%) increase in elastic modulus for the same wt% of CNT [96]. Liang et al showed 76% and 62% increases in tensile strength and modulus respectively with only 0.7 wt% of graphene in PVA epoxy composite [104]. Zhao et al showed a 150% increase in tensile strength of 1.8 wt% nanographene/PVA nanocomposites. They also

showed that there exists a maximum threshold of graphene addition (~1.8 volume%) after which increases in mechanical properties was minimal [77].

Addition of NGP to epoxy matrix has been shown to have considerable effect on the fracture toughness and fatigue properties of nano composites. Rafiee et al showed close to 53% and 126% increases in fracture toughness and fracture energies respectively for only 0.1 wt% of NGP in the Epoxy 2000 matrix. The same authors observed around 40-fold decrease in the speed of fatigue crack in the NGP/epoxy nanocomposite, which displays graphene's remarkable potential as a toughening agent [96]. Kumar et al showed approximately ~200% increase in fracture toughness and ~350% increase in fracture energy for only 0.5 wt% of NGPs in EPON 862 thermoset matrix [31]. Bortz et al showed a 111% increase in fracture energy for 0.5 wt% of NGPs in a thermoset matrix [105]. The same authors reported a plateau in the fracture toughness beyond 0.5 wt% of NGPs added to the thermoset epoxy system. The main reason given for this behavior is inadequate dispersion of graphene in the polymer matrix. Surface functionalization of the platelets may be used to solve the problem up to a certain extent.

In research published to date, the major improvement in mechanical properties has been attributed to the increased surface roughness, crack pinning and crack deflection processes due to the presence of NGPs. It has also been reported that particle matrix debonding and plastic deformation of the matrix could be potential mechanisms for the dramatic increase in toughness [103]. Thus, it is clear that graphene opens new avenues in the future of lightweight nano-composite structures, with its exceptional mechanical and toughening properties.

The following work aims to study several areas of NGP reinforced composites encompassing environmental barrier properties, Mode I and mixed mode fracture behavior of nano composites, Mode I behavior of carbon fiber/nano graphene reinforced composites, and the influence of NGP

alignment and dispersion in thermoset epoxy system. EPON 862 has been chosen as the epoxy matrix which is an emerging epoxy system used for aerospace applications due to its low processing viscosity and better mechanical properties. EPON 862 is an aerospace grade difunctional epoxy resin with very low molecular weight. It is categorized as a thermoset polymer system with high crosslink density when mixed with curing agent 'W'. Although the polymer itself is strong, it is relatively brittle with low stiffness, which makes it a suitable candidate for the proposed toughness enhancement study.

## CHAPTER 2

### MODELING OF ANOMALOUS MOISTURE DIFFUSION IN NANOGRAPHENE REINFORCED THERMOSET POLYMERS

#### 2.1 Summary

It is well known that the thermal and mechanical properties of epoxy resins are strongly affected by moisture absorption which leads to reduced glass transition temperatures ( $T_g$ ) of the cured epoxy systems. Hence, it is quite evident that modeling of water uptake in polymer systems is of utmost importance for accurate life predictions of a composite structure.

Various models have been proposed for modeling moisture diffusion in polymers, the most fundamental being Fick's Law in its one dimensional form. However, it has been shown in various studies that moisture absorption in various polymers is anomalous (Non-Fickian) [106]. Frequently, the moisture absorption in a polymer and/or polymer nanocomposite is non-Fickian (anomalous) with two saturation stages that has been the subject of various modeling attempts. Anomalous moisture diffusion models include Time Varying Diffusivity model (TVD) and Time Varying Concentration model (TVC) which assume a reducing diffusivity and boundary concentration respectively with time to model the anomalous absorption [106,107].

The rationale has been established through the thermodynamic descriptions of diffusion of permeants in polymers by Frisch and Crank [108,109]. Frisch proved that for polymers below their glass transition temperatures, the diffusion parameters are governed by set of "internal parameters", time, concentration and pressure. In this context, a set of equations known as the

Gibbs-Duhem relations are developed, and the governing equation for diffusion in a polymer takes the form

$$\frac{\partial C}{\partial t} = \frac{\partial}{\partial t} \left( \bar{D}_{ij} \frac{\partial C}{\partial X_j} \right) \quad (2.1)$$

Where the diffusivity is given by,

$$\bar{D}_{ij}(X_i, T, \sigma, t) = \left[ \frac{L_{ij}}{(1-C)} \left( \frac{\partial \mu}{\partial C} + \sum_{r=1}^n \frac{\partial \mu}{\partial \ln q_r} \right) \right] \quad (2.2)$$

Where  $C$  is the moisture concentration,  $X_i$  are the spatial coordinates,  $T$  is the temperature,  $\sigma$  represents an invariant stress measure,  $t$  is the time,  $L_{ij}$  are the Onsager coefficients,  $\mu$  is the chemical potential of the diffusing vapor, and  $q_r$  are the hidden coordinates that define the internal motion of the individual chain segments in polymer molecules thereby viscoelastic behavior in a polymer. For an unstressed polymer, this time varying diffusivity can be described by a Prony series as described in [106].

Weitsman [107] suggested that for viscoelastic materials, the chemical potential  $\mu(t)$  of the vapor can be described in form of a Prony series, as

$$\mu(t) = \mu_o + \sum_{n=1}^N \mu_n (1 - e^{-\beta_n t}) \quad (2.3)$$

This observation was used by Cai to represent the boundary concentration in view of the time dependent response of the polymer [107],

$$C(\pm L, t) = \left[ C_o + \sum_{n=1}^N C_n (1 - e^{-\beta_n t}) \right] H(t) \quad (2.4)$$

Where  $H(t)$  is the Heaviside's step function.

Nanographene is a one atom thick planar sheet of carbon atoms that has been an ideal test bed for science due to its unprecedented physical properties. Experiments conducted on graphene-

reinforced PVA composite films have shown approximately 50% improvement in barrier properties when subjected to humidity, and approximately 50-60% increase in tensile properties and fracture toughness experiments [95,110]. This makes graphene a suitable choice for use as advanced filler in nanocomposites. Liu [111] proposed tortuosity factors for exfoliated and intercalated nanoclay platelets to incorporate changes in diffusivity due to different aspect ratios of platelets.

The objective of this chapter is to present a coupled methodology incorporating the concepts of time varying diffusivity as well as boundary concentration, and Liu's [111] definition of tortuosity factor to model two-stage moisture absorption in epoxy resins, with and without graphene nanofiller. In this study, thermoset epoxy EPON 862 and nanographene have been selected as the epoxy and nanoparticle system respectively for model validation purposes. Hygrothermal absorption experiments on baseline, 0.5 wt%, 1 wt%, 3 wt% nanographene reinforced polymer composite (NRPC) have been used to predict model responses for 0.1 wt% and 2 wt% NRPCs which have been compared with experimental data for these specimens. To our knowledge this coupled approach has not been attempted to date.

Anomalous two-stage moisture diffusion in baseline thermoset epoxy (EPON 862), and in nanographene platelet (NGP) reinforced epoxy has been studied. The deviation from Fickian diffusion is assumed to be intrinsically dependent on the time varying viscoelastic response of the epoxy and its nanoparticle reinforced polymer nanocomposite. A novel viscoelasticity based model has been formulated which aims to capture the response of the two-stage moisture absorption response, incorporating the effect of time-dependent relaxation of the material, and random orientation and aspect ratio of the NGPs on the moisture absorption. Moisture uptake experiments at 60<sup>0</sup> C and 90% relative humidity were performed in an environmental chamber

for five different weight percentages (wt%) ranging from 0.1 wt% to 3 wt% NGPs and their response was compared with baseline epoxy specimens. Upon benchmarking to extract modeling parameters, the model was used to predict anomalous moisture uptake for 0.1 and 2 wt% NGP. The following work forms a part of research published by Kumar et al [112].

## **2.2 Experimental section**

Moisture uptake experiments were performed according to ASTM D570-98 [113] at 60<sup>o</sup> C and 90% relative humidity in a Cincinnati Subzero environmental chamber using deionized water vapor source on 1 inch x 1 inch epoxy specimens with a thickness of 0.125 inches. A nanocomposite system with EPON resin 862 (Diglycidyl Ether of Bisphenol F, supplied by Miller Stephenson Inc.) as the matrix component and NGP (Grade M-15, supplied by XG Sciences, Inc.) as the nano-reinforcement, was used to make the specimens following the procedure by King [114]. The NGPs were supplied as short stacks of graphene sheets with a thickness of 6 nm and average diameter of 15  $\mu\text{m}$ , which gives an average aspect ratio of 2500 for the NGP.

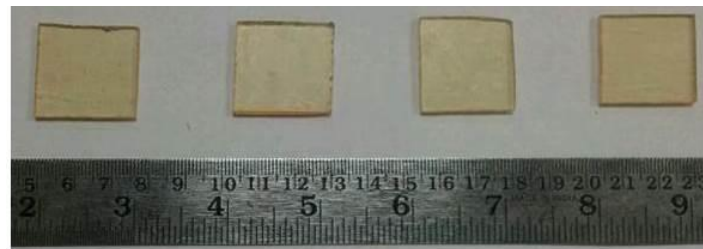
Six types of specimens were manufactured: baseline (epoxy without nanographene), 0.1 wt%, 0.5 wt% , 1 wt%, 2 wt% and 3 wt% NRPC. Four replicate specimens of each wt% were tested to account for statistical variation. Fig. 2.1 shows the moisture specimens manufactured. Fig. 2.2 depicts the experimental moisture uptake % as a function of square root of time for each wt% NRPC specimen. It is quite evident from this figure that the moisture absorption is non-Fickian (anomalous) with two saturation stages for the baseline epoxy as well as for the NRPC. To study the dispersion of graphene platelets, Transmission Electron Microscopy (TEM) has been utilized. In essence, the TEM study in Fig. 2.3 shows the highly random arrangement of NGPs in the

matrix with the presence of both single and stacked sheets in 3 wt% NRPC samples, which suggests partial exfoliation and intercalation of the graphene sheets.

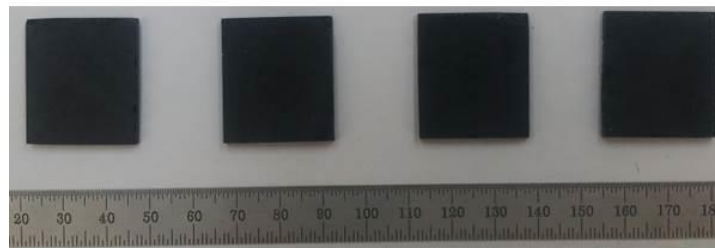
## 2.3 Modeling of diffusion in nanocomposite

### 2.3.1 Diffusion with Boundary conditions and Diffusivity of time-varying type

The governing equation for one dimensional diffusion in a polymer sheet of thickness  $2L$  is represented by the well-known Fick's Law,



(a)



(b)

**Figure 2.1** Moisture absorption manufactured specimens (a) Baseline (b) 1 wt% NRPC

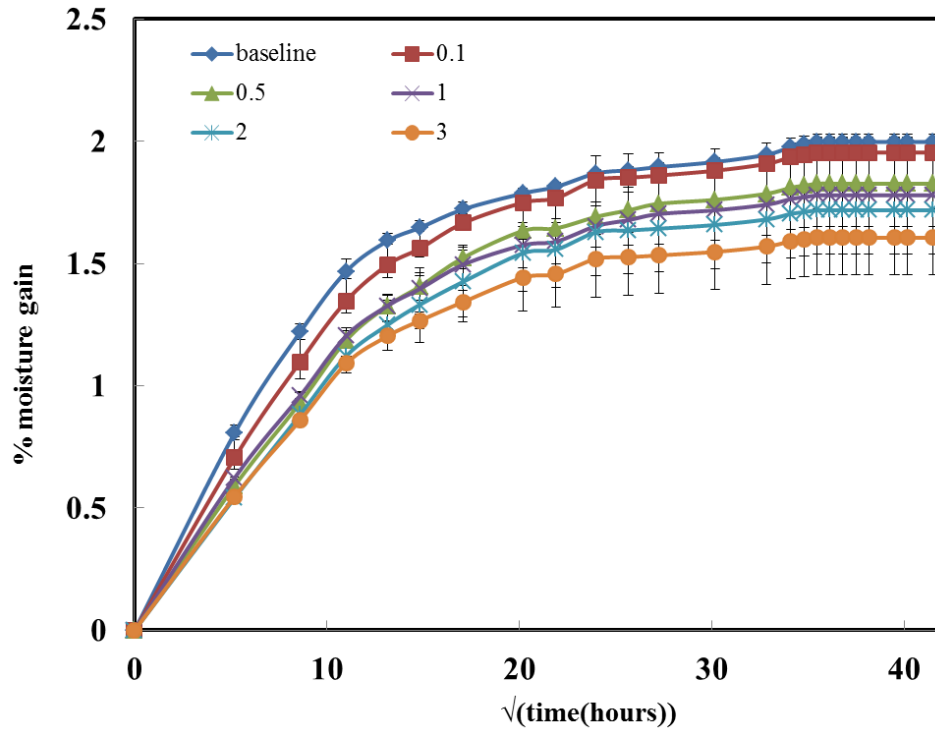


**Figure 2.2** Experimental moisture absorption profiles for baseline and NRPC specimens as a function of time

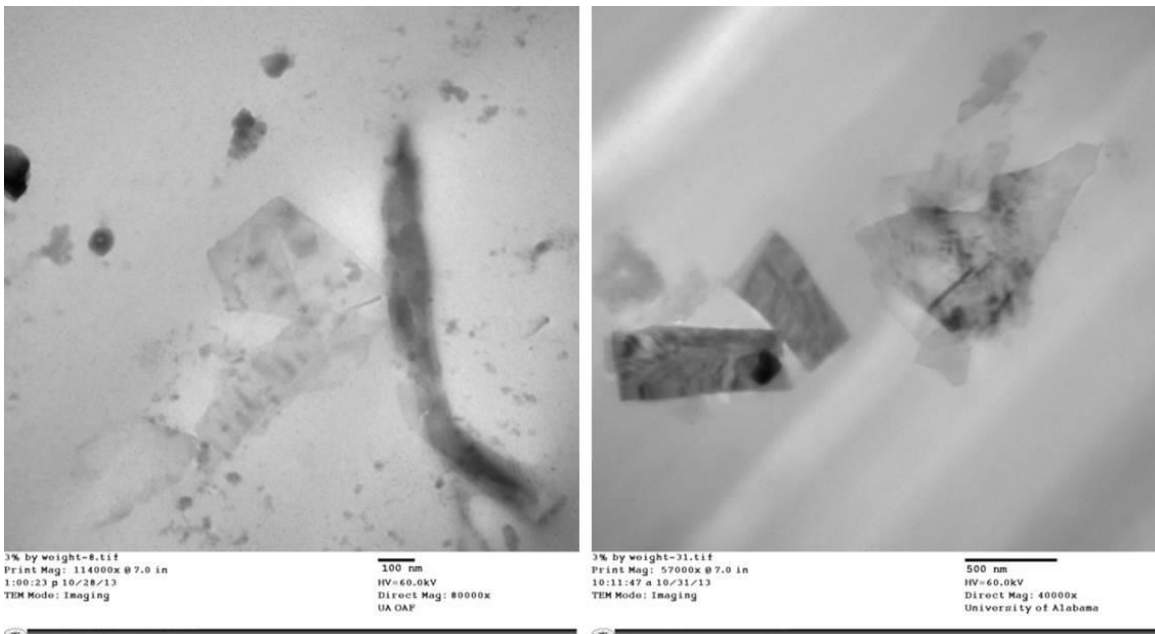


**Figure 2.3** Dispersion analyses of nanographene platelets for 3 wt% NRPC specimens using TEM

$$\frac{\partial C}{\partial t} = D(t) \frac{\partial^2 C}{\partial z^2}, \quad 0 \leq z \leq 2L, \quad t \geq 0 \quad (2.5)$$

The field Equation (2.1) is defined by a set of initial and boundary conditions given by,

$$\begin{aligned} C(z, 0) &= C_i(z) & 0 \leq z \leq 2L \\ C(0, t) &= C(2L, t) = C_b(t) & t \geq 0 \end{aligned} \quad (2.6)$$

Where  $z$  is the spatial coordinate and  $t$  is time.  $C(z, t)$  is the moisture concentration, and  $D(t)$  is a spatially constant but time varying diffusivity. In classical (Fickian) formulations,  $D(t)$  is treated as a constant. In this article,  $D(t)$  deviates from this general assumption.

Consider a specific case of an infinite plate of thickness  $2L$  undergoing moisture diffusion following the general Fick's Law in Equation (2.5) with initial and time-varying boundary conditions as defined below,

$$\begin{aligned} C(z, 0) &= C_{in} \\ C(0, t) &= C(2L, t) = C_o + \sum_{r=1}^N C_r (1 - e^{-\beta_r t}) \end{aligned} \quad (2.7)$$

Where the boundary condition is represented by a Prony series, where  $C_o$ ,  $C_r$  and  $\beta_r$  are material constants to be determined from the moisture diffusion experiments.

Assuming that time-varying diffusivity is also expressed as a Prony series assumed to be uniform through the thickness of the polymer

$$D(t) = D_o + \sum_{r=1}^N D_r (1 - e^{-\beta_r t}) \quad (2.8)$$

where  $D_o$ ,  $D_r$  and  $\beta_r$  are material constants to be determined from the moisture diffusion experiments.

### 2.3.2 Diffusion Path Tortuosity model

To completely define the diffusivity through a heterogeneous medium (polymer with NGPs), we assume that the NGP platelets are impenetrable, intercalated in the polymer matrix, and randomly oriented. Presence of the NGPs within the polymer creates a tortuous diffusion path for the permeant (water) molecules as depicted in Fig. 2.4.

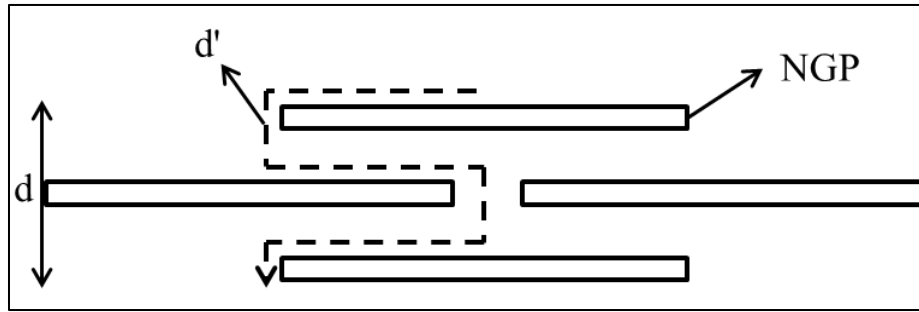


**Figure 2.4** Tortuous diffusion path due to presence of NGPs in the polymer matrix

A diffusion path tortuosity factor ' $\tau$ ' is introduced to account for the influence of tortuous path created by the presence of a nanoplatelet. Physically,  $\tau = d/d'$ , where  $d$  is the effective diffusion distance for a water molecule in the absence of nanoparticles in the polymer, and  $d'$  is the actual distance the water molecule has to travel in the presence of the nanoparticles as depicted in Fig. 2.4. Using the randomly oriented intercalated platelet model of Liu [111], the tortuosity factor can be expressed as,

$$\tau = \frac{1}{\left(1 + \frac{2\zeta v_c}{3n\pi}\right)^2} \quad (2.9)$$

Where  $v_c$  is the volume fraction of nanographene platelets,  $n$  is the number of intercalated platelets and  $\zeta$  is its aspect ratio. In order to incorporate the diffusion barrier effect due to the

presence of NGPs, each diffusivity term in Equation (2.8) is scaled by a factor of ‘ $\tau$ ’ and the final diffusivity Prony series model takes the form,

$$\bar{D}(t) = \tau D(t) = \tau D_o + \sum_{r=1}^N \tau D_r (1 - e^{-\beta_r t}) \quad (2.10)$$

In this manner the proposed model incorporates the effects of random orientation and average aspect ratio of the NGPs through the diffusion path tortuosity model.

### 2.3.3 Model description

Introducing a change in variable

$$dT = D(t)dt \quad (2.11)$$

Thus, the governing Equation (2.1) can be reduced to,

$$\frac{\partial C}{\partial T} = \frac{\partial^2 C}{\partial z^2} \quad (2.12)$$

The boundary conditions also need to be expressed in terms of  $T$  as,

$$C(0, T) = C(2L, T) = C_o + \sum_{r=1}^N C_r (1 - e^{-\beta_r t(T)}) \quad (2.13)$$

The initial condition remains unchanged because it is a constant.

The challenge in solving this problem lies in expressing time  $t$ , as a function  $t(T)$  in Equation (2.13) since  $D(t)$  is unknown at this stage. To circumvent this problem, an approximate choice of  $t(T)$  as a power-law expansion is introduced as below,

$$t(T) = \sum_{m=0}^{N'} p_m T^m \quad (2.14)$$

To obtain the solution of the governing Equation (2.5), the problem is divided into two parts: first, the contribution from the constant part of the boundary condition denoted by  $C_H(z, T)$  and

the other influenced by the time-varying part given by  $\hat{C}(z, T; \beta_r)$ . The complete solution can be expressed as explained in Cai [107],

$$C(z, T) = C_o C_H(z, T) + \sum_{r=1}^N C_r \hat{C}(z, T; \beta_r) \quad (2.15)$$

Where,  $C_o$  and  $C_r$  are constants that need to be characterized through moisture absorption experiments. Similarly, the mass uptake can be expressed as a function of mass uptake due to the constant boundary condition contribution  $M_H(T)$  and the time-varying boundary condition contribution  $\hat{M}(T; \beta_r)$  as in Cai [107],

$$M(T) = C_o M_H(T) + \sum_{r=1}^N C_r \hat{M}(T; \beta_r) \quad (2.16)$$

The following steps were followed to completely express  $C(z, t)$  and  $M(t)$  :

#### 2.3.4 Constant boundary condition solution

Assume,  $C_H(z, T) = 1 + v(z, T)$

$v(z, T)$  is evaluated following the approach by Carslaw [115]. A detailed proof for the ‘constant boundary condition’ solution can be found in Appendix A.

$C_H(z, T)$  can then be expressed as,

$$C_H(z, T) = 1 + \frac{2}{\pi} (1 - C_{in}) \sum_{n=1}^{\infty} \frac{((-1)^n - 1)}{n} e^{-\frac{n^2 \pi^2 T}{4L^2}} \sin \frac{n\pi z}{2L} \quad (2.17)$$

#### 2.3.5 Time-varying Prony series boundary condition solution

Assume,  $\hat{C}(z, T; \beta_r) = u(z, T) + w(z, T; \beta_r)$ ,

$u(z, T)$  can be obtained using an approach similar to Section 2.3.4.  $w(z, T; \beta_r)$  is evaluated using the Duhamel’s Integral as in [115].

A detailed proof of ‘Time varying Prony series boundary condition solution’ can be found in Appendix B.

$\hat{C}(z, T; \beta_r)$  can be finally written combining  $u(z, T)$  and  $w(z, T; \beta_r)$ , where  $I(T)$  is expressed as in Equation (B.12).

$$\hat{C}(z, T; \beta_r) = -\frac{2C_{in}}{\pi} \sum_{n=1}^{\infty} \frac{((-1)^n - 1)}{n} e^{-\frac{n^2 \pi^2 T}{4L^2}} \sin \frac{n\pi z}{2L} - \frac{\pi}{2L^2} \sum_{n=1}^{\infty} n((-1)^n - 1) e^{-\frac{n^2 \pi^2 T}{4L^2}} \sin \frac{n\pi z}{2L} \left[ \frac{4L^2}{n^2 \pi^2} \left( e^{\frac{n^2 \pi^2 T}{4L^2}} - 1 \right) - I(T) \right] \quad (2.18)$$

### 2.3.6 Development of model solution

Integration of the concentration along the thickness provides the net weight gain for sections 2.3.4 and 2.3.5 as

$$M_H(T) = \int_0^{2L} C_H(z, T) dz \quad (2.19)$$

This can be expressed as,

$$M_H(T) = 2L \left[ 1 + 2 \frac{(C_{in} - 1)}{\pi^2} \sum_{n=1}^{\infty} \frac{((-1)^n - 1)^2}{n^2} e^{-\frac{n^2 \pi^2 T}{4L^2}} \right] \quad (2.20)$$

Similarly,

$$\hat{M}(T; \beta_r) = \frac{4LC_{in}}{\pi^2} \sum_{n=1}^{\infty} \frac{((-1)^n - 1)^2}{n^2} e^{-\frac{n^2 \pi^2 T}{4L^2}} + \frac{1}{L} \sum_{n=1}^{\infty} ((-1)^n - 1)^2 e^{-\frac{n^2 \pi^2 T}{4L^2}} \left[ \frac{4L^2}{n^2 \pi^2} \left( e^{\frac{n^2 \pi^2 T}{4L^2}} - 1 \right) - I(T) \right] \quad (2.21)$$

Finally, we can express  $M(T)$  using Equation (2.16) and replace  $T$  with time  $t$ , using the definition in Equation (2.11).

### 2.3.7 Evaluation of diffusivity coefficients

The diffusion model in this article assumes a Prony series representation for diffusivity and expression for  $\lambda(x)$ , and a power law expression for  $t(T)$  which results in concentration and

weight gain expressions in Equations (2.15) and (2.16) containing  $(2N+N'+3)$  unknowns each which makes the total number of unknowns to be  $(2(2N+2)+N'+1)$ . Evaluation of these unknowns does not follow a linear least squares approach since the equation is highly nonlinear in the unknowns. If a further simplification to the solution is made by assuming that viscoelastic-relaxation is the same in bulk epoxy as at the boundary, we can express Equation (2.16) as,

$$M(T) = \bar{c} \left( \hat{D}_o M_H(T) + \sum_{r=1}^N \hat{D}_r \hat{M}(T; \beta_r) \right)$$

Also assume  $D_k' = \bar{s} \hat{D}_k$ , where  $\bar{c}$  and  $\bar{s}$  are constants.

This limits the total number of unknowns to  $(N+N'+3)$ . A nonlinear least squares algorithm (Nelder-Mead) is sought to evaluate these coefficients which is a numerical method for minimizing an objective function in a multi-dimensional space. The algorithm works on a simplex methodology which is a generalized triangle defined by the number of variables (diffusivity coefficients). The algorithm has been described based on the work by Lagarias [116].

### 2.3.8 Model development using *fminsearch* function in Matlab

Matlab automatically implements the Nelder-Mead algorithm using a built in *fminsearch* function which finds a minimum of a multivariable function starting at an initial estimate. The termination tolerance on the scalar variables (diffusivity coefficients) has been set at  $1 \times 10^{-4}$ . The *fminsearch* function has been manipulated to take the experimental moisture uptake data as input and uses the analytical mass uptake expression in Equation (2.16) to return a set of diffusivity coefficients to model the experimental data. The results obtained from this approach are discussed below.

## 2.4 Results and Discussion

### 2.4.1 Diffusion Model Assumptions

Since the number of terms in the Prony series diffusivity approximation are arbitrary,  $N=6$ , i.e. 7 unknown diffusivity coefficients ( $D_k$ ), was selected for computational modeling.  $N'$  for the polynomial assumption of  $t(T)$  in Equation (2.13) was selected to vary as  $N'=N+1$ , which leads to 8 unknown polynomial coefficients ( $p_m$ ). Together with the constants  $\bar{s}$  and  $\bar{c}$  as introduced in Section 2.2.7, a total of 17 unknowns were evaluated using the `fminsearch` function. For this analysis, the relaxation parameters  $\beta_r$  were kept the same for all six specimen simulations. The relaxation parameters were selected using the results in Roy [106]. Since the epoxy resin system is different in [106], relaxation parameters were slightly modified to get a converged solution. The value  $n$  in Equation (2.9) was set to be 10 intercalated platelets for this study. This value was chosen due to the fact that NGP sheets are originally supplied as agglomerates of ~15-20 platelets [117]. In spite of the high shear mixing of NGP in epoxy, our TEM observations revealed that graphene sheets were still intercalated to a significant extent in the epoxy matrix. The value of  $n=10$  was obtained iteratively through optimizing the best fit to the moisture data. Table 2.1 lists the tortuosity factors for each NGP wt% analysis obtained using Equation (2.9). Table 2.2 provides the relaxation- time parameters selected for this analysis.

### 2.4.2 Model Benchmarking and Uptake Prediction

The available moisture uptake experimental data was subdivided into two data sets. The first set of data (baseline, 0.5 wt%, 1 wt% and 3 wt% NRPC specimens) were employed to evaluate the 17 unknown coefficients in the anomalous diffusion model using the nonlinear least squares curve fit discussed earlier. It should be noted that the number of unknowns is reduced once the diffusivity fit for the baseline resin is obtained, since the diffusivities of the NGP reinforced

specimens can be found through the scaling factor  $\tau$ , using Equation (2.10). Fig. 2.5 shows that the anomalous diffusion model results for baseline, 0.5 wt%, 1 wt% and 3 wt% NRPC specimens agrees well with the moisture uptake data, which is expected since these data were used to evaluate the model parameters. Once these unknown coefficients were evaluated, the anomalous diffusion model was then applied to *predict* the uptake for the 0.1 wt% and 2 wt% cases using linear interpolation of the unknown coefficients. Fig. 2.6 shows the model predictions for 0.1 wt% and 2 wt%, specimens. The good agreement between the model and the moisture uptake data underscores the model's ability to account for both anomalous diffusion due to viscoelastic relaxation in the polymer and the enhanced tortuosity in the diffusion path due to the presence of nanographene platelets.

**Table 2.1** Tortuosity factors for baseline and NRPC specimens used for modeling

<b>Composite</b>	<b>Baseline</b>	<b>0.1 wt%</b>	<b>0.5 wt%</b>	<b>1 wt%</b>	<b>2 wt%</b>	<b>3 wt%</b>
	<b>(<math>\tau_0</math>)</b>	<b>(<math>\tau_{0.1}</math>)</b>	<b>(<math>\tau_{0.5}</math>)</b>	<b>(<math>\tau_1</math>)</b>	<b>(<math>\tau_2</math>)</b>	<b>(<math>\tau_3</math>)</b>
<b>Tortuosity factor(<math>\tau</math>)</b>	1	0.9473	0.7729	0.6145	0.4141	0.297

**Table 2.2** Relaxation parameters ( $\beta_r$ ) assumed for modeling

<b>Relaxation parameter</b> <b>(<math>s^{-1}</math>)</b>	<b><math>\beta_1</math></b>	<b><math>\beta_2</math></b>	<b><math>\beta_3</math></b>	<b><math>\beta_4</math></b>	<b><math>\beta_5</math></b>	<b><math>\beta_6</math></b>
	1/600	1/6000	1/30000	1/600000	1/3000000	1/6000000

It is evident from Figs. 2.5 and 2.6 that the present model is accurate in predicting both the mid-saturation levels and the final saturation levels closely during the two-stage diffusion in the test specimens. The model predictions for 0.1 and 2 wt% capture the details of the moisture absorption quite well. The Prony series diffusivity parameters calculated using this model for all six types of specimens are tabulated in Table 2.3.

Fig. 2.7 compares the diffusivity variation with time for the six specimens, using the parameters in Tables 2.2 and 2.3 and substituting in Equation (2.8). It is observed that for the baseline epoxy, the diffusivity exhibits reduction (relaxation) in the early stages and then gradually increases and reaches steady state as a function of time. The diffusivity profiles for the NRPC specimens also follow a similar pattern, with a monotonically decreasing diffusivity with increasing nanographene wt%. The reason for this behavior is most likely due to (a) the increased tortuosity of the diffusion path, and (b) the constraining effect of nanographene platelets on the normal relaxation behavior of the epoxy network [118]. More work is needed to determine the exact nature of the influence of NGP on time-varying changes in free volume in the EPON 862 system.

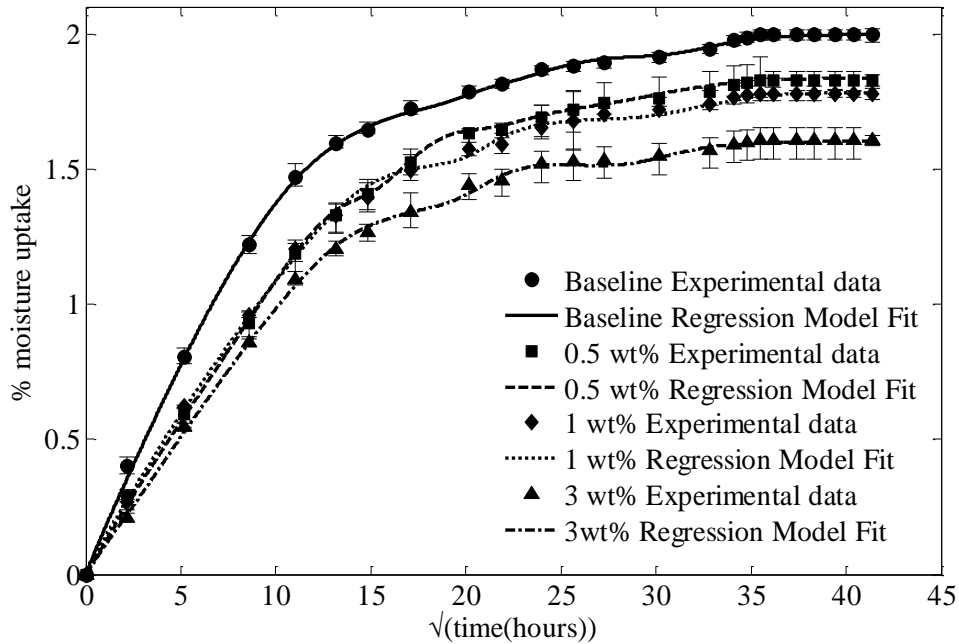


**Figure 2.5** Regression model fits for baseline, 0.5, 1, 3 wt% NGP compared with experimental data

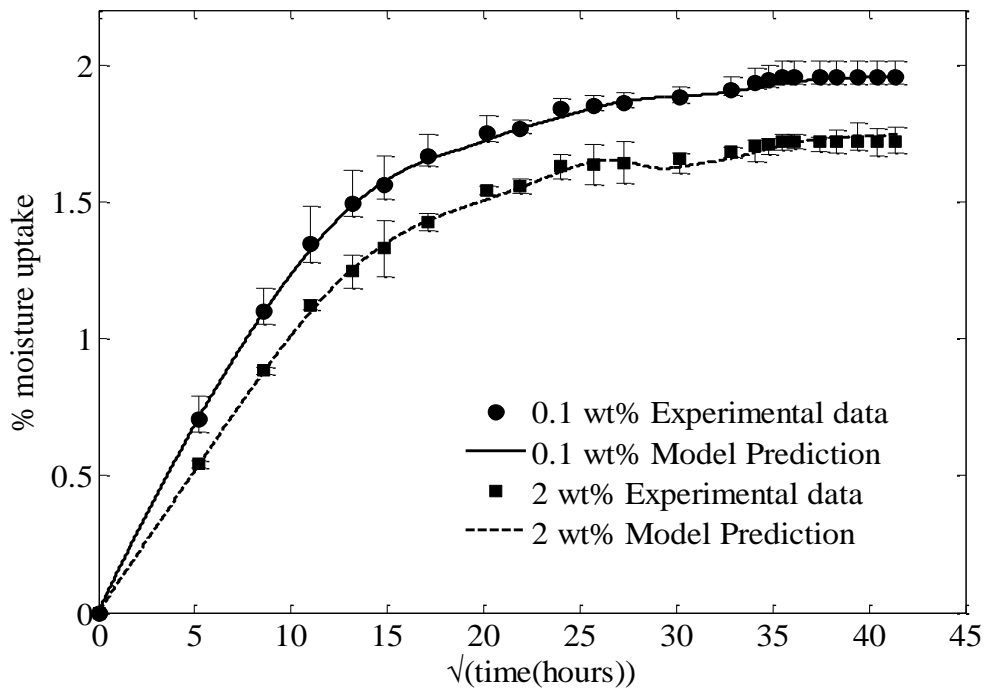


**Figure 2.6** Regression model predictions for 0.1, 2 wt% NGP compared with experimental data

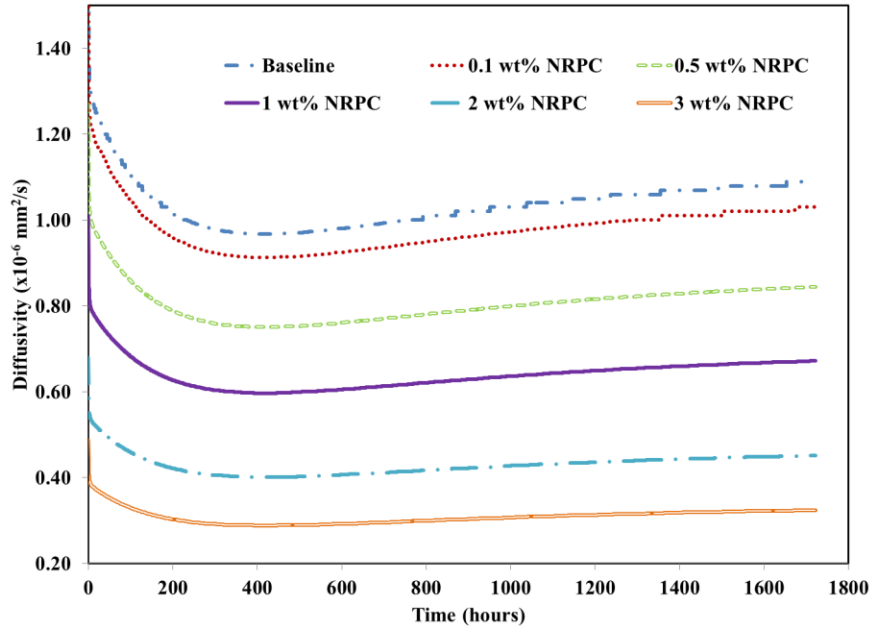


**Figure 2.7** Diffusivity variation predicted by model for baseline and NRPC specimens

**Table 2.3** Diffusion coefficients for baseline and NRPC specimens obtained from diffusion model

Diffusion coefficients (mm <sup>2</sup> /s)	Baseline (D <sub>b</sub> )	0.1 wt% (τ <sub>0.1</sub> *D <sub>b</sub> )	0.5 wt% (τ <sub>0.5</sub> *D <sub>b</sub> )	1 wt% (τ <sub>1</sub> *D <sub>b</sub> )	2 wt% (τ <sub>2</sub> *D <sub>b</sub> )	3wt% (τ <sub>3</sub> *D <sub>b</sub> )
D <sub>0</sub>	1.64x10 <sup>-6</sup>	1.56x10 <sup>-6</sup>	1.27x10 <sup>-6</sup>	1.01x10 <sup>-6</sup>	6.8x10 <sup>-7</sup>	4.88x10 <sup>-7</sup>
D <sub>1</sub>	-1.75x10 <sup>-7</sup>	-1.66x10 <sup>-7</sup>	-1.4x10 <sup>-7</sup>	-1.1x10 <sup>-7</sup>	-7.3x10 <sup>-8</sup>	-5.2x10 <sup>-8</sup>
D <sub>2</sub>	-1.58x10 <sup>-7</sup>	-1.49x10 <sup>-7</sup>	-1.2x10 <sup>-7</sup>	-9.7x10 <sup>-8</sup>	-6.5x10 <sup>-8</sup>	-4.7x10 <sup>-8</sup>
D <sub>3</sub>	-1.14x10 <sup>-8</sup>	-1.08x10 <sup>-8</sup>	-8.8x10 <sup>-9</sup>	-7x10 <sup>-9</sup>	-4.7x10 <sup>-9</sup>	-3.4x10 <sup>-9</sup>
D <sub>4</sub>	-5.02x10 <sup>-7</sup>	-4.75x10 <sup>-7</sup>	-3.9x10 <sup>-7</sup>	-3.1x10 <sup>-7</sup>	-2.1x10 <sup>-7</sup>	-1.5x10 <sup>-7</sup>
D <sub>5</sub>	3.36x10 <sup>-7</sup>	3.18x10 <sup>-7</sup>	2.6x10 <sup>-7</sup>	2.07x10 <sup>-7</sup>	1.39x10 <sup>-7</sup>	9.98x10 <sup>-8</sup>
D <sub>6</sub>	2.49x10 <sup>-9</sup>	2.35x10 <sup>-9</sup>	1.92x10 <sup>-9</sup>	1.53x10 <sup>-9</sup>	1.03x10 <sup>-9</sup>	7.39x10 <sup>-10</sup>

## CHAPTER 3

### CHARACTERIZATION OF MODE I FRACTURE PROPERTIES OF NANOGRAFENE REINFORCED EPON 862 THERMOSET POLYMER SYSTEM

#### 3.1 Summary

This chapter studies the differences in fracture properties (stress intensity factors and energy release rates) of nanocomposites of thermosetting polymer EPON 862 and its nano-graphene reinforced counterparts. Extremely low (0.1 and 0.5) weight percent nano-graphene platelets were dispersed in EPON 862 matrix and compact tension (CT) fracture experiments were conducted under quasi-static loading conditions using displacement control. Significant enhancements in fracture toughness  $K_{IC}$  (~200%), and energy release rate  $G_{IC}$  (~570%) respectively were observed in nano-graphene reinforced matrix with only 0.5 wt% of graphene platelets. Fractography analysis of the fractured CT specimens was used to qualitatively visualize and understand the mechanism(s) responsible for the enhancement in these properties using Scanning Electron Microscopy (SEM). Evidence of crack deflection due to increased surface roughness, graphene platelet pullout and plastic deformation of the matrix causing filler-matrix debonding, was observed from SEM micrographs, caused by the addition of nano-graphene platelets (NGP). Atomic Force Microscopy (AFM) was also used to quantify the magnitude of surface roughness changes between the NGP reinforced and unreinforced nano-composite samples, and correlate surface roughness changes due to crack deflection to increased fracture toughness. Studies are also presented for CT tests conducted on 90% humidity, 60°C aged specimens and the results are compared to unaged specimen CT testing results.

## 3.2 Experimental Section

### 3.2.1 Materials

Graphene nanoplatelets with an average diameter of  $15\ \mu\text{m}$  were procured from XG-Sciences Inc. The platelets were supplied in small stacks (15-20 graphene platelets) as depicted in Fig. 3.1(A) with 99.9 % purity and no functionalization. The stack has an average thickness of 6 nm and a typical surface area of 120-150  $\text{m}^2/\text{g}$  [117]. The epoxy used in the study was EPON 862, which is di-glycidyl ether of bisphenol-F epoxy (DGEBF) from Momentive Inc. and the curing agent used was Curing agent 'W' (DETDA (diethyl toluene diamine)). Figs. 3.1 (B)-(C) illustrates the molecular structures of the thermoset polymer and curing system used in the study. DETDA amine groups act as the crosslink centers.

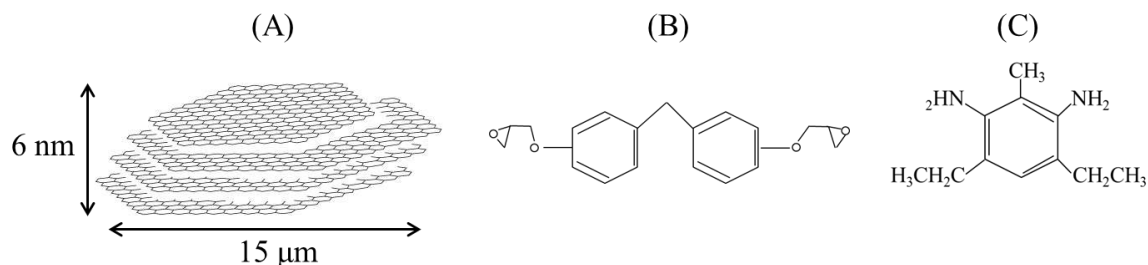


**Figure 3.1** (A) Schematic of the supplied nano graphene platelet (NGP) stack (adapted from [117]), Molecular structure (B) EPON 862 (C) DETDA (adapted from [119])

### 3.2.2 Dispersion of NGP

The desired wt% of NGP was weighed and dispersed in the epoxy using a high shear mixer (EuroStar power-b) at 2000 rpm for 45 minutes. The high shear mixing was performed based on the dispersion notes from the NGP manufacturer [117]. The curing agent was then added to the mixture and the blend was stirred for 3 minutes at 2000 rpm. The epoxy to curing agent weight ratio was 100:26.4 as provided by the manufacturer.

### *3.2.3 Curing cycle and specimen preparation*

The mixture was degassed using a vacuum oven (Stable temp 282A) for 30 minutes at 90°C to remove the bubbles created during the mechanical stirring process. The hot mixture was poured into hot silicone molds to limit any production of bubbles during pouring. The silicon molds were then placed in an oven and subjected to a cure cycle as follows: (I) 90° to 121°C in 30 minutes (II) maintain 121°C for 2 hours (III) 121° to 177°C in 30 minutes (IV) maintain 177°C for 2 hours. The molds were cooled to ambient temperature after the cure cycle finished, and the samples were ready for testing.

### *3.2.4 Testing*

Compact Tension (CT) testing was chosen to characterize the fracture behavior. CT specimen dimensions were 0.03 m x 0.03 m x 0.006 m, based on the ASTM D5045 standard test protocol [120]. CT specimens manufactured are shown in Fig. 3.2. The change in color of epoxy due to the presence of NGP is very noticeable. Razor blade tapping was used to generate a sharp starter notch to pre-crack the CT specimens, as delineated in the ASTM D5045 standard. The pre-crack tips are illustrated in Fig. 3.3. Nanometer scale crack tip dimensions were observed for all specimens, thereby ruling out macroscale crack tip blunting as the primary mechanism for the increase in toughness. Four replicate CT samples for each specimen type (baseline, 0.1 wt%, 0.5 wt%) were tested to account for statistical scatter. The test was performed using a MTS QTest-25, universal testing machine following the ASTM D5045 standard at room temperature (~23°C) and quasi-static conditions using displacement control. The test setup has been illustrated in Fig. 3.4. Load and displacement readings were recorded at regular intervals until the samples fractured.

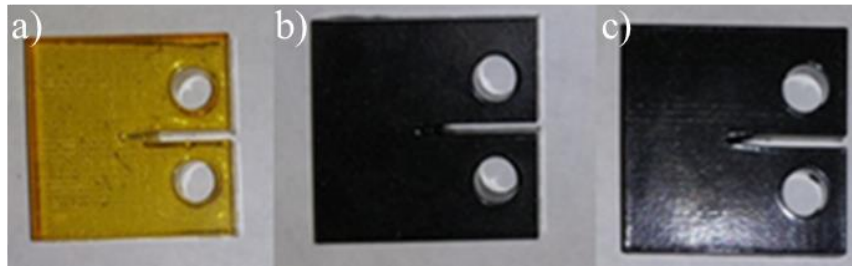


**Figure 3.2** CT samples after curing process (a) Baseline (b) 0.1 wt% and (c) 0.5 wt% NGP

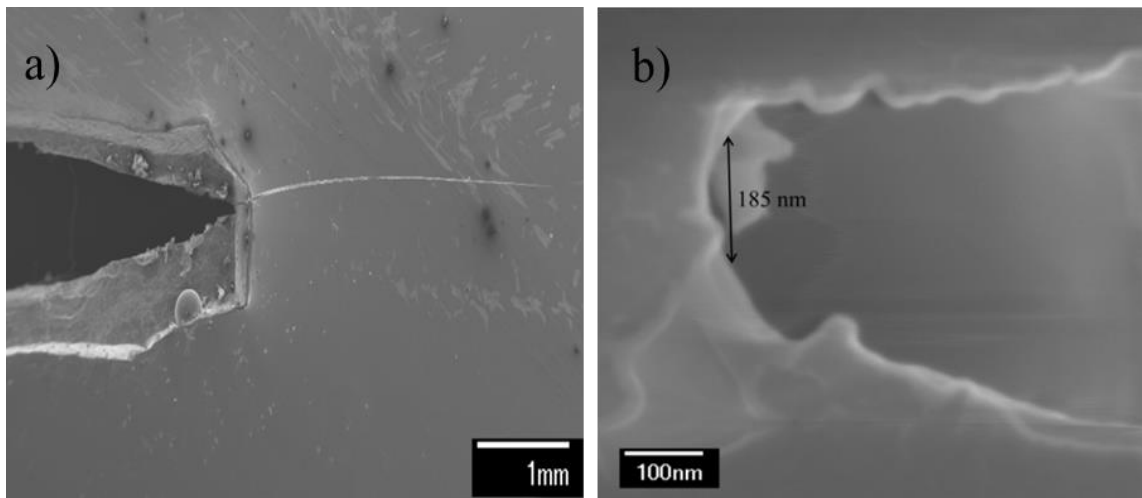


**Figure 3.3** SEM image showing a) Pre-crack created by tapping b) Magnified pre-crack tip

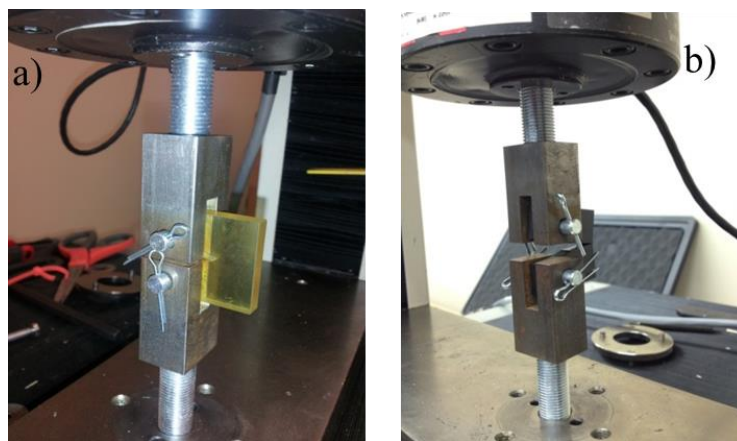


**Figure 3.4** CT test setup (a) baseline (b) 0.1 wt% NGP

Two sets of testing were done. For the first (*unaged*) set of specimens, CT testing was done without any exposure to aggressive environments. For the second (*aged*) set, moisture absorption experiments on CT specimens (baseline, 0.1 wt% and 0.5 wt %) mentioned above were done to observe the behavior of these specimens when exposed to aggressive environments (60°C and 90 % RH) for moisture saturation and then CT testing was done to compare with the *unaged* dataset results.

### 3.3 Results and Discussion

Dispersion of the NGP in the epoxy matrix was analyzed using Transmission Electron Microscopy (Hitachi H-7650 TEM) in 0.1wt% and 0.5 wt% samples. Good dispersion and random orientation with some agglomeration of the graphene platelets for the higher wt% was observed as depicted in Fig. 3.5.

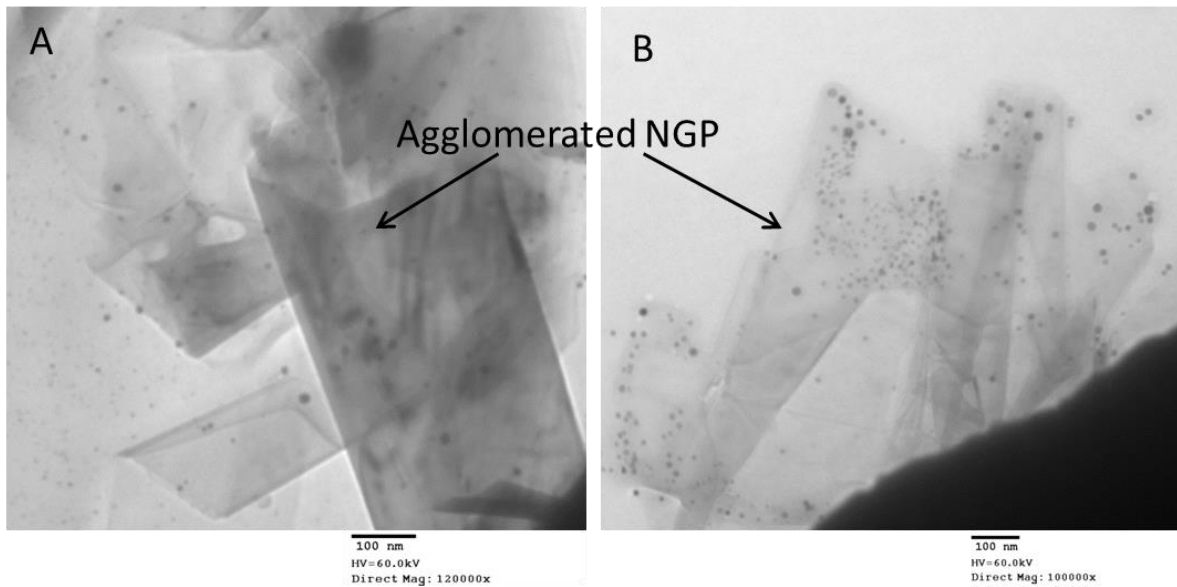


**Figure 3.5** TEM image showing nanographene platelet dispersion in (A) 0.1 wt%, (B) 0.5 wt% NGP reinforced samples

### 3.3.1 Unaged Set Results

Table 3.1 compares the fracture loads and critical cross-head displacements for all the CT specimens tested in this study. Although the failure in EPON 862 is fairly brittle, the critical displacement at failure (i.e., displacement corresponding to peak load) exhibited very little scatter for a particular specimen set as shown by the low standard deviation in the table. Fig. 3.6 depicts the corresponding load-displacement plots obtained from CT testing of the three sets of specimens in Table 3.1, i.e., baseline, 0.1wt% and 0.5 wt% NGP, averaged over 4 replicate specimens. Due to the low scatter in critical displacement, only the scatter in the load is depicted through error bars in Fig. 3.6. While the increase in failure load is expected due to the presence of the stronger NGP platelets, the large increase in deformation at failure (ductility) due to the addition of NGP in an otherwise brittle epoxy resin is very much evident in Fig. 3.6, and forms the corner-stone of the nanoscale toughening mechanism that will be discussed in Chapter 6. The pre-cracks introduced by tapping a razor were more or less straight as shown in Fig. 3.3; unevenly cracked samples were not used for the test, in order to maintain self-similar crack propagation. Fracture toughness (Equation 3.1) and energy release rates (Equation 3.2) were calculated for all the test cases using ASTM D5045 protocol, and pre-crack length was included in the calculations. Details of the calculation are provided below [120].

$$K_{IC} = (P_q / BW^{1/2})f(x) \quad (3.1)$$
$$f(x) = \frac{(2+x)(0.886 + 4.64x - 13.32x^2 + 14.72x^3 - 5.6x^4)}{(1-x)^{3/2}}$$

Where,  $P_q$  is the peak fracture load,  $B$  is the specimen thickness,  $W$  is the specimen width,  $a$  is the crack length including the pre-crack, and  $x=a/W$ .

$$G_{IC} = U / (BW\phi) \quad (3.2)$$

$$\phi = \frac{(1.9118 + 19.118x - 2.5122x^2 - 23.226x^3 + 20.54x^4)(1-x)}{(1.9118 - 5.0244x - 69.678x^2 + 82.16x^3)(1-x) + 2(1.9118 + 19.118x - 2.5122x^2 - 23.226x^3 + 20.54x^4)}$$

Where U is the strain energy, obtained from the load displacement plot during experimentation and  $\phi$  is the energy calibration factor.

**Table 3.1** Fracture Load - Critical Displacement Data Comparison

		Specimen	Specimen	Specimen	Specimen	Average
		1	2	3	4	
<b>Baseline</b>	<b>Fracture Load (N)</b>	95.7	83.17	92.94	85.96	89.45 ±5.08
	<b>Crit. Disp. (mm)</b>	0.243	0.234	0.229	0.235	0.235 ±0.005
<b>0.1 wt%</b>	<b>Fracture Load (N)</b>	238.09	299.49	200.41	208.78	215.75 ±38.86
	<b>Crit. Disp. (mm)</b>	0.432	0.436	0.445	0.447	0.44 ±0.006
<b>0.5 wt%</b>	<b>Fracture Load (N)</b>	250.65	281.35	254.03	255.37	260.35 ±12.24
	<b>Crit. Disp. (mm)</b>	0.53	0.537	0.528	0.545	0.535 ±0.007

Table 3.2 and 3.3 compare the changes in fracture toughness ( $K_{IC}$ ) and critical energy release rates ( $G_{IC}$ ) respectively for each specimen type tested. The addition of NGP to the baseline epoxy system resulted in a sharp increase in the  $K_{IC}$  value from 0.75 MPa.m<sup>1/2</sup> (baseline) to 1.82

MPa.m<sup>1/2</sup> for 0.1 wt%, and 2.25 MPa.m<sup>1/2</sup> for 0.5 wt% NGP addition. The G<sub>IC</sub> value also show a similar increase, from 317 J/m<sup>2</sup> (baseline) to 1422 J/m<sup>2</sup> for 0.1 wt% and 2125 J/m<sup>2</sup> for 0.5 wt% NGP addition. In order to obtain a benchmark, the measured test data are compared with values from experimental data for a different thermoset epoxy (Epoxy 2000) system [95]. The reference reports an increase in the fracture toughness of 65% and an increase in fracture energy of 115%,

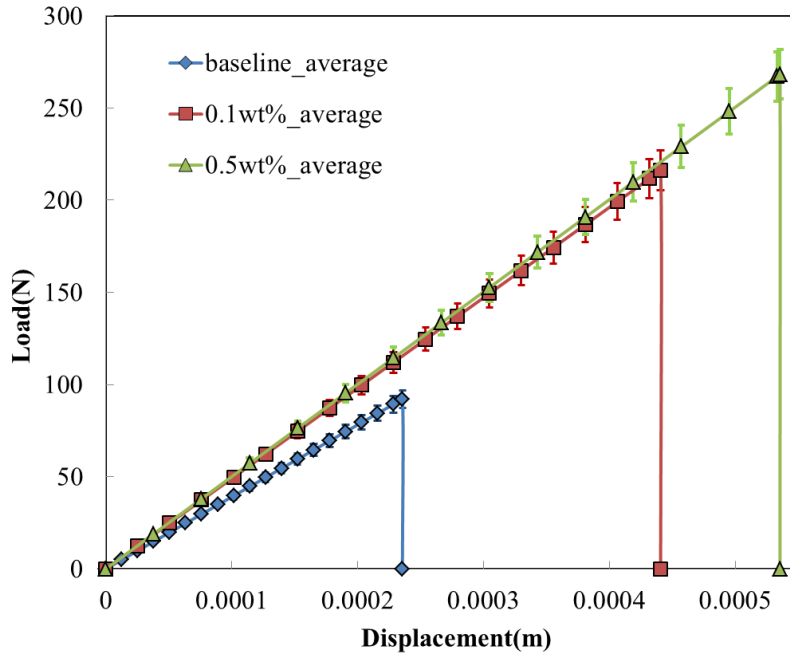


**Figure 3.6** Experimental Load-displacement plot comparison for *unaged* specimens

**Table 3.2** Average Fracture Toughness (K<sub>IC</sub>) Comparison

	Average K <sub>IC</sub> (MPa.m <sup>1/2</sup> )	% improvement	Comparison with reference [95] (MPa.m <sup>1/2</sup> )
<b>Baseline</b>	0.75±0.04	-	1.03
<b>0.1 wt%</b>	1.82±0.32	142 %	~1.7
<b>0.5 wt%</b>	2.25±0.13	200 %	~1.1

**Table 3.3** Average Fracture Energy ( $G_{IC}$ ) Comparison

	Average $G_{IC}$ ( $J/m^2$ )	% improvement	Comparison with reference [95] ( $J/m^2$ )
<b>Baseline</b>	317±74	-	325
<b>0.1 wt%</b>	1422±394	347 %	~600
<b>0.5 wt%</b>	2125±22	568 %	~410

for a functionalized NGP loading of 0.125 wt%, with a decrease in these properties for higher NGP loadings [95]. As can be seen from Table 3.2 and 3.3, the obtained test data agree quite well with the baseline fracture toughness and fracture energy data reported in reference [95], and are in a similar range for the 0.1 wt% NGP case. Further, the obtained toughness data show monotonic increase in the 0.1 to 0.5 wt% NGP range, which is in contrast to as reported in reference [95]. To find evidence for this large increase in fracture properties, fractography analysis was performed. The fracture surfaces were prepared for the analysis by coating the surface with a nanometer thick layer of sputtered gold coating. The surfaces were then observed under SEM (JEOL 7000 FE SEM) with an accelerating voltage of 15 kV.

Fig. 3.7 shows the increased fracture surface roughness of the epoxy fracture specimens due to the addition of the NGP. This is likely due to crack deflection from the presence of NGPs, which makes the cracks deviate from a simple Mode I crack to a mixed mode crack. Mixed mode cracks generally require more energy to propagate [121]. In addition, increased fracture surface leads to greater absorbed energy for surface creation.

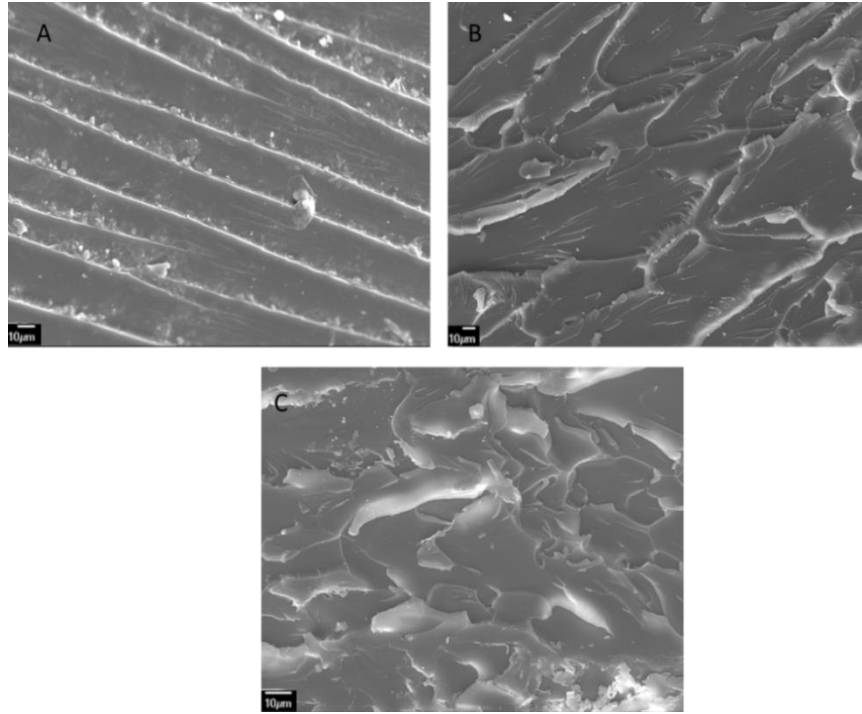


**Figure 3.7** SEM image showing fracture surface roughness comparison (A) baseline (B) 0.1 wt% (C) 0.5 wt% NGP

Surface roughness studies are sometimes used to quantify crack deflection [95]. Roughness parameter ( $R_a$ ) is the most generally used amplitude parameter used to measure the arithmetic average of the vertical deviations from a reference surface. To quantify the effect of the crack deflection in increasing the fracture energy required for crack propagation, post-fracture AFM was performed using AfmWorkshop on the baseline, 0.1 and 0.5 wt% NGP fracture specimens. A set of four random locations close to fracture initiation site were chosen on each sample to minimize statistical errors, and surface roughness was measured for the three NGP loadings.

Fig. 3.8 shows specific AFM scans for a  $27\ \mu\text{m} \times 27\ \mu\text{m}$  scan area for each of the three specimens to provide a visual depiction of increasing surface roughness from baseline to 0.5 wt% NGP specimens. Table 3.4 lists the increase in roughness parameter with the increase in the NGP wt%. Table 3.4 also lists the roughness parameter values for the Epoxy 2000/graphene

system reported in reference [95] for comparison. As can be observed, the fracture surface roughness increases by 150% for 0.1wt% NGP, and 260% for 0.5 wt% NGP. The roughness statistics are similar to the values in reference [95] but the roughness does not achieve a saturation level as reported in the same document [95]. The deviations from [95] can be attributed to completely different cure cycles and the preparation and dispersion of NGPs. Also, Table 3.4 shows that the obtained average roughness parameters are higher than that reported in the literature for the other epoxy system, indicating greater crack deflection (tilting and/or twisting of the crack front) in EPON 862 with NGP [95].

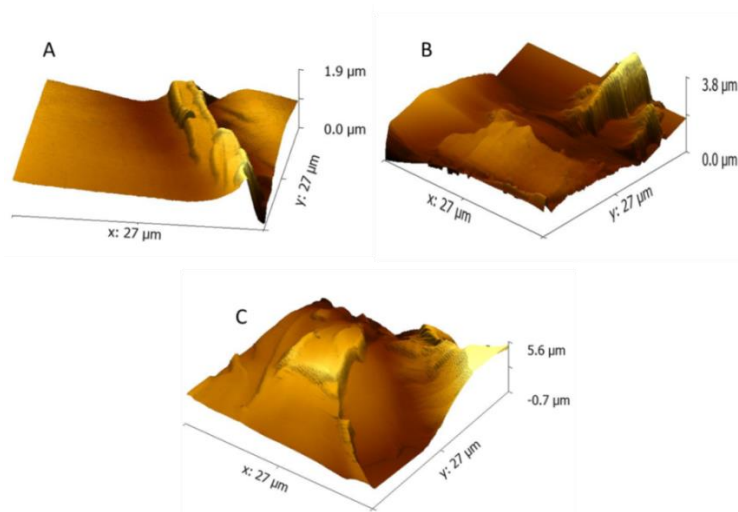


**Figure 3.8** AFM fracture surface roughness study (A) baseline (B) 0.1 wt% (C) 0.5 wt% NGP

**Table 3.4** Average Surface Roughness (Ra) comparison

	<b>Roughness parameter (Ra, <math>\mu\text{m}</math>)</b>	<b>% increase</b>	<b>Comparison with reference [95] (Ra, <math>\mu\text{m}</math>)</b>
<b>Baseline</b>	0.168 $\pm$ 0.03	-	$\sim$ 0.17
<b>0.1 wt%</b>	0.426 $\pm$ 0.15	153 %	$\sim$ 0.3
<b>0.5 wt%</b>	0.608 $\pm$ 0.1	262 %	-

Other contributors to the toughening mechanism were also observed during fractography. Fig. 3.9 shows evidence of graphene platelet pullout on the fracture surfaces of the nano-reinforced specimens. However, unlike in CNT reinforced epoxy, the evidence of NGP pullout were rare, which can be because only a very small weight percent of the NGP has been used in the study.

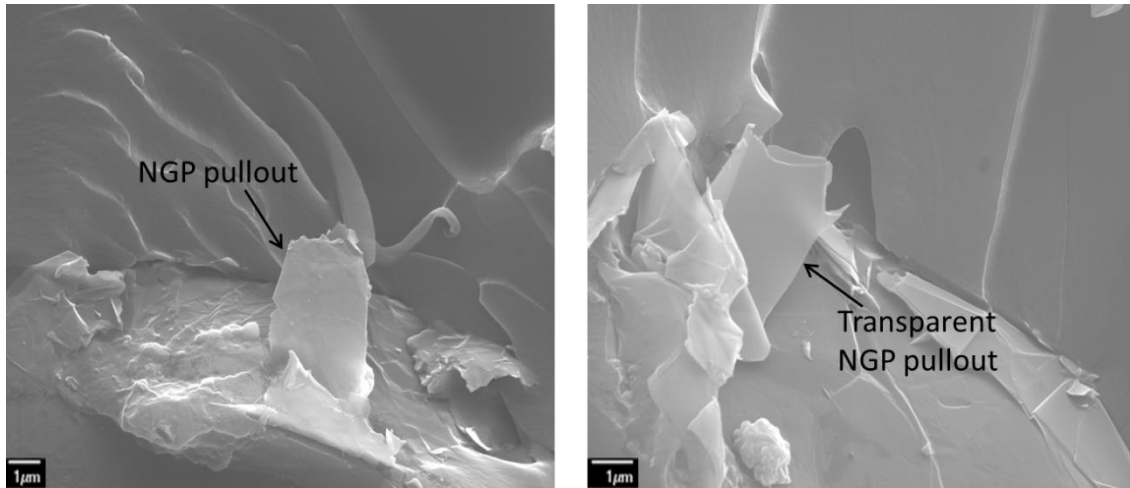


**Figure 3.9** SEM image showing graphene platelet pull-out in 0.1 wt% NGP fracture surface

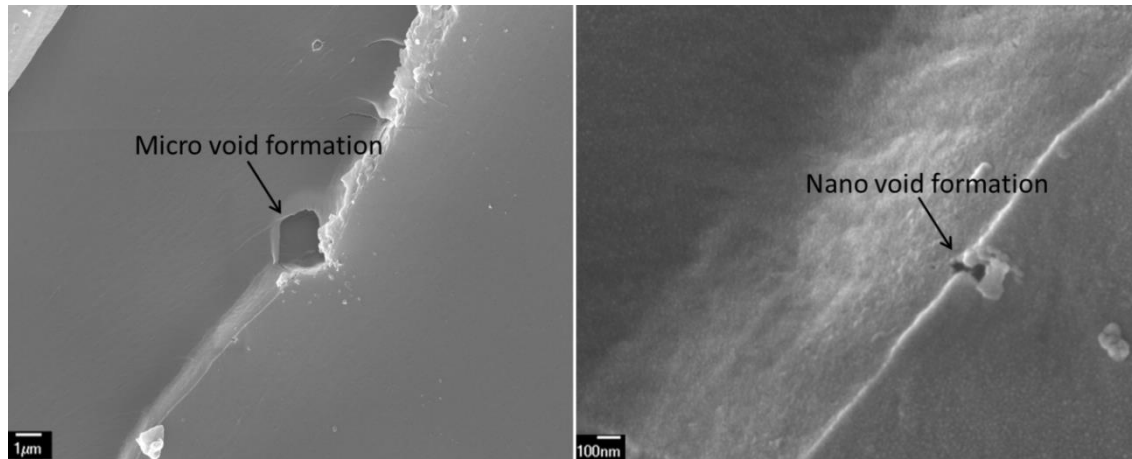


**Figure 3.10** SEM image showing void formations in 0.1 wt% NGP fracture surface

Void formation was also evident in NGP reinforced samples. Fig. 3.10 depicts formations of voids which vary in sizes from a few microns to a few nanometers. The voids occur solely along the river marks created due to crack propagation that, in conjunction with the sharply polygonal shape of the voids, indicates that the voids are not an artifact of the manufacturing process. The results reiterate the fact that local matrix plastic deformation and particle matrix debonding could be another possible reason for dramatic toughness enhancements. Although cases of crack pinning were not distinguishable in the study, it could still be a minor contributor in the toughness enhancement observed. The next chapter will discuss manufacturing of composite laminates using carbon fiber motivated by this significant increase in fracture toughness of the EPON 862 matrix reinforced by hydrogen passivated NGPs to investigate the changes in fracture toughness for laminates. It should be noted that no passivation of the NGPs was done for Mode I characterization experiments presented in this chapter.

### 3.3.2 Aged set results

Fig. 3.11 shows the moisture diffusion plots for the CT specimens. It is clear that with increasing wt% of NGPs in the specimens, the weight gain is drastically reduced. Table 3.5 compares the average saturation moisture uptake for the three types of CT specimens, which clearly shows a

1.42% moisture uptake for 0.5 wt% NGP reinforced CT specimen compared to a 1.57% moisture uptake for baseline CT specimens.

After moisture uptake saturation, the aged samples were tested for fracture properties using CT testing. Fig. 3.12 shows the averaged load-displacement plot for aged CT specimens. Even after aging, the NGP reinforced specimens exhibit higher fracture loads and fracture strains than the baseline specimens.

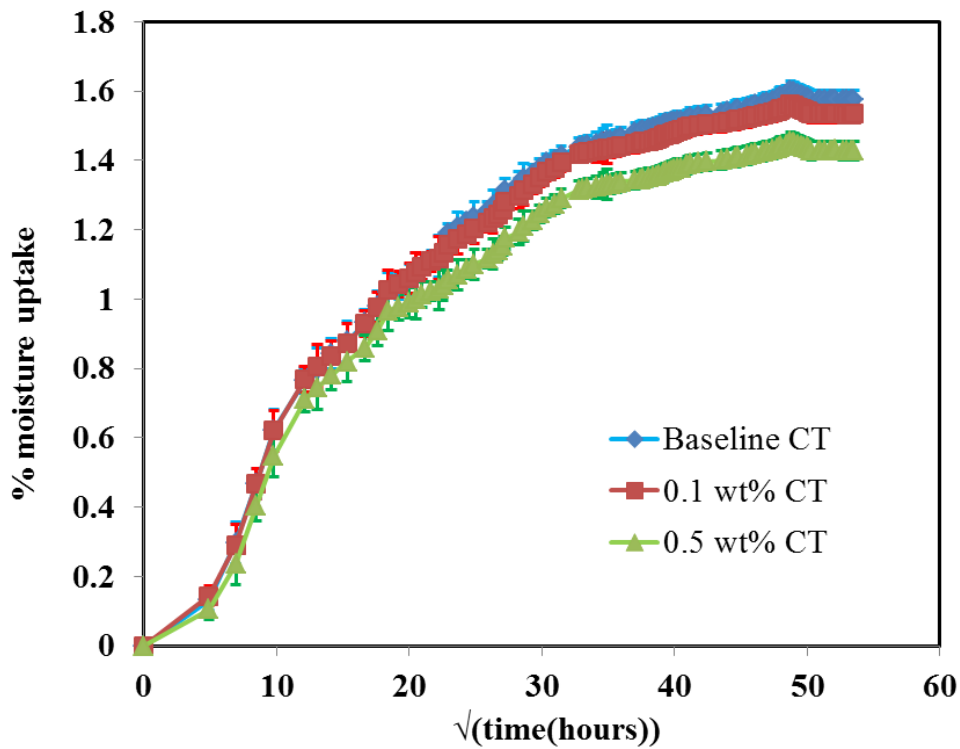


**Figure 3.11** Comparison of moisture uptake of CT specimens

**Table 3.5** Saturation moisture uptake comparison for *aged* CT specimens

	<b>Initial wt.</b> <b>(gm)</b>	<b>Final wt.</b> <b>(gm)</b>	<b>Saturation moisture</b> <b>uptake %</b>
<b>Baseline</b>	6.04	6.134	1.57%
<b>0.1 wt%</b>	6.412	6.511	1.53%
<b>0.5 wt%</b>	6.431	6.522	1.42%

Surprisingly, the slope of the load-displacement plots for the aged specimens was higher than the corresponding unaged specimens. This has been depicted in Fig. 3.13. The fracture loads for the aged specimens were also higher than the corresponding unaged specimens as can be seen clearly in Fig. 3.13. Table 3.6 provides comparison between the aged  $K_{IC}$  and  $G_{IC}$  values of different specimens, calculated using Eqn. 3.1 and 3.2. The results show that there is a 62 % and 91 % improvement in  $K_{IC}$  value for 0.1 and 0.5 wt% of NGP reinforced CT specimens respectively after aging. This shows the reinforcing potential of the NGPs is maintained even after temperature aging of the specimens. Although the extent of the improvement is not as dramatic (200 % improvement for unaged case for 0.5 wt% NGP), there is still a significant improvement over baseline toughness values. It should also be noted that although there is a considerable improvement in the  $K_{IC}$  value for the aged baseline specimens over unaged baseline cases, the value is still lower than the unaged (and aged) NGP reinforced CT specimens.

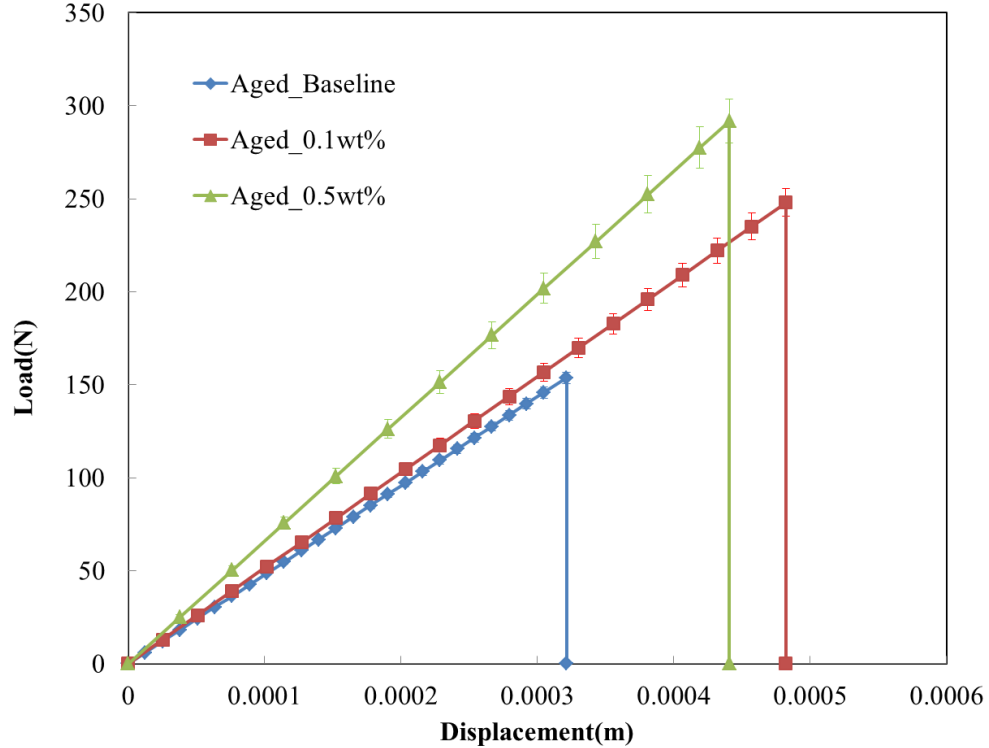


**Figure 3.12** Experimental load-displacement curves for *aged* CT specimens

The change in  $G_{IC}$  values after aging has been presented in Table 3.7. The  $G_{IC}$  values follow a similar trend as the  $K_{IC}$  values, where there is an increase of 143% and 161% for 0.1 and 0.5 wt% of NGP respectively. We can ascertain from the above results that graphene's barrier properties coupled with matrix plasticization gives rise to results observed. Hydrolytic degradation in the matrix due to moisture absorbance during the experiment could be the reason for decrease in fracture properties. The results of  $K_{IC}$  and  $G_{IC}$  from the two sets (unaged and aged) were normalized with respect to the unaged baseline values to summarize the work presented in this chapter. Figs. 3.14 and 3.15 show the normalized comparisons between  $K_{IC}$  and  $G_{IC}$  respectively for the two sets tested.

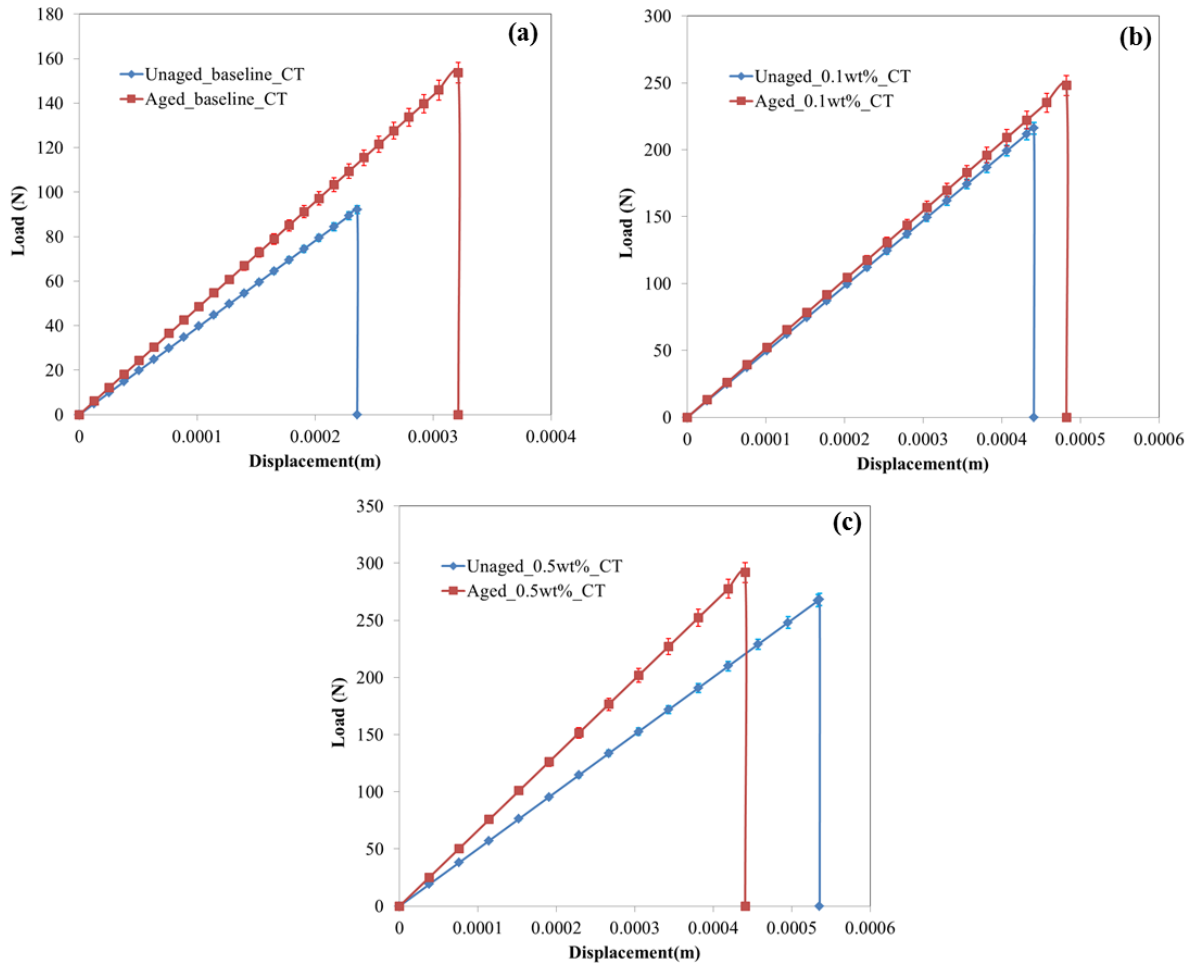


**Figure 3.13** Comparison of averaged load-displacement curves of unaged & aged CT specimens

**Table 3.6** Average  $K_{IC}$  Comparison of aged CT specimens

	Aged ( $MPa \cdot m^{1/2}$ )	% Change
<b>Baseline</b>	1.29±0.05	-
<b>0.1 wt%</b>	2.09±0.1	62.01 %
<b>0.5 wt%</b>	2.47±0.07	91.47 %

**Table 3.7** Average  $G_{IC}$  Comparison of aged CT specimens

	<b>Aged</b> <b>(J/m<sup>2</sup>)</b>	<b>% improvement</b>
<b>Baseline</b>	737±104	-
<b>0.1 wt%</b>	1791±102	143 %
<b>0.5 wt%</b>	1926±133	161 %

In summary, a thermoset polymer (EPON 862) reinforced with NGPs was shown to possess dramatically enhanced fracture properties (fracture toughness and energy release rate) in comparison with the baseline polymer. Remarkable improvements (~200 %) and (~570 %) in the  $K_{IC}$  and  $G_{IC}$  values were recorded for up to 0.5 wt% NGP loading. The likely mechanisms for such high toughness increases are explained through a crack deflection and nano-scale damage formation mechanism which were corroborated with the use of AFM and, taken together with evidence of graphene pull out and void formation using SEM, are deemed to be the major

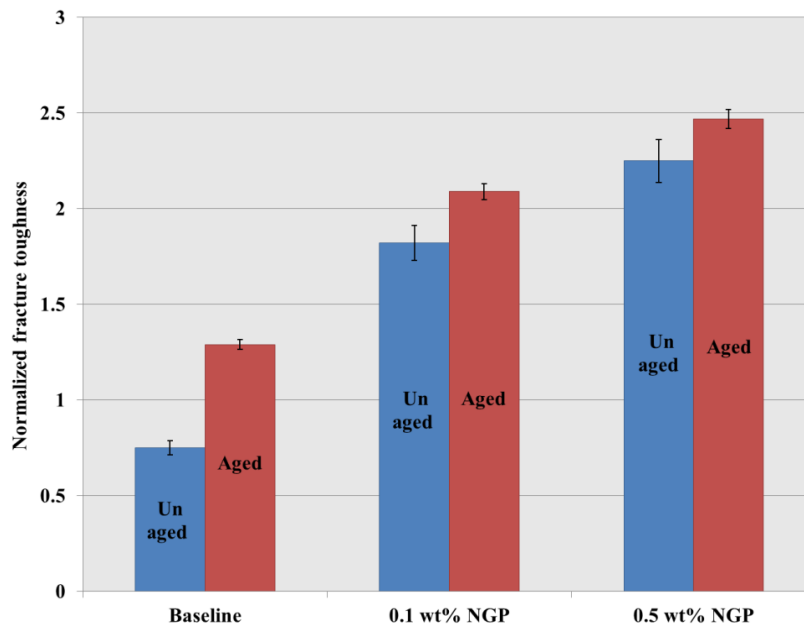


**Figure 3.14** Normalized  $K_{IC}$  comparison of *unaged* & *aged* CT specimens

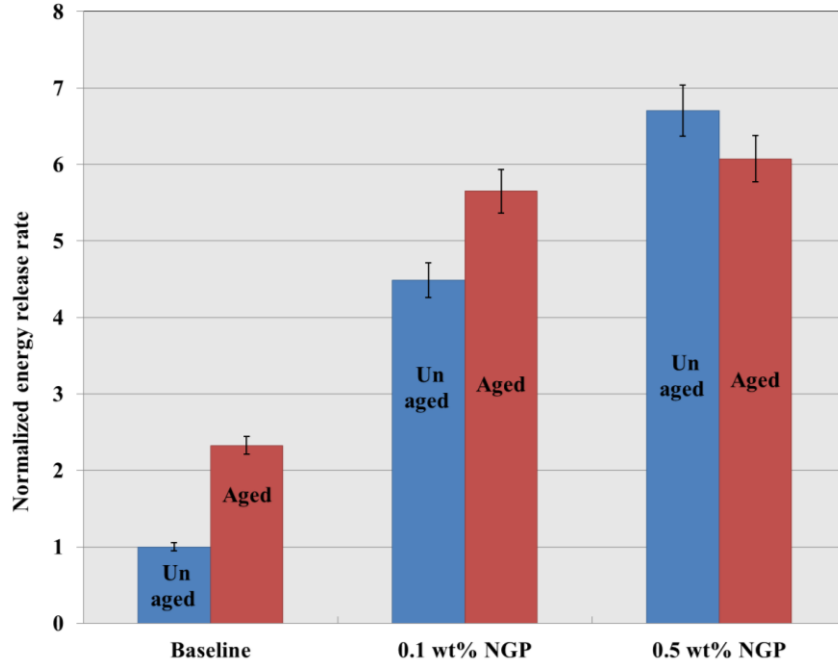


**Figure 3.15** Normalized  $G_{IC}$  comparison of *unaged* & *aged* CT specimens

contributors for the significant increases in the fracture properties. It is also shown that CT specimens exposed to high temperature (60°C) and humidity (90% RH) for a prolonged period of time, exhibit different fracture properties than their unaged counterparts. There is an increase in fracture loads after aging which is counterintuitive, and reasons for this change need to be explored.

The results presented in this chapter clearly indicate that small NGP loadings in EPON 862 thermoset epoxy system leads to significant Mode I toughness improvements in NGP reinforced composite specimens. The next chapter aims to study mixed mode behavior of NGP reinforced EPON 862 system and Mode I delamination of carbon fiber/nanographene reinforced EPON 862 composite to produce high toughness light weight composite laminate structures for large scale aerospace and automobile applications.

## CHAPTER 4

### STUDIES ON THE DISPERSION AND ALIGNMENT OF NANOGRAPHENE IN EPOXY POLYMER

#### **4.1 Summary**

This chapter aims to perform a temperature dependent hydrogen passivation study of NGPs. Four different temperatures were chosen for these studies which are 23°C, 75°C, 300°C, and 450°C. The hydrogen passivated (HP) NGPs were dispersed in ethanol using ultra-sonication. Optical microscopy and TEM studies were conducted to monitor the changes in the dispersion of HP-NGPs with the passivation temperature. Surface area changes, X-ray diffraction results and Raman shift due to passivation were also studied. The motivation for this study comes from the work done in Chapter 3, to improve the dispersion of NGPs in a polymer matrix.

This chapter also lays the foundation of graphene alignment studies motivated by the above model. The chapter investigates the alignment of GNPs in SC780 polymer using an alternating current (AC) electric field. The study was performed for various voltages (100V-200V) and frequency (100 Hz-1 kHz). The electrodes used for analysis were silver, steel and aluminum. Alignment of the NGPs for each case was studied using optical microscopy.

#### **4.2 Materials and Methods**

##### *4.2.1 Materials*

NGPs with an average diameter of 15  $\mu\text{m}$  procured from XG-Sciences Inc. were used in this study. A 95% ethanol solution was used to disperse the NGPs.

#### *4.2.2 Hydrogen passivation setup*

Passivation of graphene was carried out in a tubular furnace at different temperatures (23°C, 75°C, 300°C and 450°C). Typically, a quartz boat with 0.3 g graphene was placed in the tubular furnace and the graphene was baked and passivated, simultaneously, under the flow of a 5% H<sub>2</sub>/N<sub>2</sub> gas mixture. The sample was heated from 23°C to the temperature of interest in 4 hours followed by holding at that temperature for another 2 hours. Room temperature (RT) (23°C) passivation of graphene was performed using the same setup by subjecting graphene to the 5% H<sub>2</sub>/N<sub>2</sub> gas mixture for 6 hours.

#### *4.2.3 Dispersion in ethanol*

0.1 wt% of HP-NGPs were dispersed in 95% ethanol solution using a Branson 450W probe sonifier (20 second pulsed with 10 second intervals) at 40% amplitude for 1 hour run time. The pulsed operation helps to keep the temperature of ethanol low and prevents it from vaporizing during the sonication.

### **4.3 Microscopy Study**

#### *4.3.1 Optical microscopy study*

0.1 wt% HP-NGP dispersed ethanol solution was drop casted on a glass slide to be observed on an optical microscope. Figs. 4.1-4.3 depict the dispersion of the HP-NGPs dispersed in ethanol at different 4x, 10x and 40x magnifications respectively, compared to the unpassivated NGP dispersed in ethanol. It is clearly evident that the 23°C and 75°C passivated NGP exhibit a better dispersion and less agglomeration in ethanol than the unpassivated NGPs. The 23°C passivated NGP shows the best dispersion compared to the unpassivated NGPs in Figs. 4.1-4.3. The HP-NGPs become intercalated and highly agglomerated with further increase in passivation

temperature. This clearly indicates a temperature dependence on dispersion and agglomeration of HP-NGPs.

#### 4.3.2 TEM study

Due to evidence from optical microscopy, that 23°C passivated HP-NGP shows the best dispersion and least agglomeration compared to the unpassivated NGPs, a TEM was used to study the dispersion of these platelets in comparison to the unpassivated NGPs at the micro and nano scales. For the TEM study, 20  $\mu\text{l}$  solution of the dispersed ethanol solution was dropped on formvar coated copper grids and were observed on a Hitachi H-7650 TEM.

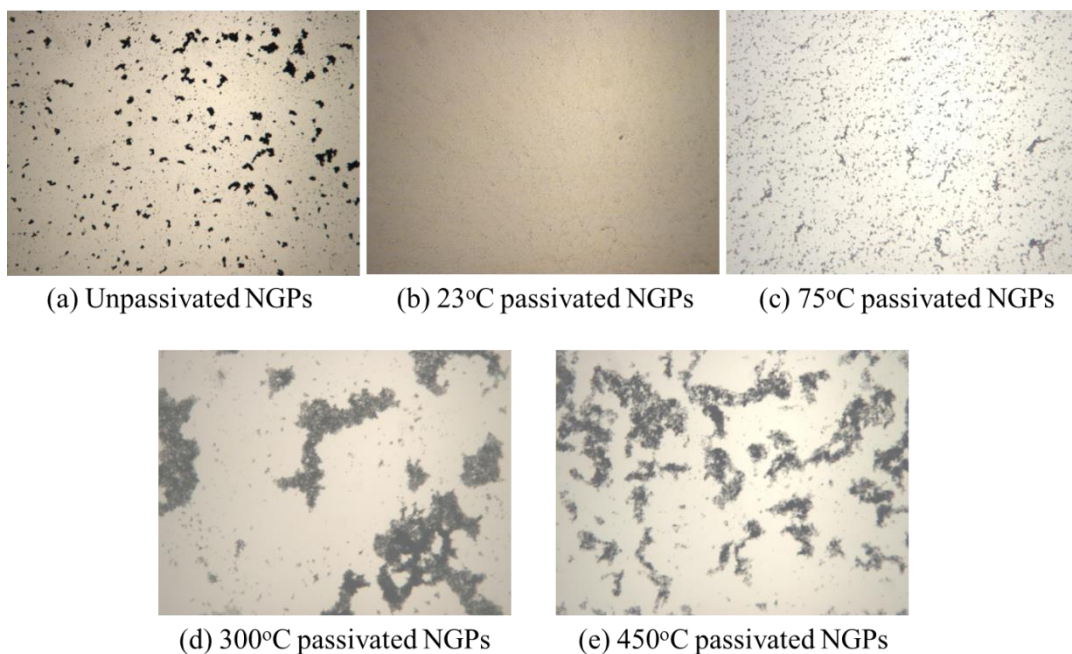


**Figure 4.1** Optical micrograph of drop casted HP-NGPs in ethanol at 4x magnification

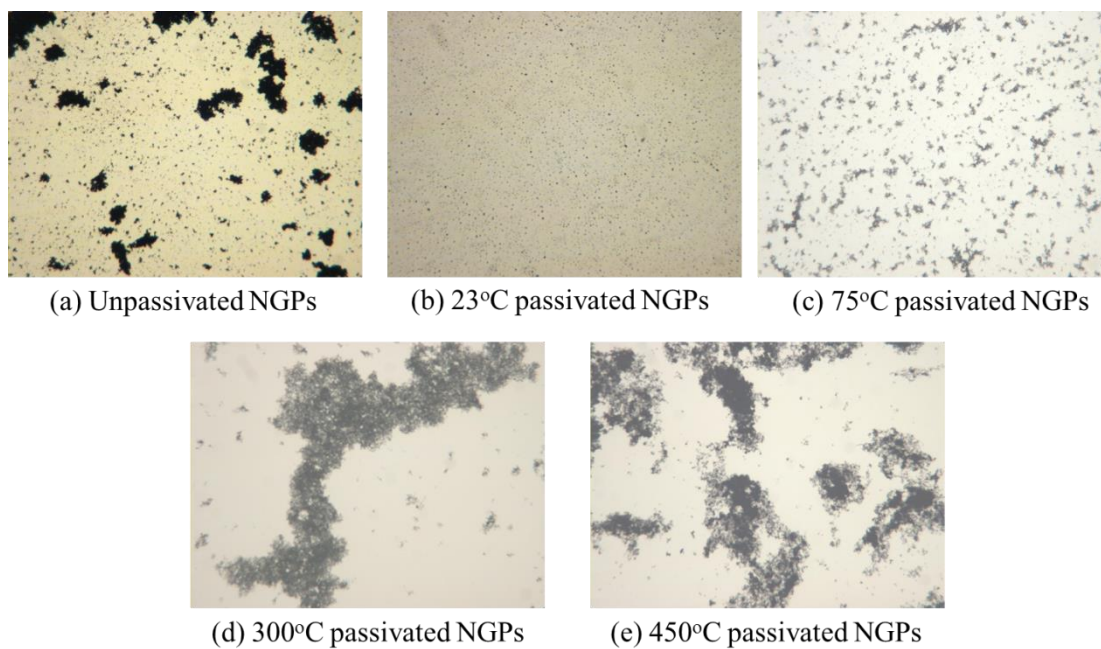


**Figure 4.2** Optical micrograph of drop casted HP-NGPs in ethanol at 10x magnification

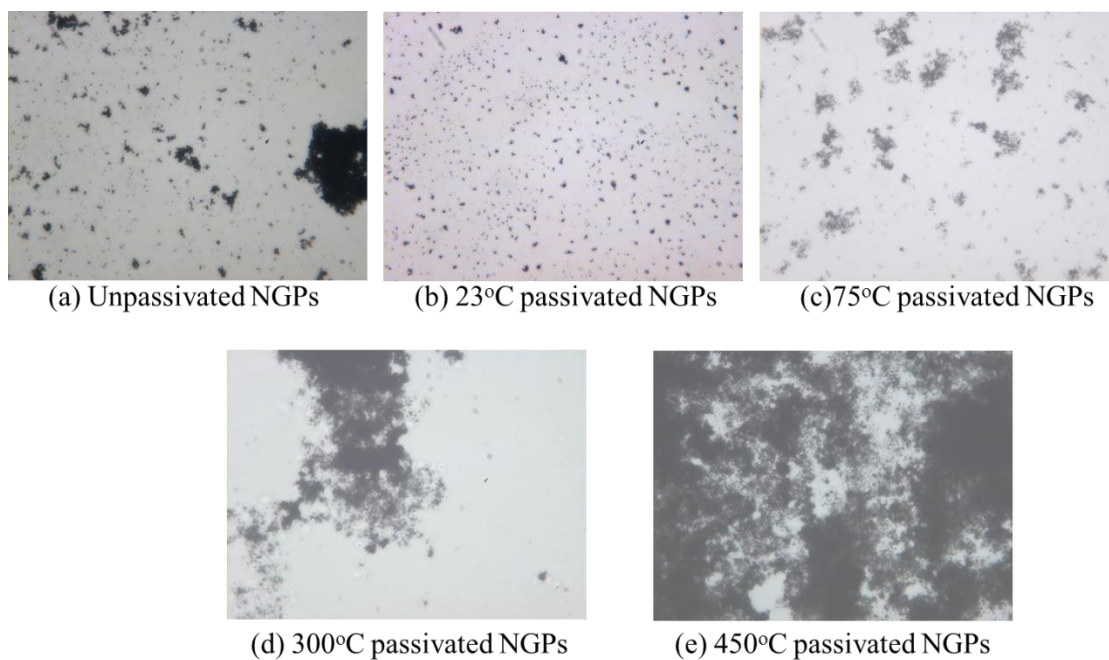
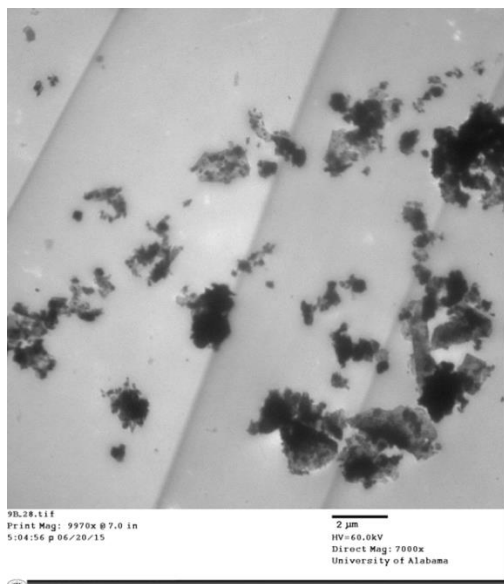
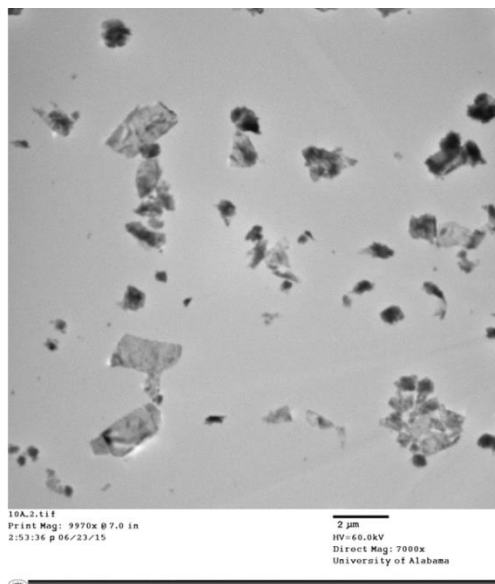


**Figure 4.3** Optical micrograph of drop casted HP-NGPs in ethanol at 40x magnification

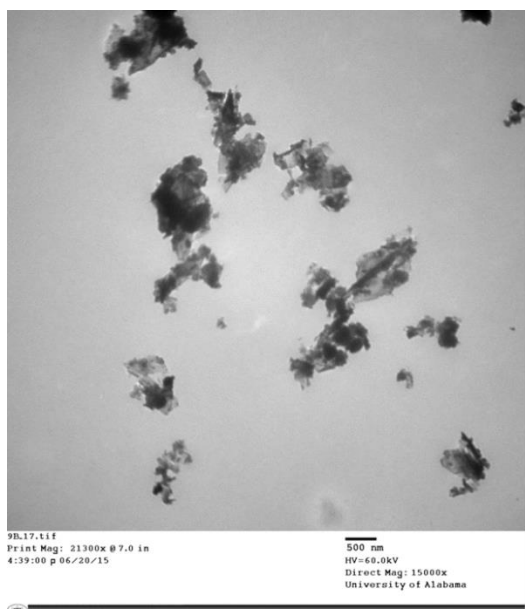


Unpassivated NGPs

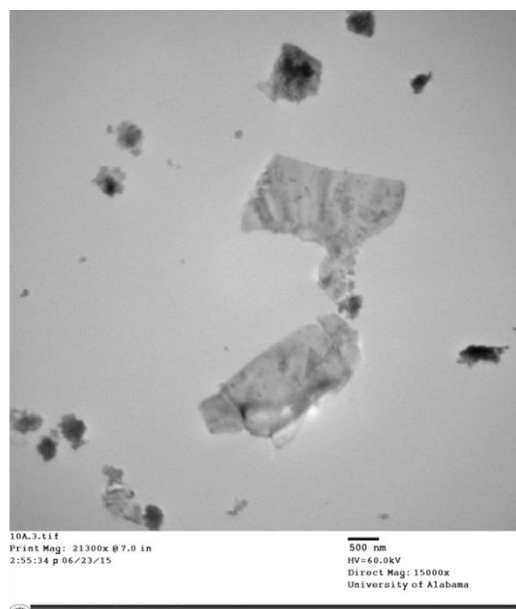


23°C passivated NGPs

**Figure 4.4** TEM micrograph of unpassivated and passivated NGP in ethanol (2 micron scale)



Unpassivated NGPs



23°C passivated NGPs

**Figure 4.5** TEM micrograph of unpassivated and passivated NGP in ethanol (500 nm scale)

Figs. 4.4 and 4.5 show the micro scale and nano scale dispersions respectively of the 0.1 wt% of 23°C passivated NGPs compared to the unpassivated NGPs in ethanol. It is again evident from

the TEM analysis that the hydrogen passivation of the NGPs at 23°C drastically improves the dispersion of the NGPs in ethanol. Although a little agglomeration is observed, it is much less than the unpassivated NGPs in ethanol.

#### 4.4 Analysis of hydrogen passivated NGPs

To understand the reasons behind the different agglomeration and dispersion patterns and role of temperature during hydrogen passivation, HP-NGPs were studied using techniques like N<sub>2</sub> physisorption measurements, Raman spectroscopy, powder X-ray diffraction (XRD).

The Nitrogen (N<sub>2</sub>) physisorption measurements were recorded on a Quantachrome Nova 2200e pore size analyzer at -197°C with Helium mode to determine surface area and void volume of

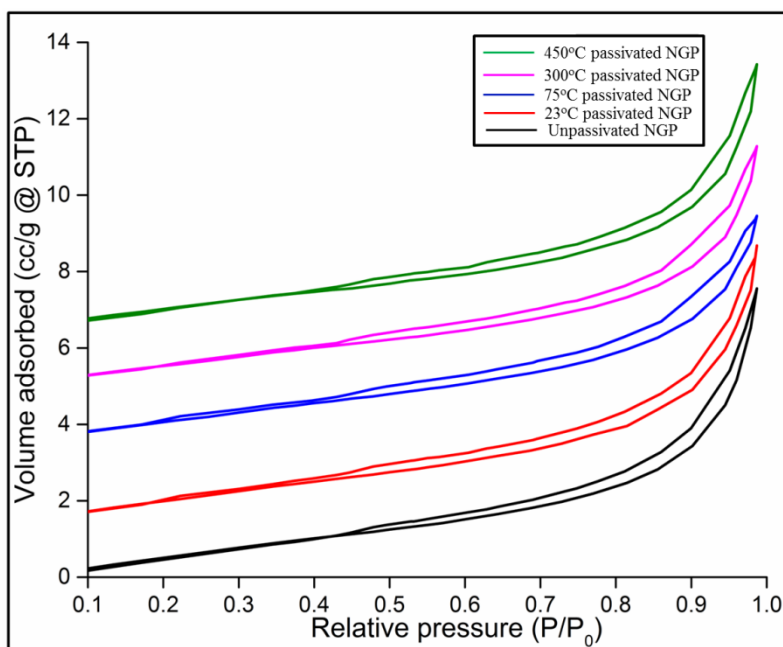


**Figure 4.6** N<sub>2</sub> adsorption-desorption isotherms for different temperature HP-NGPs

the NGPs, respectively. Interpretation of the isotherms obtained was done with Quantachrome NovaWin software version 11.1 (NL-DFT), and the Barrett-Joyner-Halenda (BJH) method was applied to the adsorption branch to calculate the pore size and the Brunauer–Emmett–Teller (BET) method was utilized for the calculation of the surface area. Fig. 4.6 shows the N<sub>2</sub>

adsorption-desorption isotherms obtained using this analysis. The hysteresis loop between the adsorption and desorption branches in the  $P/P_0$  range of 0.45-0.9 demonstrated the presence of mesopores in all the samples. It is evident that the volume of  $N_2$  adsorbed by the HP-NGPs increases with the increase in the temperature of passivation. Table 4.1 shows the surface area ( $S_{BET}$ ) and pore size measurements obtained using BET and BJH methods respectively. The table shows a monotonic decrease in surface area and the pore diameter and hence a decrease in the total pore volume of the NGPs with increasing temperature of hydrogen passivation. Pristine graphene (un-passivated) gave a specific surface area of  $828.8 \text{ m}^2/\text{g}$  which decreased to  $748.5 \text{ m}^2/\text{g}$  for GR-RT (NGP passivated at  $23^\circ\text{C}$ ). This analysis shows that the reinforcing potential of the NGPs might be reduced since the surface area of the NGPs is being reduced.

**Table 4.1** BJH and BET analysis using  $N_2$  adsorption isotherm for different temperatures

<b>Sample</b>	<b><math>S_{BET}</math> (<math>\text{m}^2/\text{g}</math>)</b>	<b><math>V_{total}</math> (<math>\text{cc/g}</math>)</b>	<b>Pore diameter<sub>BJH</sub> (<math>\text{nm}</math>)</b>
<b>Unpassivated NGP</b>	828.8	0.6447	5.0476
<b>23°C passivated NGP</b>	748.5	0.5842	4.4776
<b>75°C passivated NGP</b>	515.7	0.4111	4.1656
<b>300°C passivated NGP</b>	407.2	0.3265	4.1502
<b>450°C passivated NGP</b>	291.8	0.2353	4.181

Powder X-ray diffraction (XRD) measurements were performed on a Bruker D8 Discover with GADDS (General Area Detector Diffraction System) (wavelength  $\text{Co K}\alpha$ ,  $1.79 \text{ \AA}$ ) and a Hi-Star area detector. Fig. 4.8 shows the XRD profiles obtained for the different HP-NGPs. An intense peak centered at  $\sim 2\theta = 30^\circ$  (wavelength  $\text{Co K}\alpha$ ,  $1.79 \text{ \AA}$ ) corresponds to C (002) peak in graphite

with an interlayer distance  $\sim d = 3.37 \text{ \AA}$  for all NGPs. Graphene samples obtained at various passivation temperatures showed an increasing shift towards lower  $2\theta$  values with an increase in the passivation temperature. Applying the Debye-Scherrer equation for calculation of crystallite sizes for the HP-NGPs shows a peculiar trend in these sizes. The average crystallite size of unpassivated NGPs was calculated to be 17.1 nm which decreased to 16.2 nm and 15.8 nm for GR-RT and GR-75 respectively. On the contrary, increase in the passivation temperature increase the crystallite size of graphene to 16.5 nm and 17.1 nm for GR300 and GR450, respectively. This is in agreement with the increasing agglomeration observed for HP-NGPs at 300 C and 450 C in Figs. 4.1-4.3. Table 4.2 shows the average crystallite sizes for the different temperature HP-NGPs.

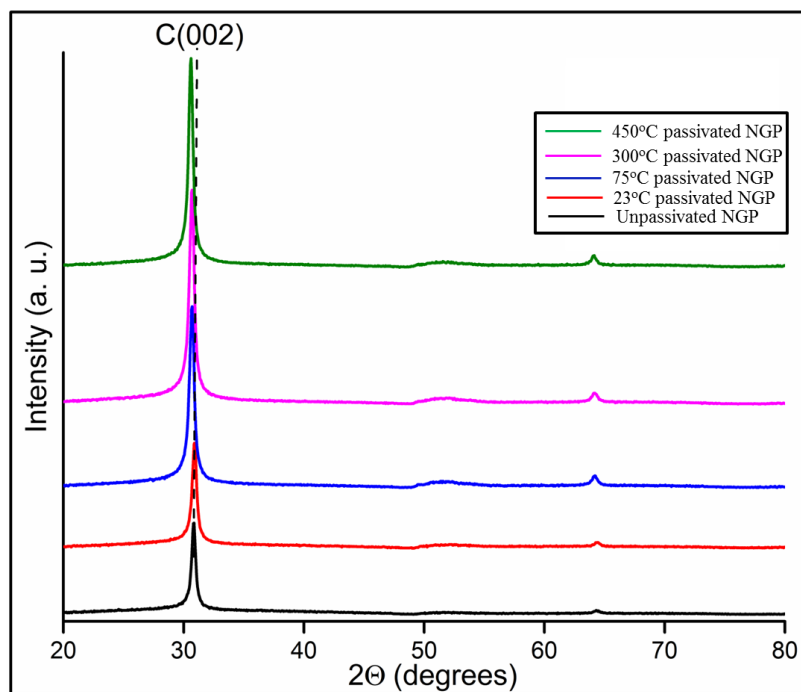


**Figure 4.7** XRD analysis of different temperature HP-NGPs

**Table 4.2** Crystallite size calculation for different temperature HP-NGPs

<b>Sample</b>	<b>Average crystallite size (nm)</b>
<b>Unpassivated NGP</b>	17.1
<b>23°C passivated NGP</b>	16.2
<b>75°C passivated NGP</b>	15.8
<b>300°C passivated NGP</b>	16.5
<b>450°C passivated NGP</b>	17.1

The Raman spectroscopy was conducted using a Jobin-Yvon HR800 UV confocal microscope. The excitation line at 632.81 nm came from a He-Ne laser with approximately 12 mW of power at the analyzed samples of HP-NGPs. The shifts were detected using a Peltier cooled CCD detector. The image used a 10× objective lens and scanned around the center of the NGPs. Fig. 4.8 shows the G band and D bands obtained from the Raman spectroscopy for different NGPs. There is a slight shift in the G band with increasing temperature of hydrogen passivation of the NGPs which points to a decreasing number of layers of graphene present due to increasing temperature of the passivation [97].

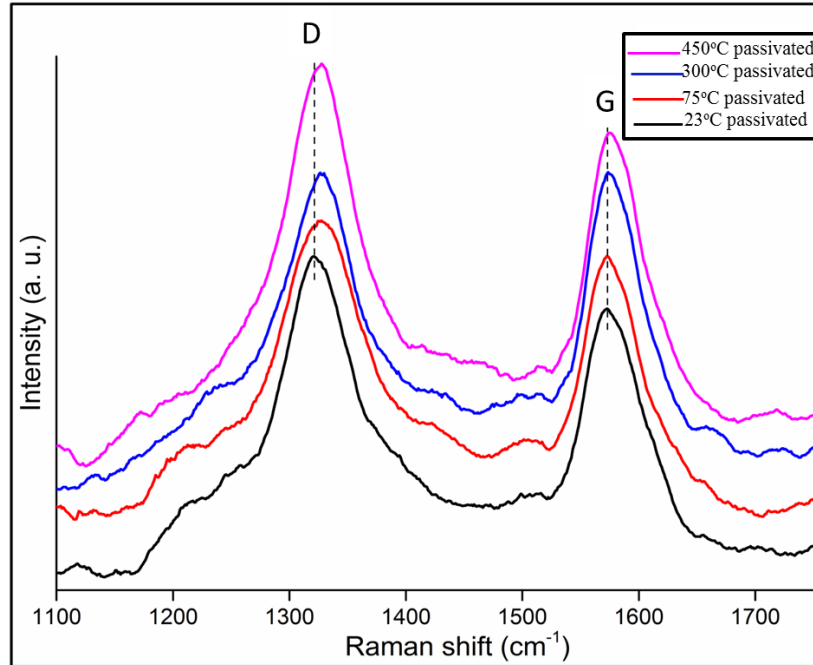


**Figure 4.8** G and D bands obtained using Raman spectroscopy of HP-NGPs

The above discussion explains the work done to improve the dispersion of NGPs in ethanol. This gives confidence that hydrogen passivation is a great technique to improve the overall dispersion of NGPs in polymer matrices to extract full potential of the NGPs. The HP-NGPs at 23°C will be used in the next chapter to study Mode I and mixed mode fracture properties of epoxy composites.

#### 4.5 Graphene alignment study

Specific tailoring of composites by controlling the orientation of carbon nanoparticles such as CNTs, carbon black and nanofibers in polymers has been investigated in detail by various research groups. Park et al conducted a series of experimentation on aligning SWCNTs [122]. They observed that CNTs are aligned in an epoxy under alternating current (AC) sources, which increased the dielectric properties and conductivity of the composite. The group also performed an applied voltage and frequency study to observe the dependence of alignment on these factors.

The degree of alignment of carbon nano particles is highly dependent on the source used for alignment.

Different sources ranging from Electric Field (EF), Magnetic Field (MF) and combined EF+MF have been used to obtain a higher degree of alignment [122-125]. Chen et al prepared highly oriented SWCNT samples in ethanol at a frequency of 5 MHz [123]. Romyen et al showed that the application of a MF in conjunction with an EF enhances the level of alignment as compared to using only an EF or MF [125]. AC and Direct Current (DC) EF have been used repetitively for this task for its ease of application. AC EF has proved to be the better alternative to DC fields on multiple experiments. Kumar et al showed that applying a DC field induces movement of CNTs towards the positive electrodes leading to an aggregation of particles towards this end [126]. Martin et al showed that the aligned network formation using an AC EF was more uniform and aligned in comparison to a DC EF [127].

Mechanical property enhancements by aligning inclusions in an epoxy matrix have also been documented. Kim et al showed that aligned ceramic and glass fiber inclusions in an epoxy composite gives an increase of 27.3% in Young's modulus between transversely oriented and randomly oriented specimens. They also show a more dramatic increase of 69.6% in Young's modulus for a longitudinal alignment of inclusions [128]. Ladani et al showed that addition of 1.6 wt% of aligned carbon nano fibers in an epoxy increases the electrical conductivity by about seven orders of magnitude and increases the fracture energy  $G_{IC}$  by 1600%, compared to a 5-fold increase in electrical conductivity and 27% increase in  $G_{IC}$  for randomly oriented carbon nano fibers [129].

Graphene is an emerging nano filler being increasingly researched for structural and electrical applications. Being one of the most highly conductive materials on Earth, graphene is highly

susceptible to orientation changes when subjected to electric fields, like its other counterparts such as CNTs and hence would be ideal to produce high quality aligned nano composites for a variety of applications. Chen et al showed five to seven orders of electrical conductivity improvements in a polymer composite when graphite flakes were aligned using an AC EF [124]. Wang et al also demonstrated orientation of graphite nano sheets by DC EF, which showed significant improvements in visible light transmittance [130]. Recently, Wu et al showed that tailoring NGP composites using an AC electric field, gives remarkable results (up to 7-8 orders of magnitude improvement in electrical conductivity, and nearly 900% increase in Mode I fracture toughness) when compared to unaligned composites [131]. Still, a gap exists in the experimental study of the alignment of NGPs in a polymer matrix and its dependence on the type of electrodes used, electrode spacing, electric field intensity and frequency.

This section studies graphene alignment in SC-780 polymer using an AC electric field, and presents a study between different metals (Silver, Aluminum, Steel) used as electrodes, frequency range of 100 Hz-1 kHz and voltage range of 100V-200V for a 5mm electrode spacing, and compares which would be most adequate setting for alignment of graphene for fracture property enhancement purposes.

#### *4.5.1 Devices for initial testing*

For this study, three different types of devices were fabricated. Fig. 4.9 shows the three devices, which differ in the type of electrodes used. The electrodes used were silver, aluminum and steel. The electrodes were joined to a glass substrate using an epoxy adhesive with a 5 mm gap. The total device area was fixed as 625 mm<sup>2</sup>, with the electrode dimensions being 25 mm x 10 mm. The thickness of the electrodes was .025 mm for each device.

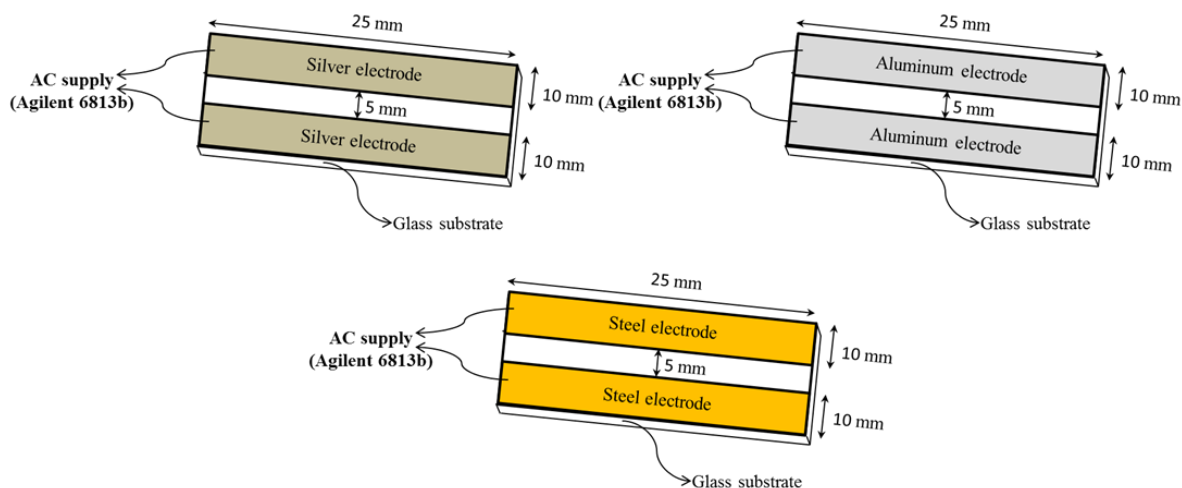


**Figure 4.9** Devices fabricated for initial alignment

#### 4.5.2 Graphene dispersion and electric field application

A 0.05 wt% NGP suspension was prepared in SC-780 resin using a shear mixer for 1 hr. An Agilent 6813b AC source was used to generate three different electric field intensities, 20kV/m, 30kV/m and 40kV/m, corresponding to applied voltages of 100V, 150V and 200V respectively. Three different frequencies were used 100 Hz, 500 Hz and 1 kHz, for each case, which gives 27 cases in total to be studied, 9 for each device. Fig. 4.10 shows the assembled device setup with the AC source attached. After the connections were completed, 35  $\mu$ l of the NGP solution was dropped on the 5 mm gap using a micro-pipette, in order to complete the connections between the electrodes for electric field application and to start the alignment process.

#### 4.5.3 Results

Figs. 4.10-4.18 show the alignment of GNPs for different electrodes, electric field intensities and frequencies. Figs. 4.10-4.12 show the alignment using silver electrodes device for an electric field intensity of 20kV/m, and 30kV/m, 40kV/m respectively for a time period of 60 minutes. Similarly Figs. 4.13-4.15 show the alignment using aluminum electrodes and Figs. 4.16-4.18

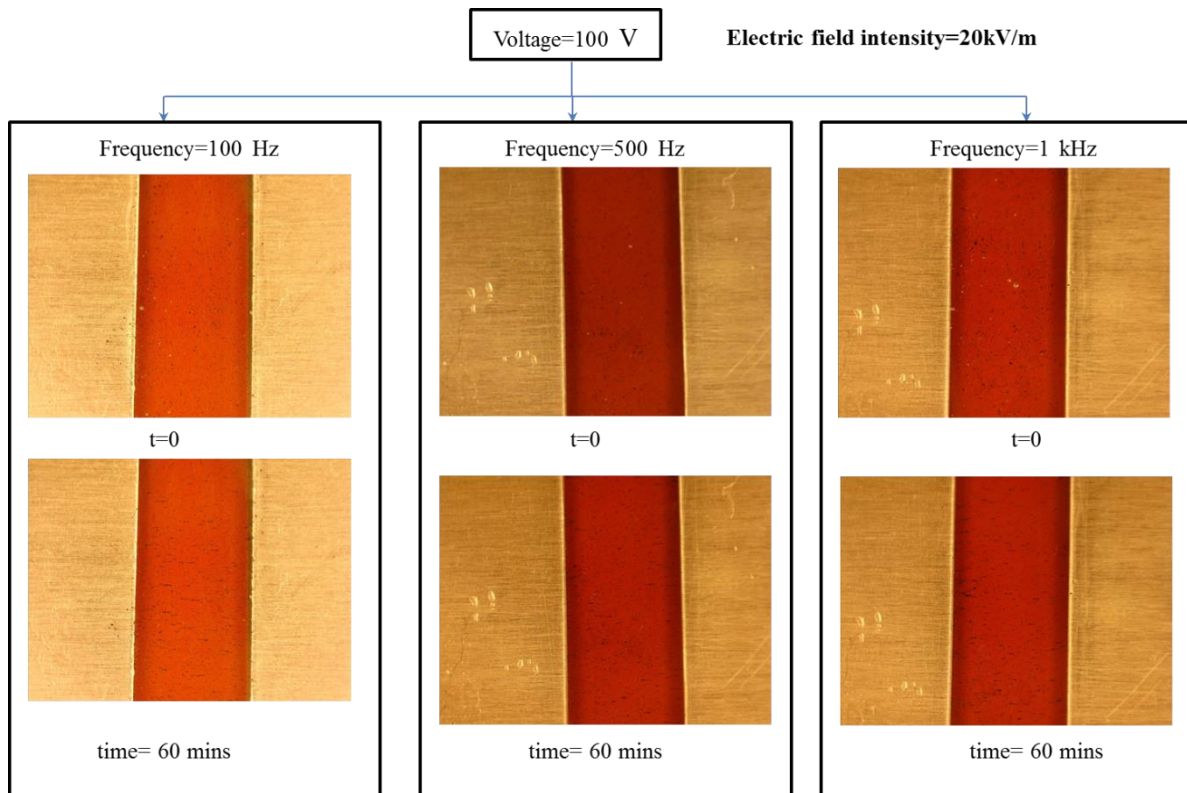


**Figure 4.10** Alignment using silver electrodes at 100V (100, 500, 1000 Hz) for 60 minutes depict the alignment using steel electrodes for the respective electric field intensities for a time period of 60 minutes. Each figure also shows variation in alignment with varying frequencies at constant field intensity.

It can be seen clearly from the above figures that with increasing electric field intensity from 20-40kV/m, there is an increase in the degree of alignment of the NGPs in the epoxy matrix. This is true for all three electrode systems. It should also be noted that NGP alignment is faster with higher electric field intensity. This can be demonstrated using Fig. 4.19 which compares alignment of NGPs using steel electrodes at 20kV/m, 30kV/m and 40kV/m for a 20 minute time period. It can be seen that for higher electric field intensity, the response of the NGPs to alignment is higher. Figs. 4.10-4.18 show the tendency of the NGPs to form aligned long column like structures traversing the two electrodes.

An interesting phenomenon occurs when aligning at 40kV/m at all electrode configurations and frequencies. Fig. 4.20 illustrates this feature. The alignment is generally faster at this field intensity, but as soon as the column connection of NGPs is complete, the column starts acting like an electrode in itself, generating an electric field in a direction perpendicular to the applied electric field, which causes already aligned neighboring NGPs to lose their alignment and form agglomerated clusters surrounding this channel. Fig. 4.20 shows a particular case of aluminum electrodes at 40kV/m and aligning at 100 Hz at different times. Figs. 4.12, 4.15 and 4.18 for the

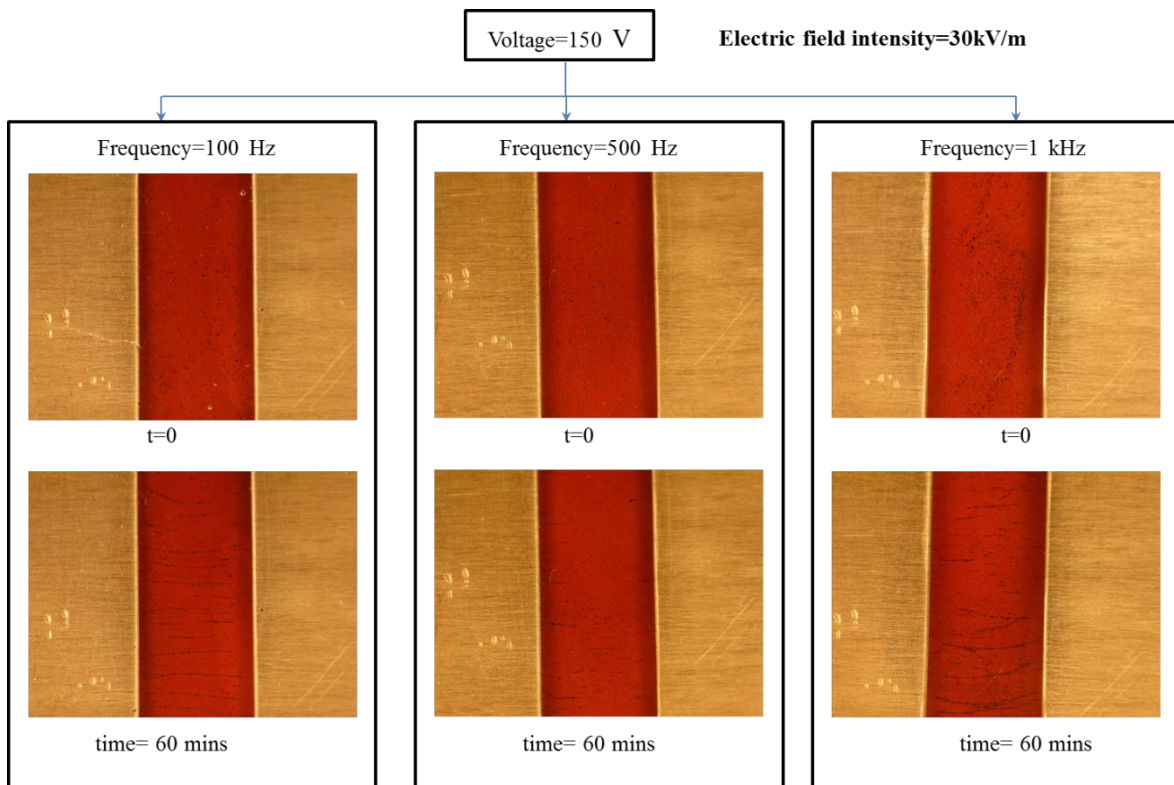


**Figure 4.11** Alignment using silver electrodes at 150V (100, 500, 1000 Hz) for 60 minutes

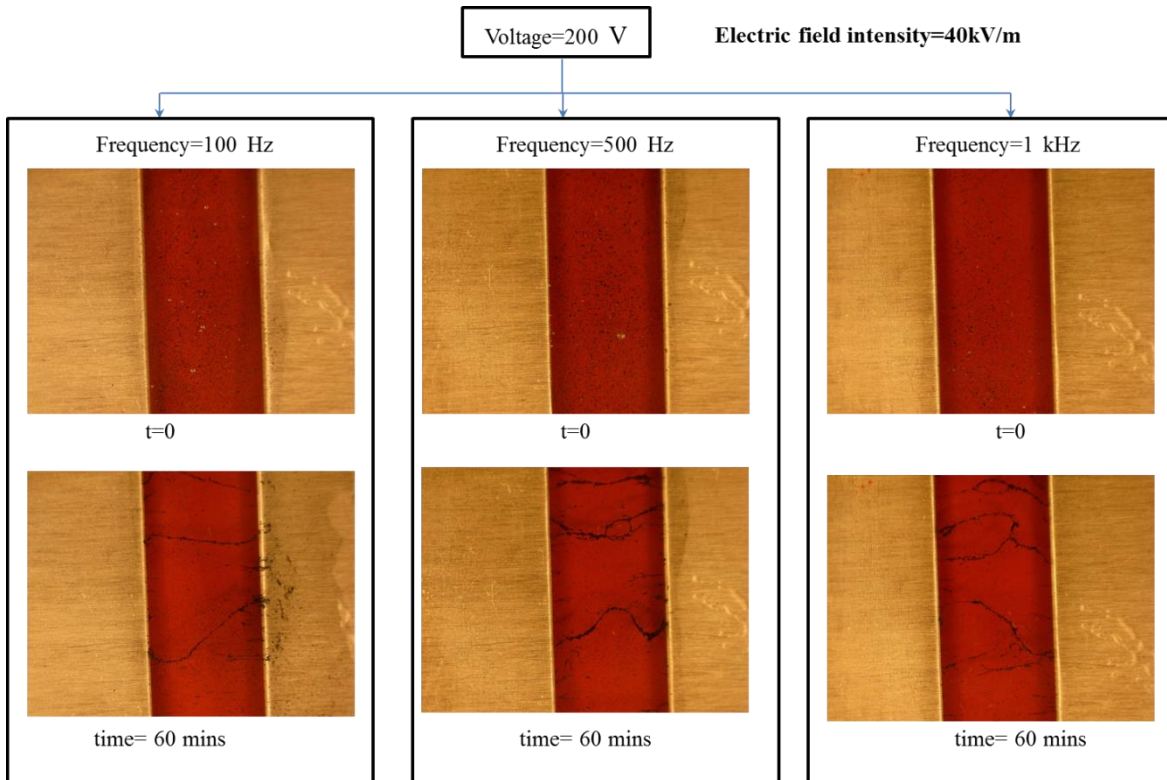


**Figure 4.12** Alignment using silver electrodes at 200V (100, 500, 1000 Hz) for 60 minutes

silver, aluminum and steel electrodes show this agglomeration which is a result of this interesting behavior. The reason for this behavior can be attributed to the inherently high conductivity of the NGPs in their alignment direction in conjunction to the already high field intensity applied.

The cases studied above can be compared in Figs. 4.21-4.29. Not much difference is seen in alignment after 60 minutes for each electrode set in individual cases, so any metallic conductor studied is an apt choice for an electrode system. However, the inherent choice for a good alignment lies with the field intensity. 30kV/m cases tend to behave well for all electrode systems and since there is limited agglomeration during aligning, would be a good choice for fracture property enhancement purposes. 40kV/m cases can be used too, if alignment is required in shorter time, but care needs to be taken to stop the alignment within 20 minutes, which is an

average time estimate before agglomeration of the NGPs begin, and cases like Fig. 4.12 are observed.

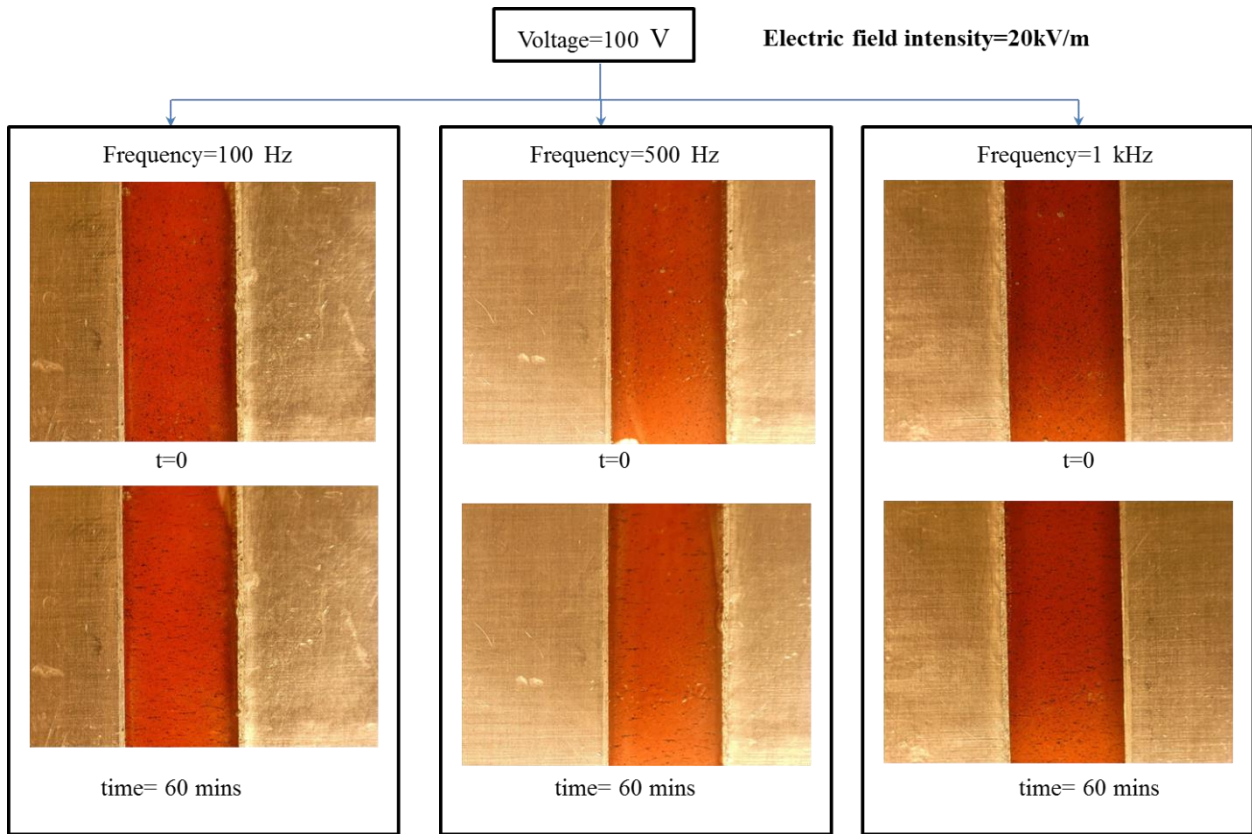


**Figure 4.13** Alignment using aluminum electrodes at 100V (100, 500, 1000 Hz) for 60 minutes. Frequency dependence in this particular study was low, although other authors have found better alignment at much higher frequencies. Unfortunately, due to constraint on the maximum frequency (1 kHz) that can be studied using the AC source employed, a definitive answer to the dependence on frequency cannot be provided. But for smaller sample fabrication purposes, the cases studied in this chapter should be perfectly adequate.

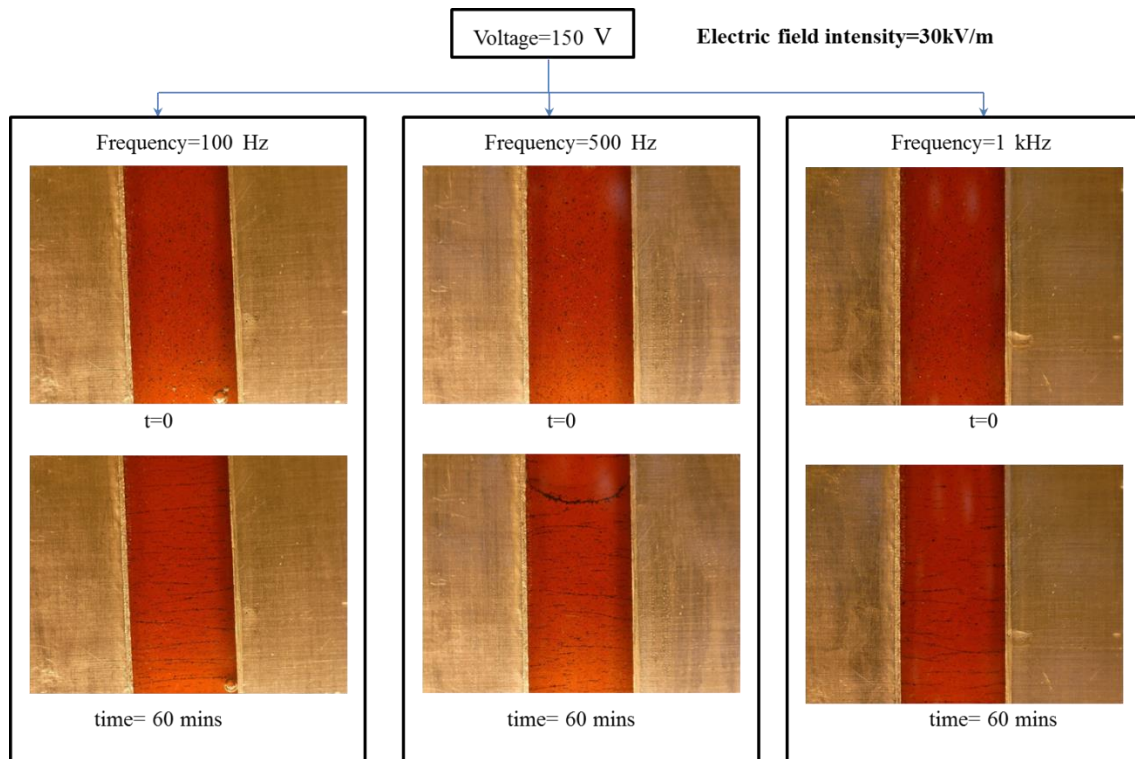


**Figure 4.14** Alignment using aluminum electrodes at 150V (100, 500, 1000 Hz) for 60 minutes

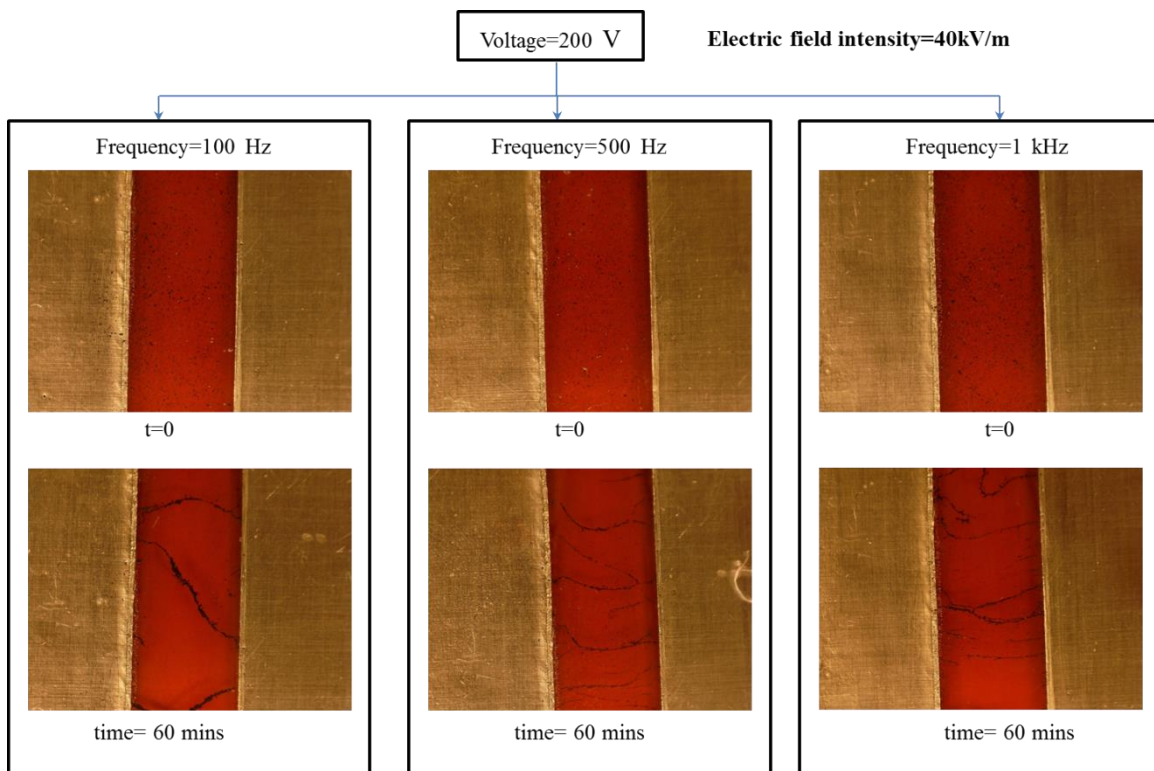


**Figure 4.15** Alignment using aluminum electrodes at 200V (100, 500, 1000 Hz) for 60 minutes

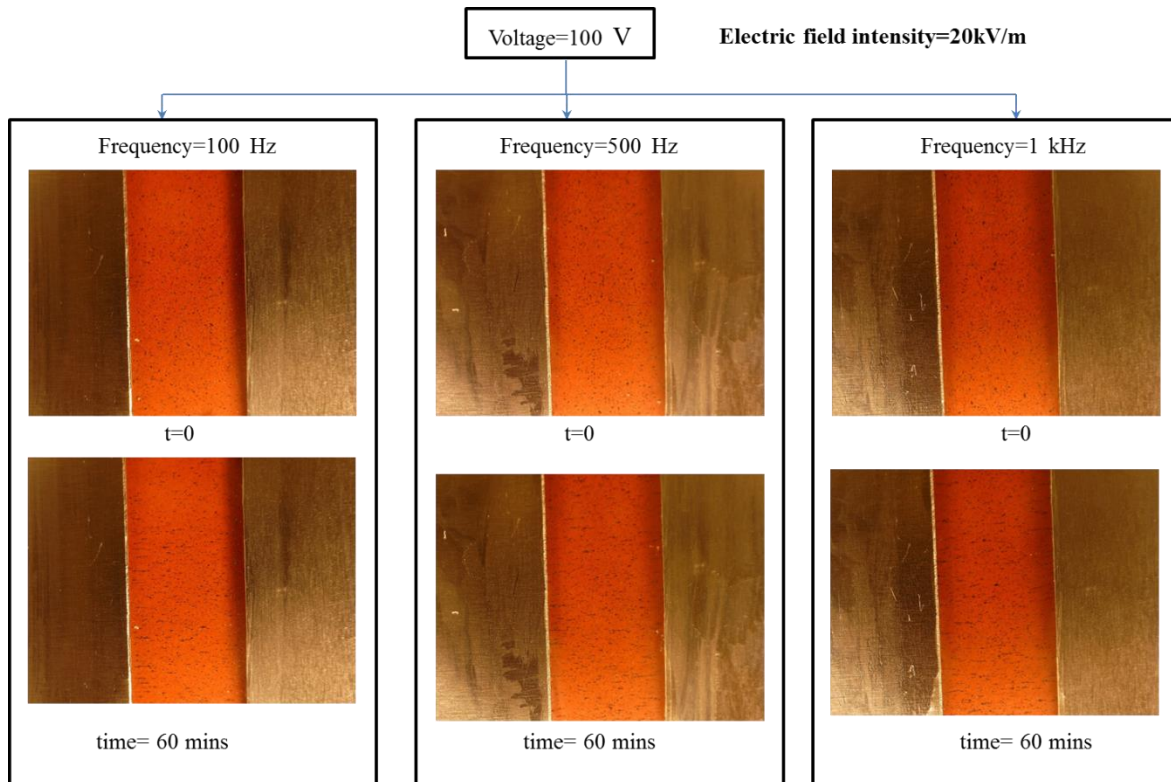


**Figure 4.16** Alignment using steel electrodes at 100V (100, 500, 1000 Hz) for 60 minutes

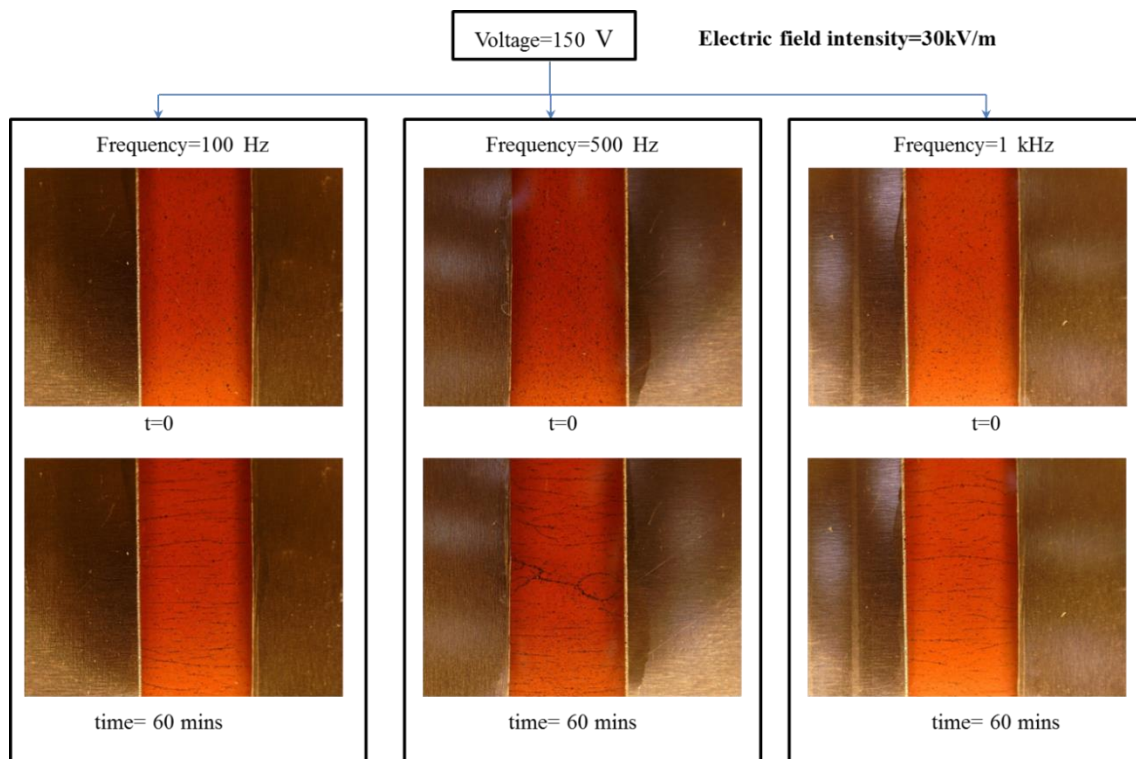


**Figure 4.17** Alignment using steel electrodes at 150V (100, 500, 1000 Hz) for 60 minutes

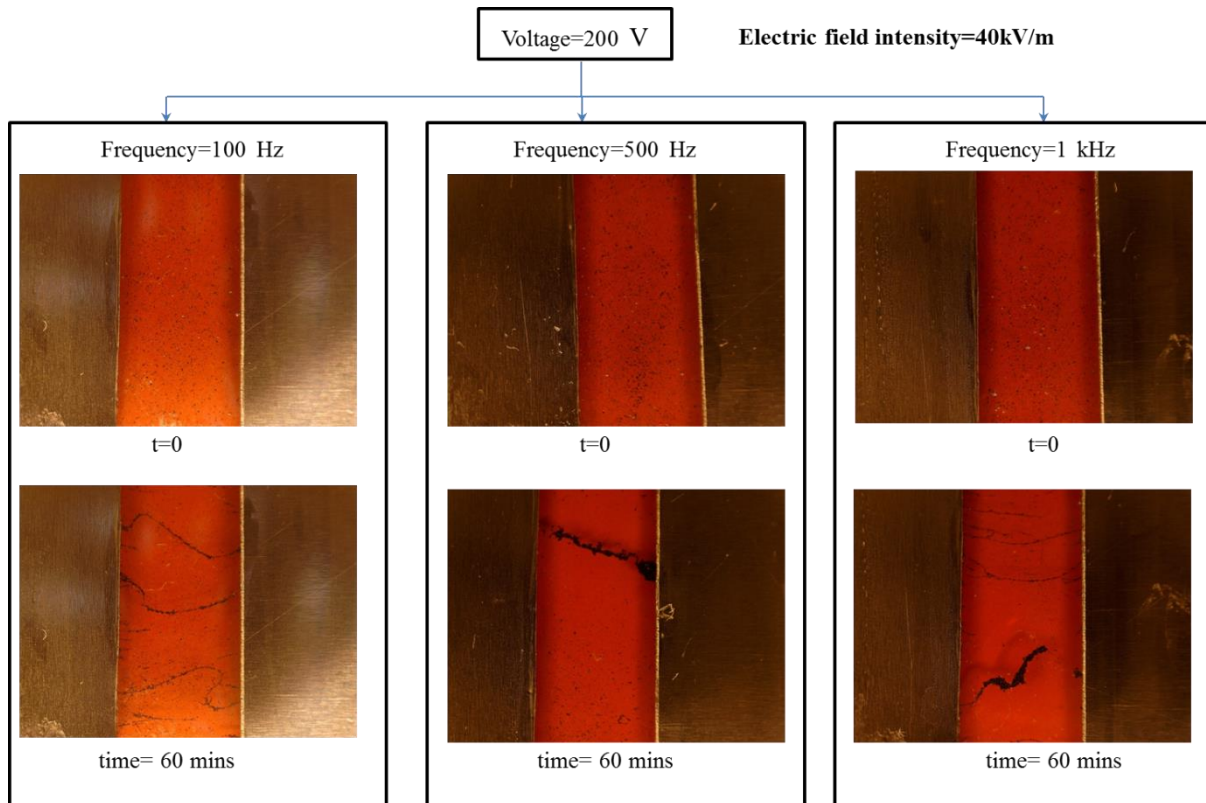


**Figure 4.18** Alignment using steel electrodes at 200V (100, 500, 1000 Hz) for 60 minutes

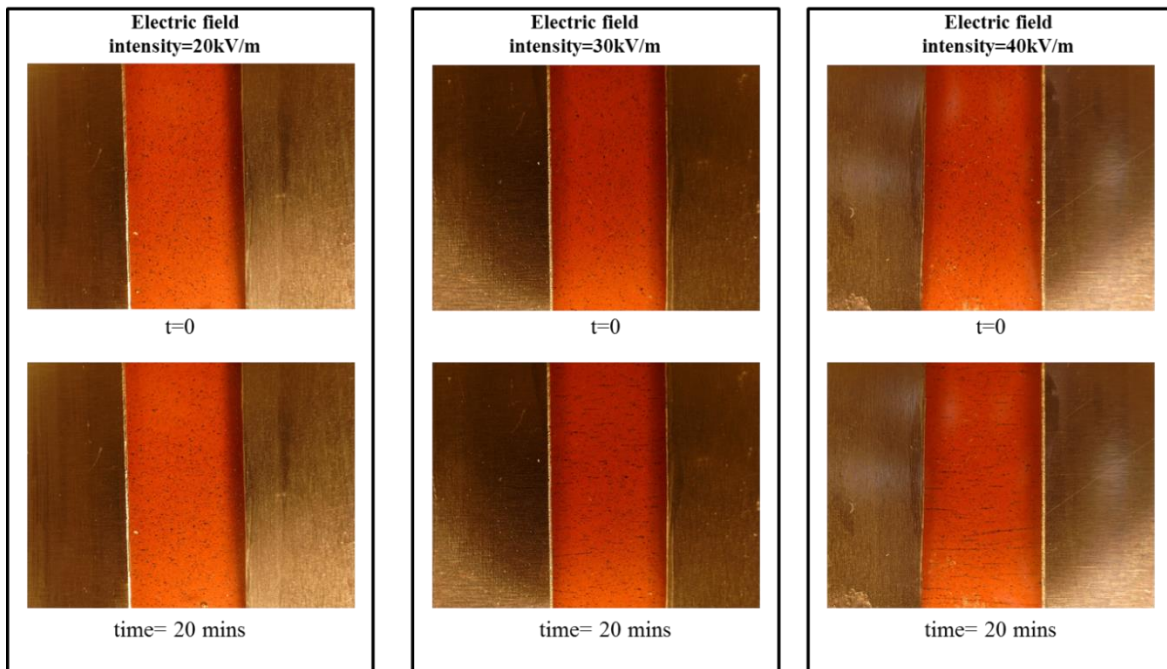


**Figure 4.19** Alignment using steel electrodes at 100V, 150V, 200V (100 Hz) in 20 minutes

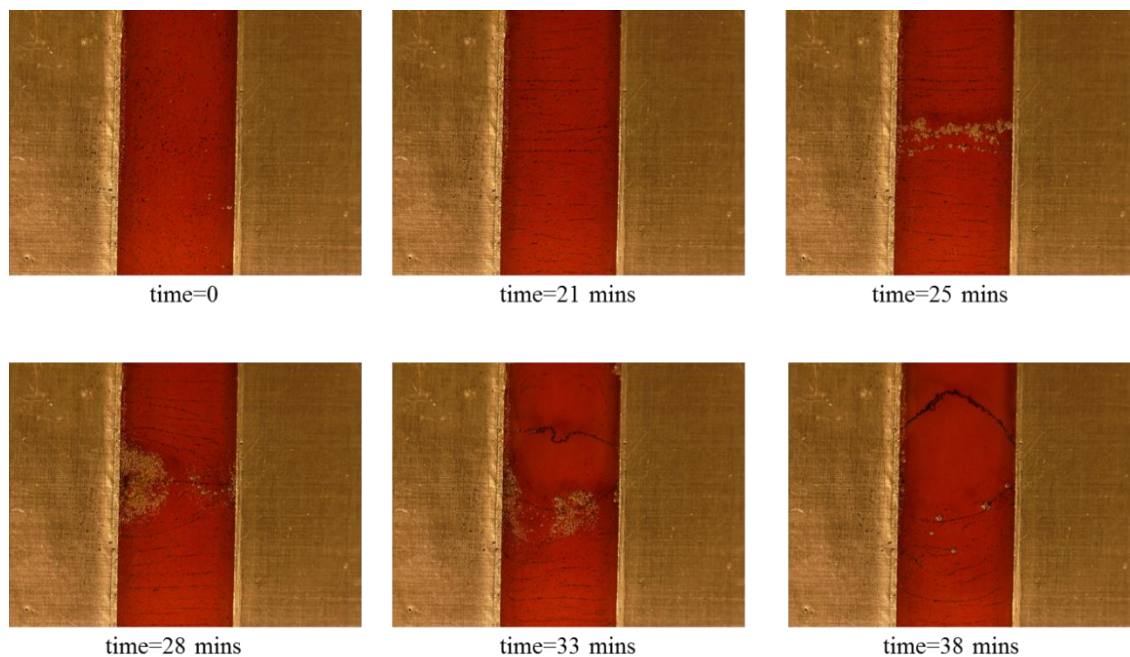


**Figure 4.20** Graphene column formation and agglomeration at 40kV/m for aluminum electrodes



**Figure 4.21** Comparison of alignment using different electrodes at 100V, 100 Hz for 60 minutes

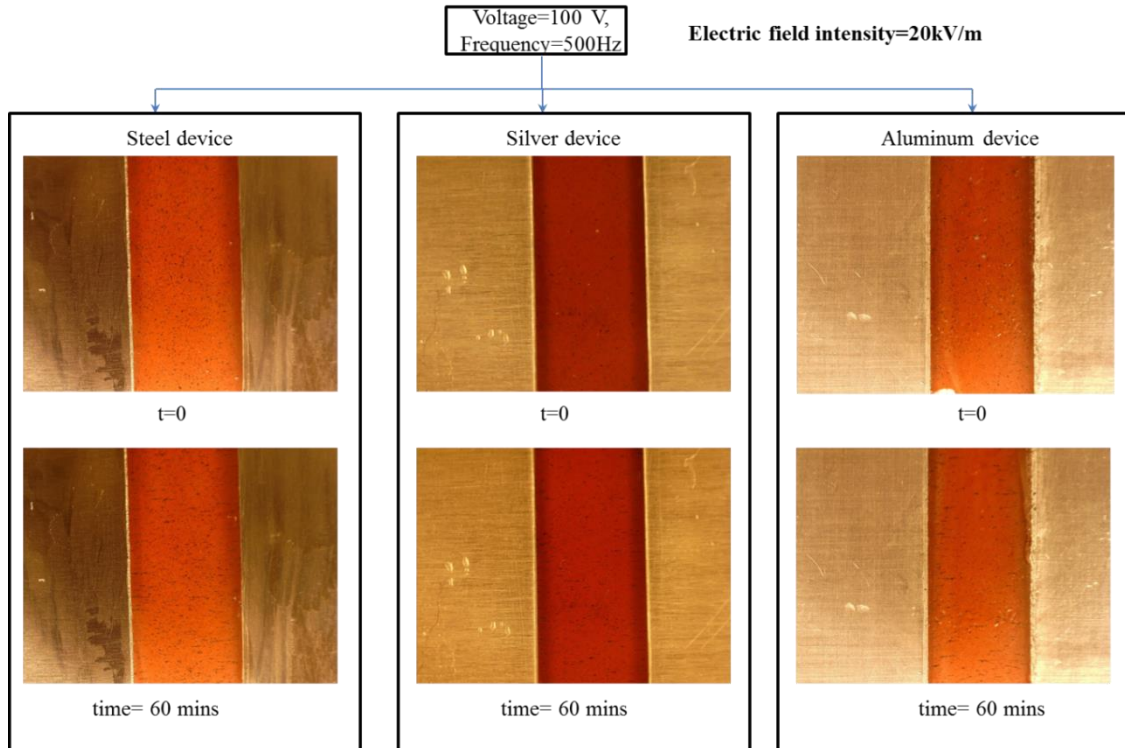


**Figure 4.22** Comparison of alignment using different electrodes at 100V, 500 Hz for 60 minutes

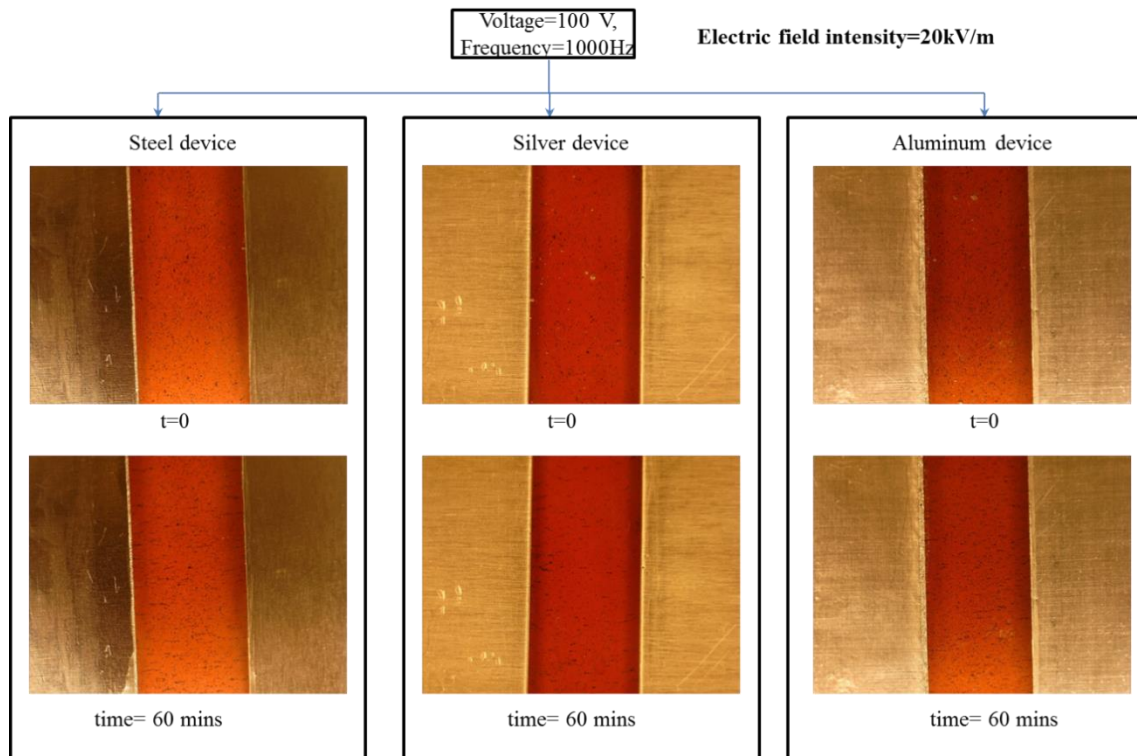


**Figure 4.23** Comparison of alignment using different electrodes at 100V, 1000 Hz in 60 minutes

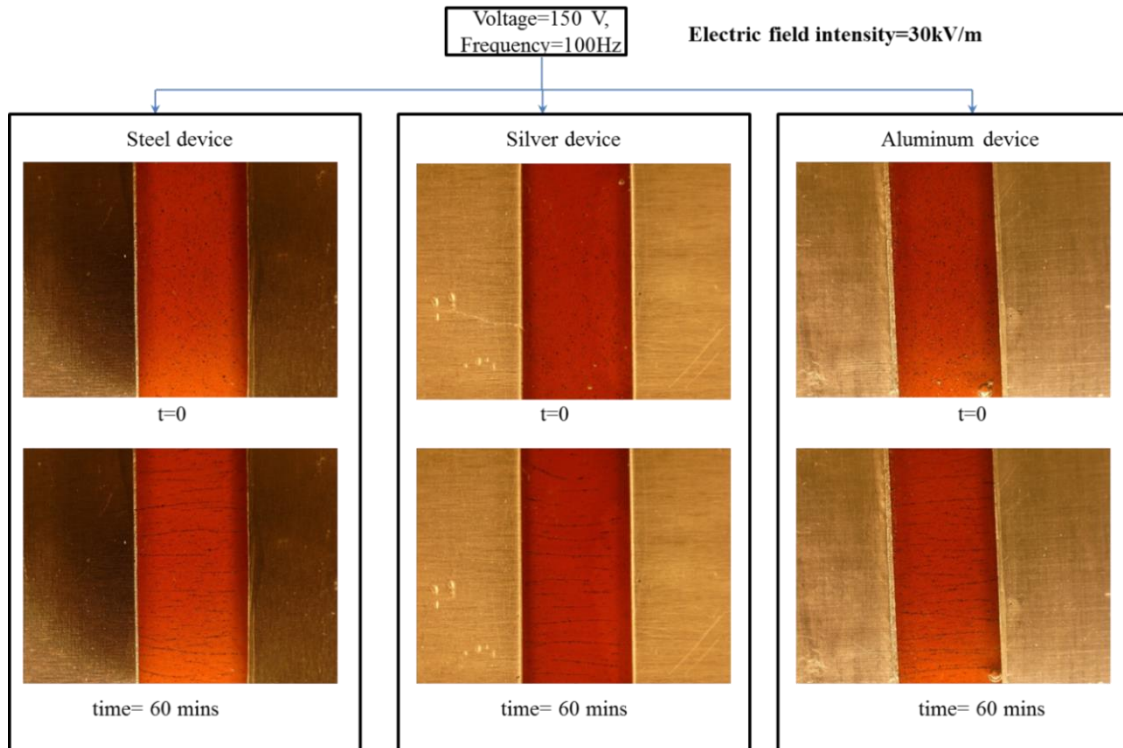


**Figure 4.24** Comparison of alignment using different electrodes at 150V, 100 Hz for 60 minutes

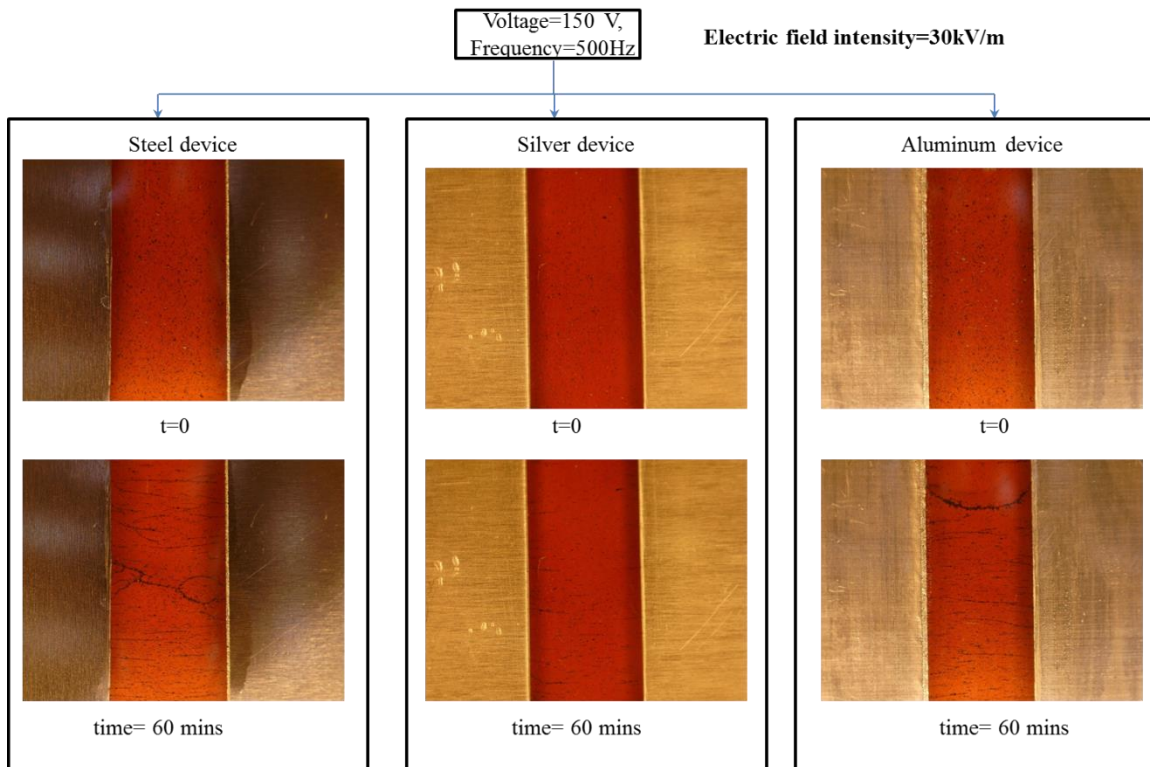


**Figure 4.25** Comparison of alignment using different electrodes at 150V, 500 Hz for 60 minutes

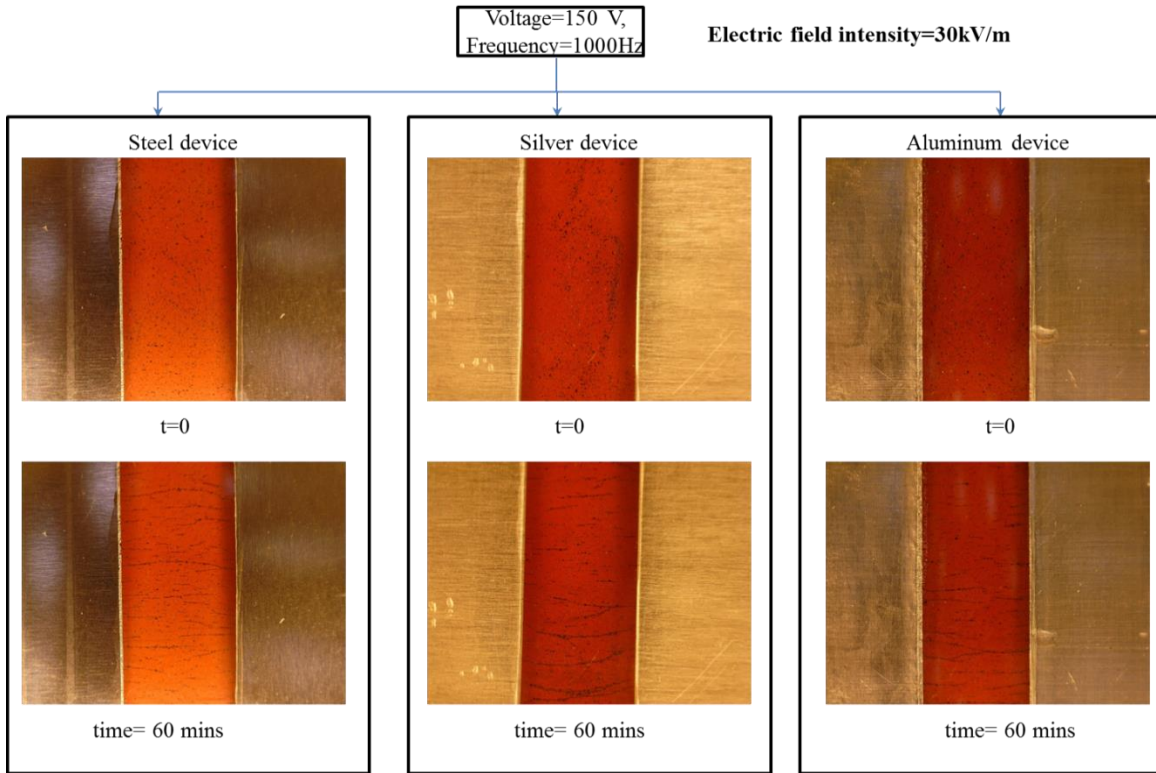


**Figure 4.26** Comparison of alignment using different electrodes at 150V, 1000 Hz in 60 minutes

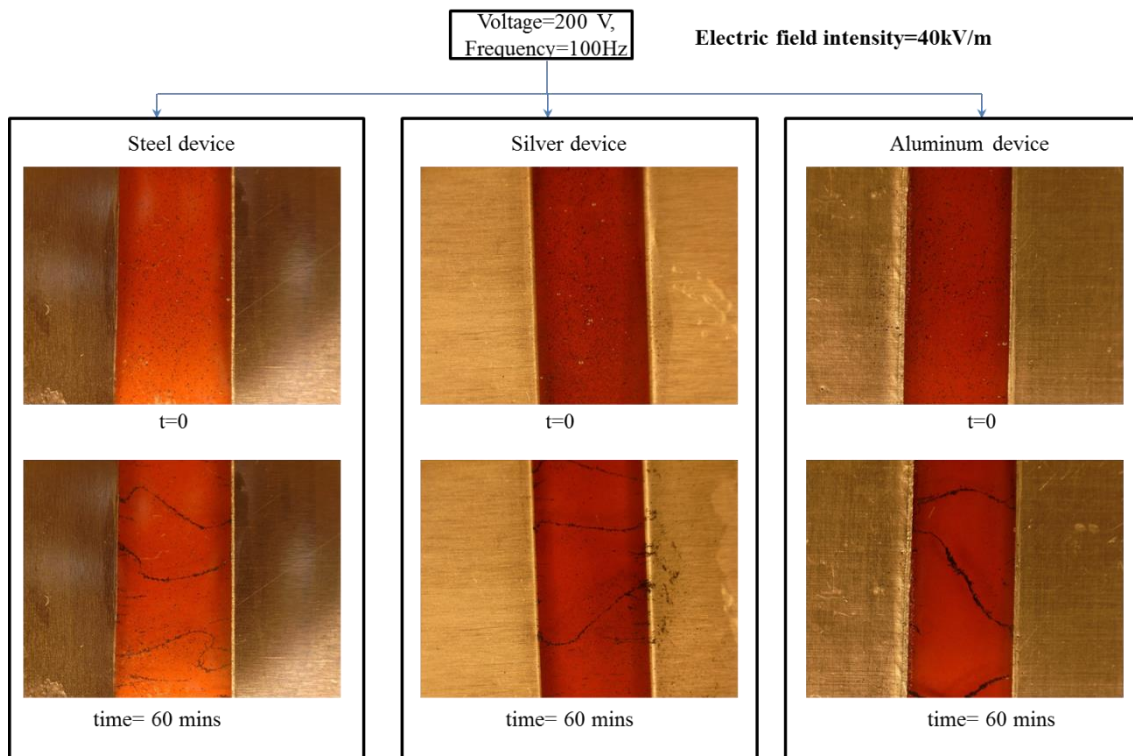


**Figure 4.27** Comparison of alignment using different electrodes at 200V, 100 Hz for 60 minutes

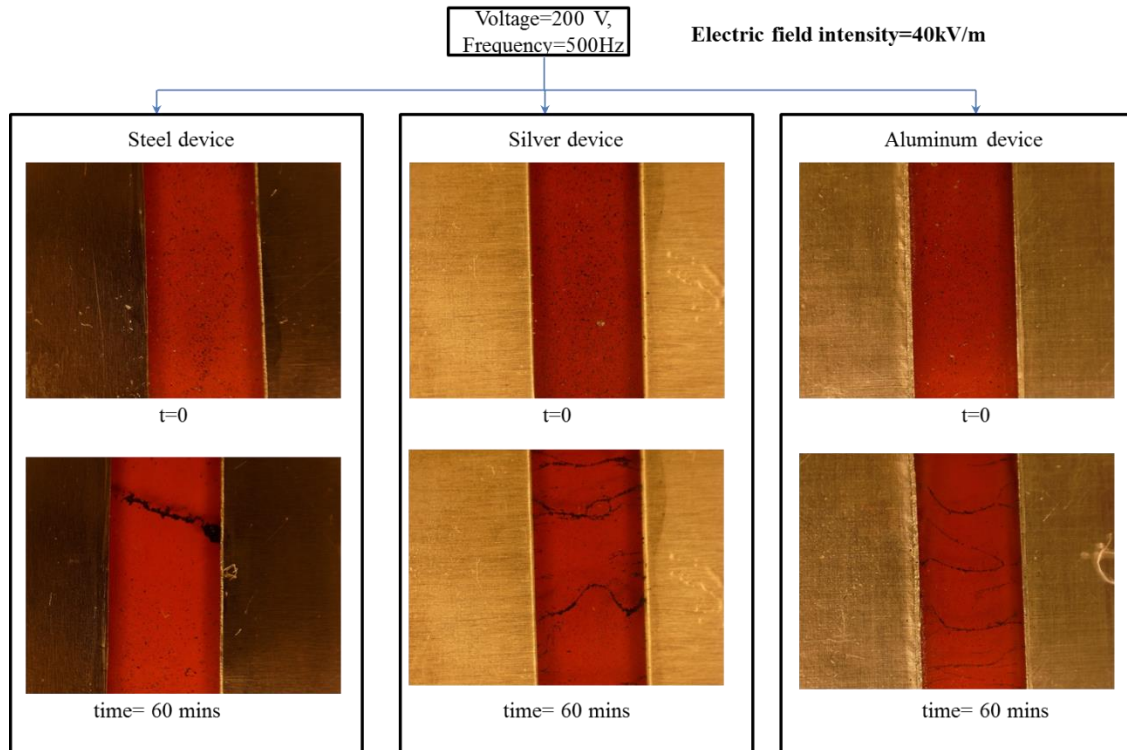


**Figure 4.28** Comparison of alignment using different electrodes at 200V, 500 Hz for 60 minutes

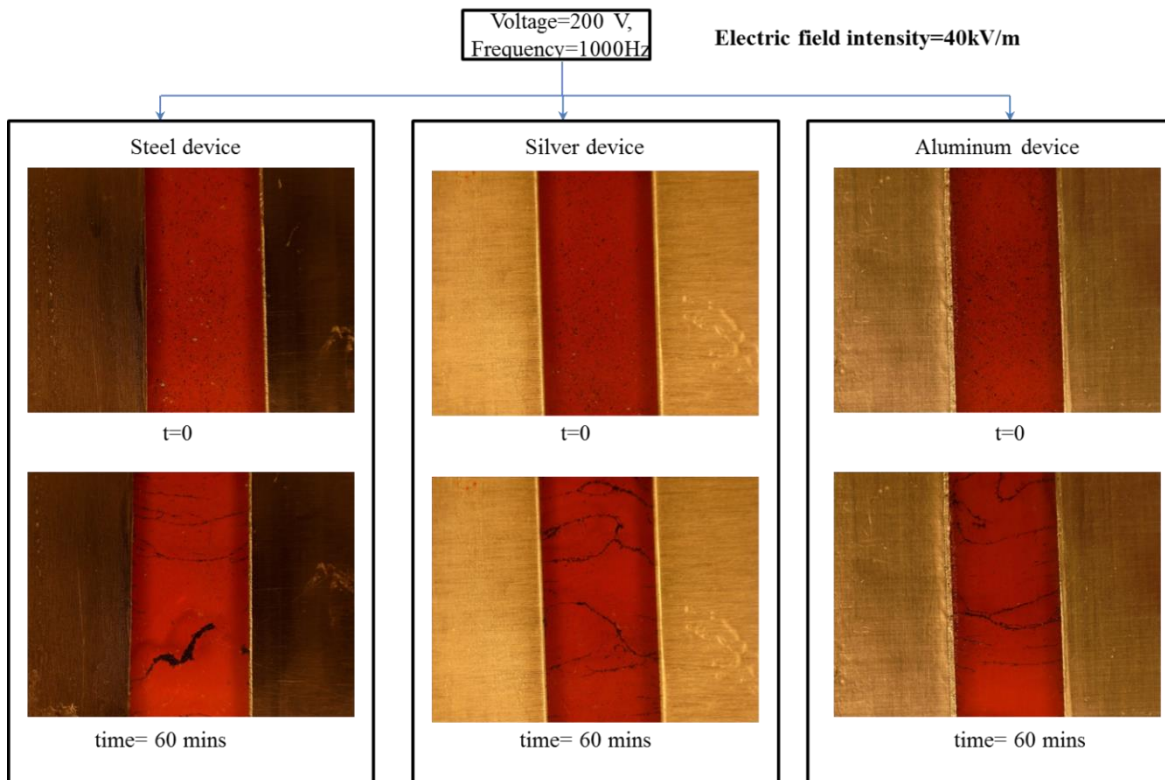


**Figure 4.29** Comparison of alignment using different electrodes at 200V, 1000 Hz in 60 minutes

## CHAPTER 5

### CHARACTERIZATION OF MIXED MODE FRACTURE PROPERTIES OF NGP REINFORCED EPOXY AND MODE I DELAMINATION PROPERTIES OF CARBON FIBER/NGP/EPOXY UNIDIRECTIONAL LAMINATE

#### 5.1 Summary

This chapter aims to experimentally investigate (a) the changes in mixed mode fracture properties of a thermoset polymer (EPON 862) reinforced with 23°C HP-NGPs (b) Mode I fracture properties of EPON 862/IM7 laminates with and without 23°C HP-NGPs. For (a), mixed mode experimentation was performed on baseline (0 wt%), 0.1 wt% and 0.5 wt% HP-NGP reinforced EPON 862 polymer using an asymmetric mixed mode specimen. Three different mode mix ( $K_{II}/K_I$ ) ratios (0.78, 1.53, 117) were used to obtain an experimental fracture envelop encompassing pure Mode I to Mode II. Remarkable increase in the fracture envelop both in Mode I (~3 times) and Mode II (~2.5 times) was observed with only 0.5 wt% of HP-NGP dispersed in the epoxy matrix.

For case (b), Double Cantilever Beam (DCB) experiments were performed to obtain the Mode I fracture toughness of the unidirectional laminate specimens with the NGP reinforced epoxy matrix, in accordance with ASTM D5528. Significant increase (~100%) in resistance to crack propagation was observed for the 0.5 wt% NGP reinforced system compared to baseline EPON system for a crack propagation length of 1 inch.

## 5.2 Experimental section

### 5.2.1 Materials

NGPs with an average diameter of  $15\ \mu\text{m}$  were procured from XG-Sciences Inc. The epoxy used in the study was EPON 862, which is di-glycidyl ether of bisphenol-F epoxy (DGEBF) from Momentive Inc. and the curing agent used was Curing agent 'W' (DETDA). Details of the starter materials can also be found in Chapter 3.

### 5.2.2 NGP hydrogen passivation and dispersion

The NGPs procured were hydrogen passivated at room temperature ( $23^\circ\text{C}$ ) for 6 hours using a 5%  $\text{H}_2/\text{N}_2$  mixture as explained in Chapter 4. Appropriate wt% of these HP-NGPs was weighed and dispersed in the epoxy using shear mixing at 2000 rpm for 1 hour after which the curing agent was added to the mixture. Details of the dispersion can be found in the Chapter 3.

### 5.2.3 Specimen preparation

#### 5.2.3.1 Mixed mode specimens

The mixture was degassed using a vacuum oven (Stable temp 282A) for 30 minutes at  $90^\circ\text{C}$  to remove any bubbles created during the mechanical stirring process. The hot mixture was poured into preheated silicone molds to limit production of bubbles during pouring. The silicon molds were then placed in an oven and subjected to a cure cycle as mentioned in Chapter 3. The molds were cooled to ambient temperature after the cure cycle was completed, and the specimens were ready for testing. ASTM D5045 was used to calculate the specimen dimensions [120]. Single edge notch specimens (3.5in x 0.8 in x 0.2 in, as shown in Fig. 5.1(a)) with  $(a/W) = 0.47$  including the pre-crack (introduced by tapping a sharp razor blade), were prepared for testing, where  $W$  is the width of the specimen and  $a$  is the initial crack length.

### 5.2.3.2 DCB testing specimens

Three separate 10in x 10in unidirectional  $[(0^\circ)_{24}]_s$  laminates were prepared using EPON 862 and HP-NGP (0 wt% (baseline), 0.1 wt% and 0.5 wt%) respectively. The three resin matrices were prepared using the NGP dispersion technique in Chapter 3. It should be noted that the wt% of the NGP is with respect to the weight of resin used in making the laminate, and therefore the actual wt% of the NGP will be much lower in the carbon fiber laminate. ASTM D5528 standard was followed during sample preparation to prepare the notched DCB specimen [132]. The starter notch (2.5 inch in length) was prepared by inserting a 12.5 $\mu$ m thick PTFE film (procured from Dupont Inc.) at the midplane of the laminate. Hand layup was used to assemble 24 unidirectional IM7 carbon fiber mats and the resin systems were prepared as described in Chapter 3. After initial impregnation of the fiber mats with resin using a brush, final consolidation was performed using a compression molding machine by using the curing cycle with varying pressure as below for proper consolidation of the laminate.

- (1) Preheat to 90°C.
- (2) 90°C -121°C in 30 minutes at 2000 psi.
- (3) 121°C for 2 hours at 3000 psi.
- (4) 121°C -177°C in 30 minutes at 4000 psi.
- (5) 177°C for 2 hours at 5000 psi.

The DCB specimens (7in x 0.9 in x 0.12 in) were cut using a diamond saw from the laminates and piano hinges were attached to the specimens as shown in Fig. 5.1(b).

## 5.2.4 Test setup and experimental data analysis

### 5.2.4.1 Mixed mode testing

Fig. 5.2 depicts the test setup for mixed mode fracture testing. An asymmetric 4 point bend test with variable loading axis distance ‘c’ was used to simulate different mode mix ratios as suggested by He et al [133]. Three different mode mix ratios ( $K_{II}/K_I$ ) were used 0.78, 1.53 and 117, corresponding to loading phase angles ( $\tan^{-1}(K_{II}/K_I)$ ) of  $38^\circ$ ,  $57^\circ$ , and  $89.5^\circ$  respectively. An MTS Qtest-25 testing frame with a 5000 lbs. load cell was used at a crosshead displacement rate of 0.05 in/min. to perform the test. The bending loads were applied using 4 roller pins supplied by MTS. Based on Fig. 5.2, the shear force Q acting at the crack front can be calculated using [133],

$$Q = P \frac{(b_2 - b_1)}{(b_2 + b_1)} \quad (5.1)$$

Where P is the force being applied at a particular time frame,  $b_1$  and  $b_2$  are the moment arms shown in Fig. 5.2. The mode I and mode II stress intensity factors can be calculated using [133],

$$K_I = \frac{6(c - c_o)Q}{W^2} \sqrt{\pi a} F_I(a/W)$$

$$K_{II} = \frac{\eta Q}{W^{1/2}} \frac{(a/W)^{3/2}}{(1 - a/W)^{1/2}} F_{II}(a/W) \quad (5.2)$$

Where  $F_I$  and  $F_{II}$  are calibration factors dependent on the specimen dimensions [133],

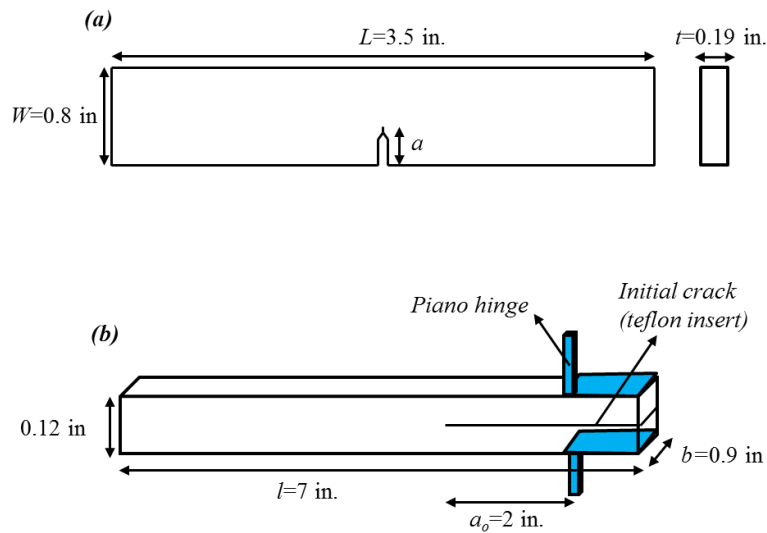
$$F_I(a/W) = \sqrt{\frac{2W}{\pi a} \tan \frac{\pi a}{2W}} \frac{0.923 + 0.199 \left(1 - \sin \frac{\pi a}{2W}\right)^4}{\cos \frac{\pi a}{2W}} \quad \text{for } 0 \leq \frac{a}{W} \leq 1 \quad (5.3)$$

$$F_{II}(a/W) = 7.264 - 9.37 \left(\frac{a}{W}\right) + 2.74 \left(\frac{a}{W}\right)^2 + 1.87 \left(\frac{a}{W}\right)^3 - 1.04 \left(\frac{a}{W}\right)^4 \quad \text{for } 0 \leq \frac{a}{W} \leq 1$$

The parameters  $c_o$  and  $\eta$  are introduced to account for the proximity of the loading points to the crack. Ref. 122 was used to calibrate these values for different  $c/W$  ratios. A constant value of  $c_o/W = -.0036$  was calculated for each mode mix ratio. Table 5.1 shows the values of  $\eta$  used for each mode mix ratio.

#### 5.2.4.2 DCB testing

Standard DCB tests were performed using a MTS QTest-25 universal testing machine at room temperature ( $\sim 23^\circ\text{C}$ ) and quasi-static conditions using displacement control (0.05 in/min) to obtain Mode-I fracture toughness and resistance curves of the laminates. The test setup is



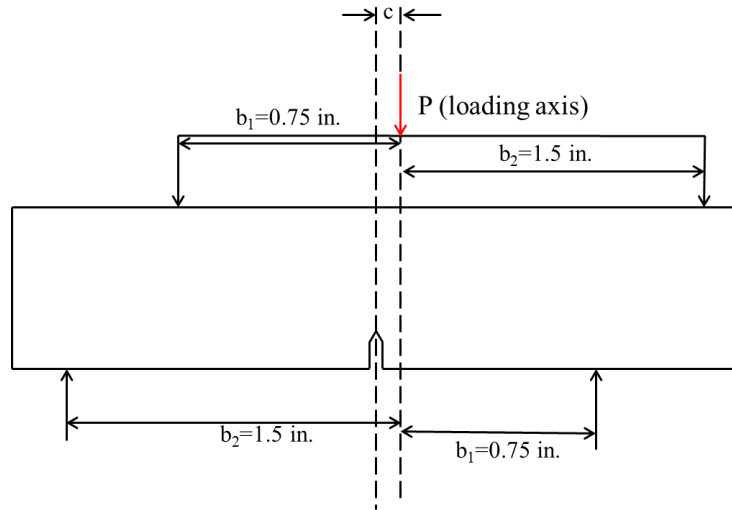


**Figure 5.2** Mixed mode test setup

illustrated in Fig. 5.3. A Mark-5D high resolution camera with a 100 mm macro lens was used to capture the crack propagation with time. Load and displacement readings were recorded at regular intervals until the crack propagated one inch. The video from the camera was post-processed to get individual frames using Photoshop CC which aided in the calculation of crack length at individual time frames and were correlated to the load displacement data to plot the



**Figure 5.3** DCB test setup

resistance curves (R-curve) for each specimen type. The energy release rate  $G_I$  can be calculated using ASTM D5528 [132],

$$G_I = \frac{3P\delta}{2b(a + |\Delta|)} \quad (5.4)$$

Where  $P$  is the load,  $\delta$  is the displacement,  $b$  is the specimen width and  $a$  is the delamination length and  $\Delta$  is the compliance correction calculated as the x-intercept of  $(\delta/P)^{1/3}$  vs  $a$  plot.

## 5.3 Results and Discussion

### 5.3.1 Mixed mode test results

Five specimens were tested for each mode mix ratio. Fig. 5.4 depicts load-displacement plots comparison for different specimens for each mode mix ratio. The plots clearly depict the increase in load carrying capability of the HP-NGP reinforced specimens at only 0.5 wt% at each mode mix ratio. Table 5.2 and 5.3 present pure Mode II ( $89.5^\circ$ ) and mixed mode,  $K_{Ic}$  and  $K_{IIc}$  values for each case respectively. Table 5.2 shows an increase of 158% in Mode II fracture toughness when compared with baseline. For only 0.1 wt% and 0.5 wt% of HP-NGP addition, an increase of 104% and 158% was observed respectively. Similar increases in toughness are observed for the mode mix angles of  $\psi = 57^\circ$  and  $\psi = 38^\circ$  as listed in Table 5.3.

In Chapter 3, Mode I testing was performed on CT specimens which gave ~200% increase in pure mode I fracture toughness ( $K_{Ic}$ ) for only 0.5 wt% of NGP in epoxy. Although the increase in mixed mode toughness with the addition of NGP is not nearly as much as in the case on Pure Mode I, it is still very significant. Further, the increased deformation at failure (ductility) due to the addition of NGP is very much evident in the mixed mode cases as can be seen in Fig. 5.4, and is consistent with the increased deformation at failure observed for pure Mode I fracture (Fig. 3.6). For an overall comparison, a normalized fracture envelop was plotted as shown in Fig. 5.5, indicating a steady increase in the resin fracture toughness with increasing wt% of NGP over

baseline data while encompassing a full range of mode mix ratios. The key issue of increased ductility of a brittle epoxy resin with the addition of NGP, and the nanoscale mechanisms behind this increase, will be addressed in Chapter 6.

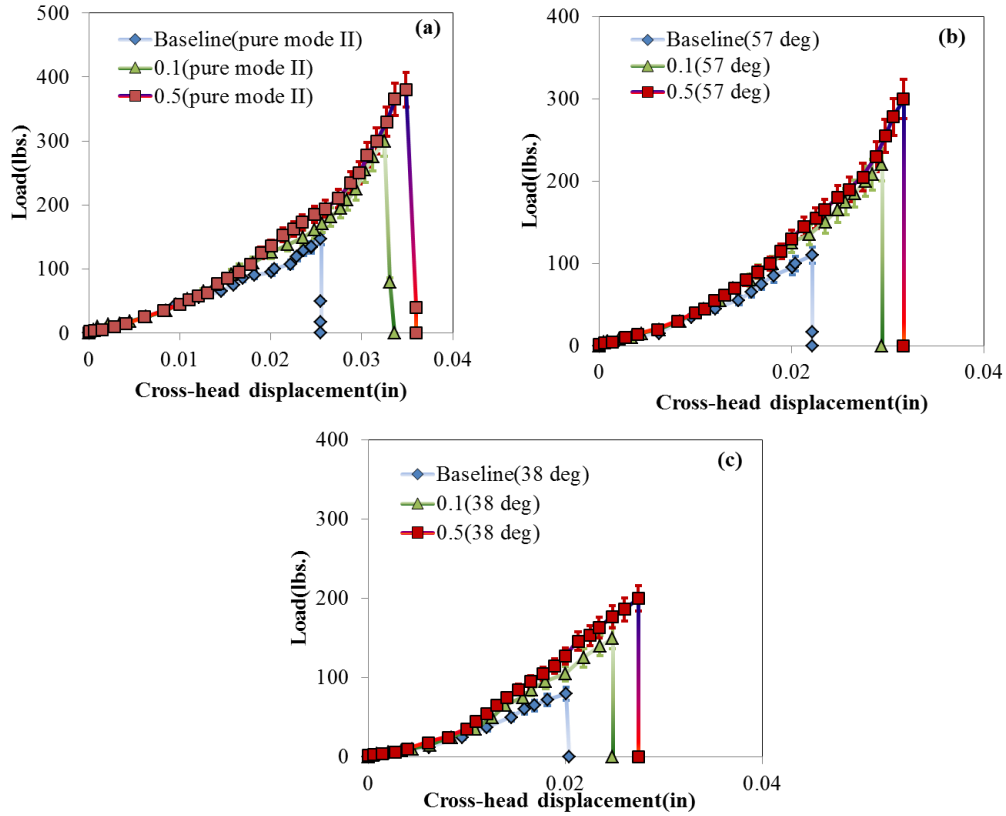


**Figure 5.4** Load displacement plots of mixed mode results for mode mix angle (a)  $\psi = 89.5^\circ$  (Mode II), (b)  $\psi = 57^\circ$ , and (c)  $\psi = 38^\circ$

**Table 5.1** Calibration parameters used for mixed mode data analysis

Case	$\eta$
Mode II ( $\psi = 89.5^\circ$ )	0.998
$\psi = 57^\circ$	1.0098
$\psi = 38^\circ$	1.0267

**Table 5.2** Pure mode II critical stress intensity factors

Specimen	Average $K_{IIc}$ (MPa.m <sup>1/2</sup> )	
	$(\Psi=89.5^\circ)$	
		% improvement
Baseline	0.49±0.015	-
0.1 wt%	0.99±0.02	104%
0.5 wt%	1.25±0.027	158%

**Table 5.3** Mix mode critical stress intensity factors for  $\Psi=57^\circ$  and  $\Psi=38^\circ$  mixed mode cases

Specimen	Mode Mix SIF (MPa.m <sup>1/2</sup> )			
	Mode mix ratio=0.78, $\Psi=57^\circ$		Mode mix ratio=1.53, $\Psi=38^\circ$	
	$K_{Ic}$	$K_{IIc}$	$K_{Ic}$	$K_{IIc}$
Baseline	0.24±0.02	0.37±0.02	0.34±0.02	0.27±0.02
0.1 wt%	0.48±0.02	0.73±0.02	0.64±0.02	0.51±0.02
0.5 wt%	0.65±0.02	1.0±0.02	0.86±0.02	0.68±0.02

### 5.3.2 DCB test results

Four replicate specimens were tested for each NGP wt% in the epoxy matrix. Fig. 5.6 depicts an averaged load-displacement plot for each case and clearly shows that the presence of HP-NGPs in the epoxy matrix improves the peak load at delamination initiation of the composite laminates. Using the data from the camera for tracking crack propagation (Fig. 5.7) over a distance of 1 inch, a delamination growth resistance curve (R-curve) was plotted for each NGP loading as

shown in Fig. 5.8. This chart shows that both the initiation fracture toughness (when the delamination crack is 2 inch in length), and the propagation fracture toughness

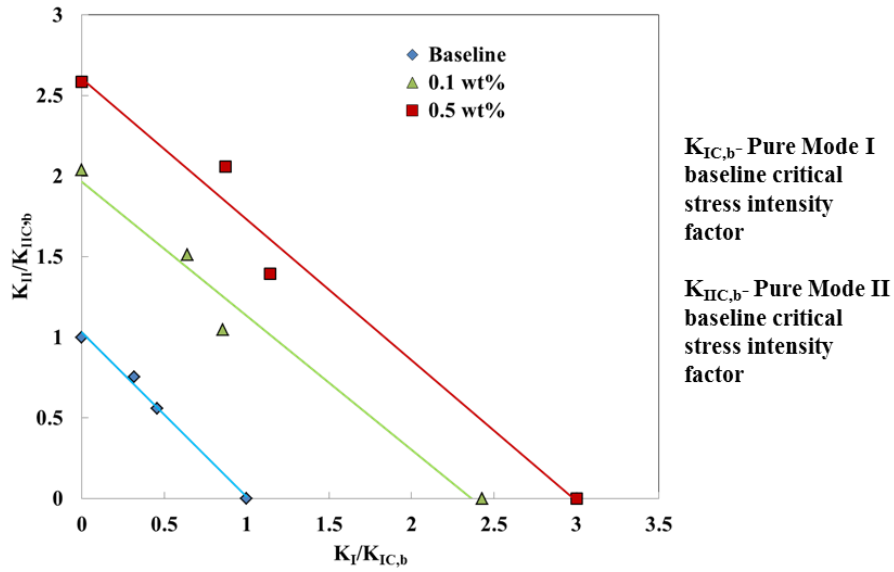


**Figure 5.5** Normalized mixed mode fracture envelop

(when the delamination crack reaches 3 inch in length) are much higher for the HP-NGP reinforced laminates in comparison to the baseline specimens. Tables 5.4 and 5.5 compare the initiation and propagation fracture toughness for each specimen type. An increase in initiation toughness of 29% and 48% is observed for 0.1wt% and 0.5wt% NGP cases, respectively, while an increase in crack growth resistance of 61% and 68% is observed after the delamination has grown by 1-inch for 0.1wt% and 0.5wt% NGP cases, respectively. The nanoscale mechanisms behind the increase in delamination initiation toughness with the addition of NGP, as well as the increase in delamination resistance with crack growth will be addressed in Chapter 6.

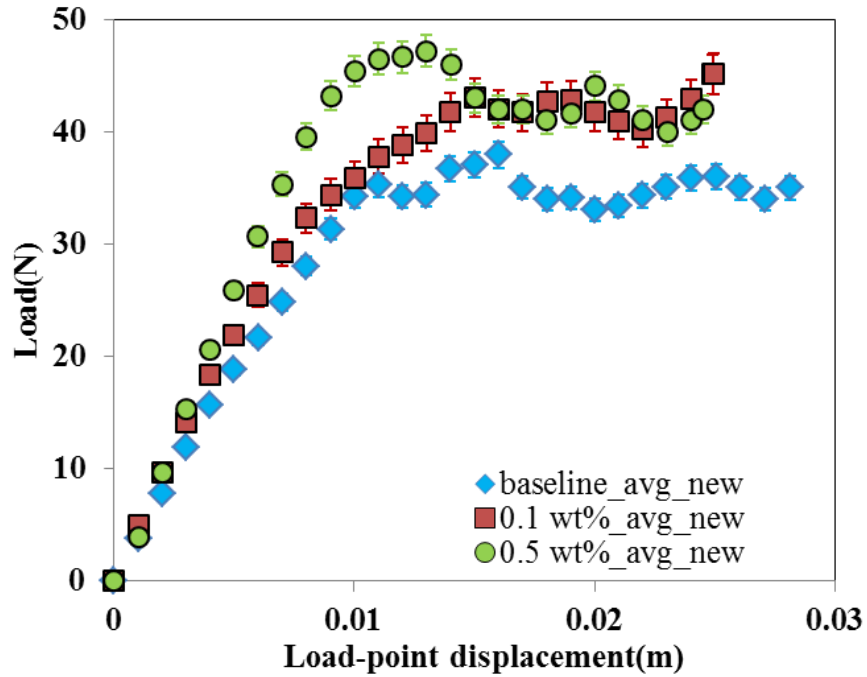


**Figure 5.6** Load displacement plot comparison for baseline, 0.1 wt% and 0.5 wt% HP-NGP reinforced epoxy laminates (DCB specimens)

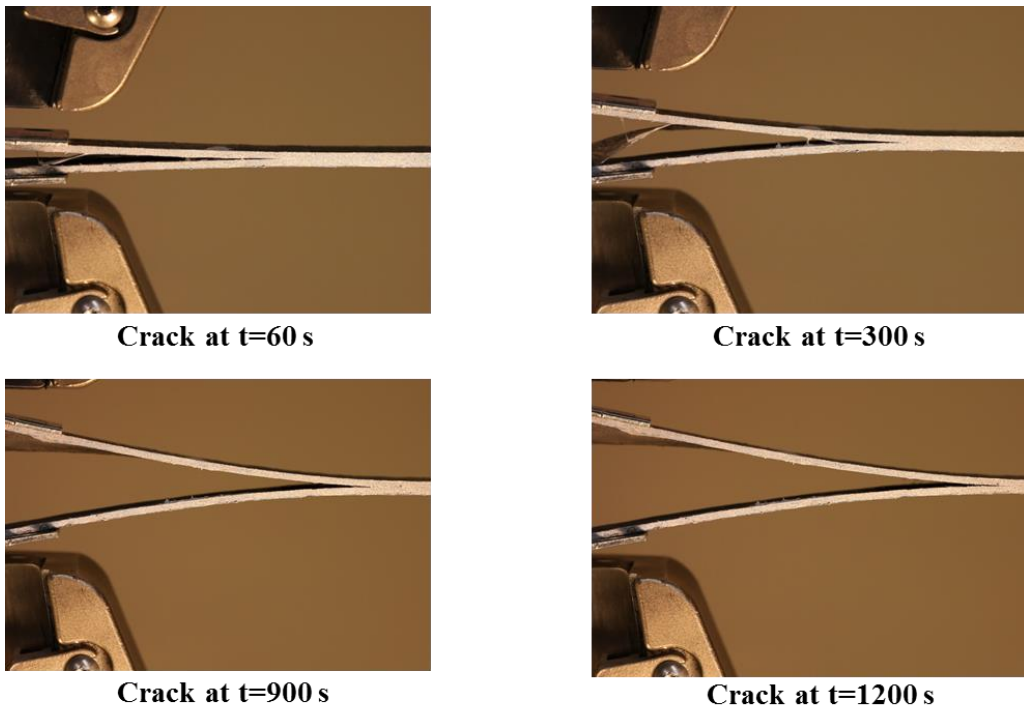


**Figure 5.7** Crack propagation captured using camera for post processing in DCB testing

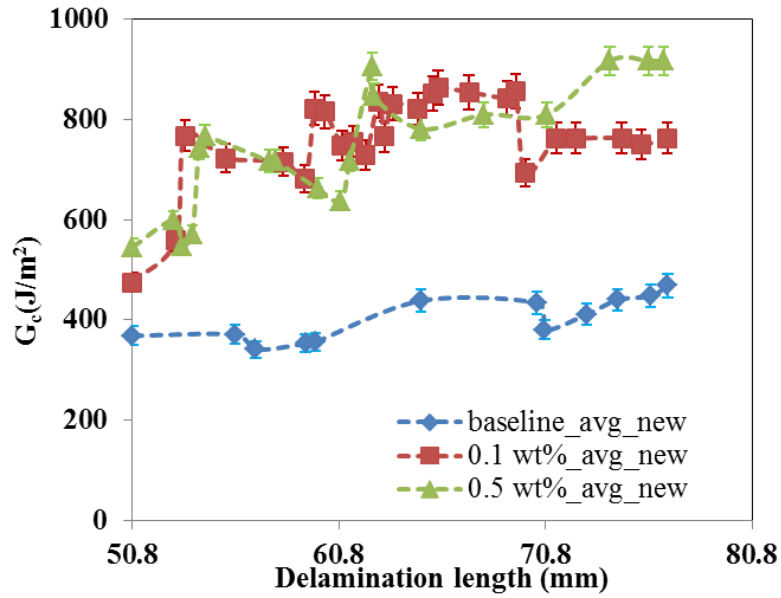


Figure 5.8 R curves for baseline and NGP reinforced epoxy laminates from DCB testing

Table 5.4 Initiation fracture toughness of laminates at 2 inch crack length

Specimen type	$G_{IC}^2$ (J/m <sup>2</sup> )	% improvement
Baseline CFRP	368.9±11.1	-
0.1 wt% graphene CFRP	475.3±19.2	29%
0.5 wt% graphene CFRP	545.7±16.4	48%

Table 5.5 Propagation Fracture toughness of laminates after 1 inch crack propagation

Specimen type	$G_c^2$ (J/m <sup>2</sup> )	% resistance increase
Baseline CFRP	458.2±18.3	-
0.1 wt% graphene CFRP	756.5±22.9	65%
0.5 wt% graphene CFRP	917.2±27	100%

## CHAPTER 6

### MECHANISMS FOR TOUGHNESS ENHANCEMENT IN POLYMERS AND COMPOSITES AT THE NANO SCALE

#### **6.1 Summary**

It is now well known that the use of polymers as matrix materials in composites demands excellent mechanical performance over a wide range of temperatures and multi-axial loads. A limiting factor in the use of polymer matrices, however, is their relative brittleness and tendency to exhibit micro-cracking at low levels of strain. These micro-cracks may coalesce under load, forming intra-ply macro cracks or inter-ply delamination, and ultimately result in catastrophic structural failure. While design strains can be kept to lower levels to prevent macro-cracking and catastrophic failure, additional composite material is required to bear the applied load, increasing the total weight of the composite structures. To mitigate the brittleness and micro-cracking of polymer matrices without incurring weight penalty, researchers have experimented with the addition and dispersion of a small weight percentages of nano particles in polymer matrices to improve their strain to failure and fracture toughness, as described in the earlier chapters of this dissertation. Although some researchers have postulated crack deflection and nanoparticle pull-out as primary toughening mechanisms [95, 96, 98], the exact toughening mechanisms at the nanoscale have remained elusive.

Postulating the existence of stress singularity at a crack tip in a continuum (such as, a polymer matrix), linear elastic fracture mechanics (LEFM) proposes a material property termed fracture toughness (i.e., the critical stress intensity factor  $K_{Ic}$  or energy release rate  $G_{Ic}$ ) to determine

whether a brittle solid loses its load-carrying capability due to crack initiation and propagation. If there is a central crack in an infinite plate subjected to remote uniform tension, the critical remote stress  $\sigma_{cr}$  as a function of crack length,  $2a$ , can be estimated by [134],

$$\sigma_{cr, \text{far-field}} = \frac{K_{IC}}{\sqrt{\pi a}} = \sqrt{\frac{2E^* \gamma}{\pi a}} \quad (6.1)$$

where  $E^*$  = material constant dependent on plane-strain or plane-stress condition; and  $\gamma$  is surface energy, i.e.,  $G_{Ic} = 2\gamma$  in the absence of dissipative losses. According to Eq. (6.1), on the basis of fracture toughness as a material constant, once the crack length,  $2a$ , approaches nanoscale, the far-field critical stress  $\sigma_{cr}$  could exceed the theoretic strength  $\sigma_{th}$  of a perfect solid. Because this is not physically admissible, the critical crack length  $a_{cr}$  can be calculated as,

$$a_{cr} = \frac{K_{IC}^2}{\pi \sigma_{th}^2} \quad (6.2)$$

which is the crack length below which the strength of nanoscale structures is governed by the theoretical strength and not by fracture toughness, thereby triggering a brittle to ductile transition in the failure mode as schematically depicted in Fig. 6.1. Guided by the large increase in ductility of the CT specimens at fracture due to the presence of NGP as described in Chapters 3 and 5, it is hereby postulated that the primary toughening effect observed with the dispersion of small amounts of nanographene (NGP) in a polymer and polymer composite is because of the nanoscale crack that is created when a macro-scale crack impinges on a nanoparticle-polymer interface and is deflected along the polymer-nanoparticle interface. By limiting the length of the dispersed NGP to be less than the critical crack length ( $a_{cr}$ ) for a given polymer matrix through high-shear processing, very significant increases in Mode I and mixed-mode toughness can be achieved, as evidenced in the fracture test data in Chapters 3 and 5. The transition of failure

mode from LEFM fracture (brittle) to strength-based diffuse-damage (ductile), results in far greater energy absorption, and hence greater “toughness” enhancement as reported in the literature by our group and others [31, 95]. Hence, in general, for optimum toughening of any matrix using nanoparticles, the overall length of the nanoparticle ( $l_{cr}$ ) must be less than  $a_{cr}$  determined by inputting the value of the Mode I fracture toughness and the theoretical strength of the matrix material in Eqn. (6.2).

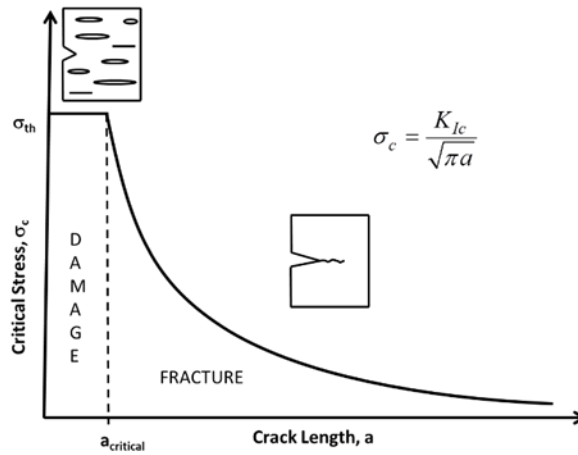


**Figure 6.1** Crack length effect at the nanoscale

The rest of this chapter focuses on extending the above fundamental concept to planar mixed-mode fracture (Mode I and II) and deriving an analytical model for predicting the critical length of nano particle as a function of its orientation to the macro scale crack path in the matrix. The model takes inspiration from the research accomplished in Chapter 3-5, where large increases in Mode I and mixed mode fracture energies was achieved with the addition of small quantities of nano graphene. The specific aim of this chapter is the ability to predict the orientation of nano particles for a given loading on a structure, as well as the minimum separation distance necessary to keep the particles from interacting.

## 6.2 Nano scale fracture derivation for Mixed-Mode loading

### 6.2.1 Critical nano particle length calculation

Fig. 6.2 depicts a macro-scale crack impinging on a nanoplatelet (shown in green), where the angle made by the nanoplatelet with the global X-direction is  $\beta$ , and the angle made by the crack with the global X-direction is  $\alpha$ . The cracked-body is subjected to multi-axial external stress field as shown in Fig. 6.2, with the maximum principal stress direction making an angle  $\theta$  with the local  $X_1$ -direction which is collinear with the longitudinal axis of the nanoparticle. On the principal plane at the nano-particle tip under plane stress conditions, the local shear stress ( $\tau_{12}$ ) must vanish, giving [135],

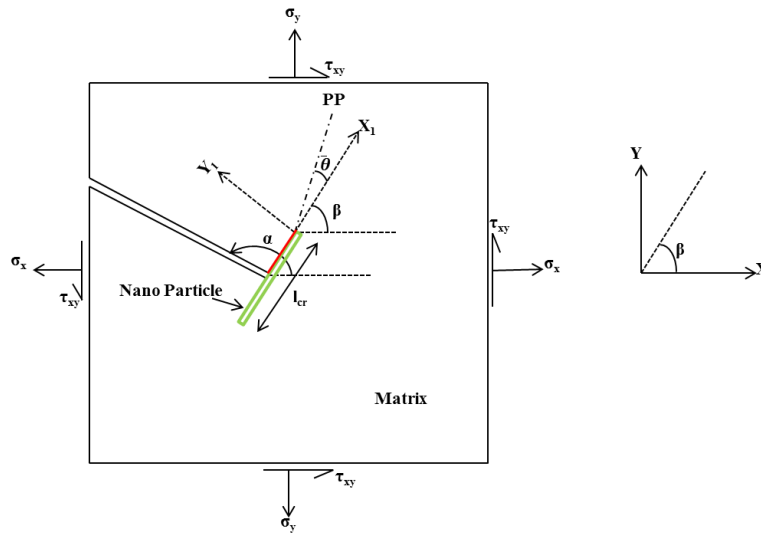


**Figure 6.2** Schematic of the nano particle optimization for fracture toughness enhancement

$$K_I \sin \frac{\bar{\theta}}{2} (1 + \cos \bar{\theta}) = K_{II} \cos \frac{\bar{\theta}}{2} (1 - 3 \cos \bar{\theta}) \quad (6.3)$$

Where,  $K_I$  is the Mode I stress intensity factor and  $K_{II}$  is Mode II stress intensity factor,

$$K_I = \sigma_{22,o} \sqrt{\pi l_n} \quad (6.4)$$

$$K_{II} = \tau_{12,o} \sqrt{\pi l_n} \quad (6.5)$$

Where, ‘o’ implies far-field stresses and  $l_n$  is the length of the nano-particle. Using global-local stress transformation,

$$\sigma_{11,o} = \sigma_x \cos^2 \beta + \sigma_y \sin^2 \beta + 2\tau_{xy} \sin \beta \cos \beta \quad (6.6)$$

$$\sigma_{22,o} = \sigma_x \sin^2 \beta + \sigma_y \cos^2 \beta - 2\tau_{xy} \sin \beta \cos \beta \quad (6.7)$$

$$\tau_{12,o} = -\sigma_x \sin \beta \cos \beta + \sigma_y \sin \beta \cos \beta + \tau_{xy} (\cos^2 \beta - \sin^2 \beta) \quad (6.8)$$

Combining Eqns. (6.3)-(6.8), the direction of the principal plane ( $\bar{\theta}$ ) can be obtained directly from the global stresses for the plane stress case.

$$\frac{K_{II}}{K_I} = -\frac{\sin \bar{\theta}}{3 \cos \bar{\theta} - 1} = \frac{\tau_{12,o} \sqrt{\pi l_n}}{\sigma_{22,o} \sqrt{\pi l_n}} = \frac{\tau_{12,o}}{\sigma_{22,o}} = F(\beta) \quad (6.9)$$

The principal axis orientation  $\bar{\theta}$  relative to the nano particle is solved using Eqn. (6.9) to get,

$$\sin \bar{\theta} - F(\beta)(1 - 3 \cos \bar{\theta}) = 0 \quad (6.10)$$

Eqn. (6.10) can be solved as:

$$\begin{aligned} \sin \bar{\theta} &= F(\beta) - 3F(\beta) \cos \bar{\theta} \\ \Rightarrow \sqrt{1 - \cos^2 \bar{\theta}} &= F(\beta) - 3F(\beta) \cos \bar{\theta} \\ \Rightarrow (1 - \cos^2 \bar{\theta}) &= F^2(\beta) + 9F^2(\beta) \cos^2 \bar{\theta} - 6F^2(\beta) \cos \bar{\theta} \\ \Rightarrow (9F^2(\beta) + 1) \cos^2 \bar{\theta} - 6F^2(\beta) \cos \bar{\theta} + (F^2(\beta) - 1) &= 0 \\ \cos \bar{\theta} &= \frac{6F^2(\beta) \pm \sqrt{36F^4(\beta) - 4(9F^2(\beta) + 1)(F^2(\beta) - 1)}}{2(9F^2(\beta) + 1)} \\ \Rightarrow \cos \bar{\theta} &= \frac{3F^2(\beta) \pm \sqrt{8F^2(\beta) + 1}}{(9F^2(\beta) + 1)} \\ \Rightarrow \bar{\theta} &= \cos^{-1} \left[ \frac{3F^2(\beta) \pm \sqrt{8F^2(\beta) + 1}}{(9F^2(\beta) + 1)} \right] \end{aligned} \quad (6.11)$$

From Fig. 6.2, the crack angle  $\alpha$  w.r.t to the global X axis, can be expressed as,

$$\alpha = \beta + 90^\circ \quad (6.12)$$

Also, the Mode I critical stress factor can be expressed as [135],

$$K_{IC,matrix} = \frac{1}{2} K_I \cos \frac{\bar{\theta}}{2} (1 + \cos \bar{\theta}) - \frac{3}{2} K_{II} \sin \frac{\bar{\theta}}{2} (1 + \cos \bar{\theta}) \quad (6.13)$$

From Eqns. (6.7) and (6.8),

$$\tau_{12,o} = \left[ \frac{-\sigma_x \sin \beta \cos \beta + \sigma_y \sin \beta \cos \beta + \tau_{xy} (\cos^2 \beta - \sin^2 \beta)}{\sigma_x \sin^2 \beta + \sigma_y \cos^2 \beta - 2\tau_{xy} \sin \beta \cos \beta} \right] \sigma_{22,o} \quad (6.14)$$

$$\tau_{12,o} = \left[ \frac{c_3(\beta)}{c_2(\beta)} \right] \sigma_{22,o} = F(\beta) \sigma_{22,o}$$

Substituting, Eqns. (6.4), (6.5), (6.9) and (6.14) in (6.13),

$$K_{IC,matrix} = \frac{\sigma_{22,o} (1 + \cos \bar{\theta}) \sqrt{\pi l_n}}{2} \left[ \cos \frac{\bar{\theta}}{2} - 3F(\beta) \sin \frac{\bar{\theta}}{2} \right] \quad (6.15)$$

When the size of the nano particle  $l_n \leq a_{cr}$ , where  $a_{cr}$  is the critical crack length, the far field stress must satisfy the condition [134],

$$\sigma_{22,o} = \sigma_{th,matrix} \quad (6.16)$$

Where,  $\sigma_{th,matrix}$  is the theoretical strength of the matrix (epoxy). Substituting Eqn. (6.16) in (6.15)

and solving for  $l_{n,cr}$  gives,

$$l_{n,cr} = \frac{4K_{IC,matrix}^2}{\pi \sigma_{th,matrix}^2 (1 + \cos \bar{\theta})^2 \left[ \cos \frac{\bar{\theta}}{2} - 3 \left[ \frac{-\sigma_x \sin \beta \cos \beta + \sigma_y \sin \beta \cos \beta + \tau_{xy} (\cos^2 \beta - \sin^2 \beta)}{\sigma_{th,matrix}} \right] \sin \frac{\bar{\theta}}{2} \right]^2} \quad (6.17)$$

Where,  $l_{n,cr}$  is the critical nano particle length required for enhanced toughness under planar mixed-mode loading for a nanoparticle oriented at an angle  $\beta$  to the macro-scale crack path.

### 6.2.2 NGP wt% calculation

The near crack-tip stress field, can be calculated as [135],

$$\sigma_{22} = \frac{K_I}{\sqrt{2\pi r}} \frac{1}{2} \cos \frac{\theta}{2} (1 + \cos \theta) - \frac{K_{II}}{\sqrt{2\pi r}} \frac{3}{2} \sin \frac{\theta}{2} (1 + \cos \theta) \quad (6.18)$$

Assuming,  $K_I = \sigma_{22,o} \sqrt{\pi a}$ ,  $K_{II} = \tau_{12,o} \sqrt{\pi a}$ , where  $a$  is the crack length,

$$\frac{\sigma_{22}}{\sigma_{22,o}} = \sqrt{\frac{a}{2r}} \left\{ \frac{1}{2} \cos \frac{\theta}{2} (1 + \cos \theta) - \frac{\tau_{12,o}}{\sigma_{22,o}} \frac{3}{2} \sin \frac{\theta}{2} (1 + \cos \theta) \right\} \quad (6.19)$$

Similarly,

$$\frac{\tau_{12}}{\tau_{12,o}} = \sqrt{\frac{a}{2r}} \left\{ \frac{\sigma_{22,o}}{\tau_{12,o}} \frac{1}{2} \sin \frac{\theta}{2} (1 + \cos \theta) - \frac{1}{2} \cos \frac{\theta}{2} (1 - 3 \cos \theta) \right\} \quad (6.20)$$

For  $\sigma_{22}$  and  $\tau_{12}$  to equal far-field stresses simultaneously, setting,  $\frac{\sigma_{22}}{\sigma_{22,o}} = 1$  in Equation (6.19) and

$\frac{\tau_{12}}{\tau_{12,o}} = 1$  in Equation (6.20), yield respectively,

$$r_\sigma = \frac{a}{2} \left\{ \frac{1}{2} \cos \frac{\theta}{2} (1 + \cos \theta) - \frac{3}{2} F(\beta) \sin \frac{\theta}{2} (1 + \cos \theta) \right\}^2 \quad (6.21)$$

And,

$$r_\tau = \frac{a}{2} \left\{ \frac{1}{F(\beta)} \frac{1}{2} \sin \frac{\theta}{2} (1 + \cos \theta) - \frac{1}{2} \cos \frac{\theta}{2} (1 - 3 \cos \theta) \right\}^2 \quad (6.22)$$

For a repeating unit cell (RUC) depicted in Fig. 6.3, the maximum value of ' $r$ ' at which both the normal and shear stresses decrease below the far field stress level at nearest neighbor crack tip is given by,

$$r_{\max} \geq r_\sigma \Big|_{\theta=\pm\frac{\pi}{2}} \geq r_\tau \Big|_{\theta=\pm\frac{\pi}{2}}$$

From Eqn. (6.21),

$$r_{\sigma} \left( \frac{\pi}{2} \right) = \frac{a_{cr}}{16} \{1 - 3F(\beta)\}^2 \quad (6.23)$$

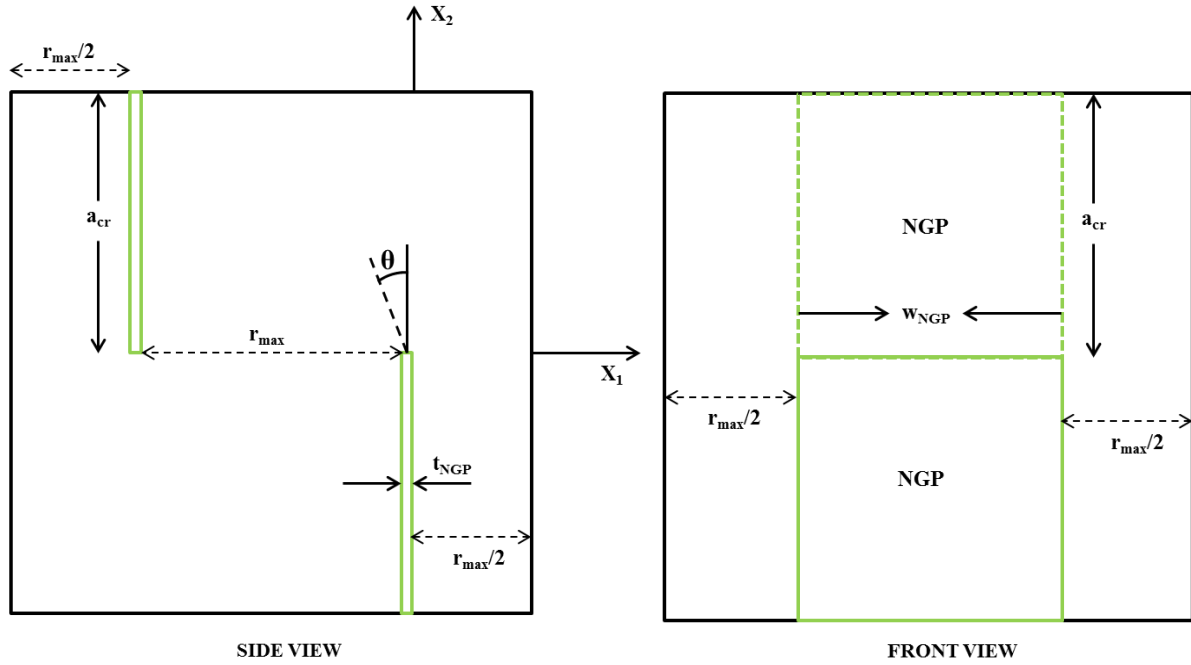


**Figure 6.3** RUC of NGP in polymer matrix

And,

$$r_{\sigma} \left( -\frac{\pi}{2} \right) = \frac{a_{cr}}{16} \{1 + 3F(\beta)\}^2 \quad (6.24)$$

From Eqn. (6.22),

$$r_{\tau} \left( \frac{\pi}{2} \right) = \frac{a_{cr}}{16} \left\{ \frac{1}{F(\beta)} - 1 \right\}^2 \quad (6.25)$$

And,

$$r_{\tau} \left( -\frac{\pi}{2} \right) = \frac{a_{cr}}{16} \left\{ \frac{1}{F(\beta)} + 1 \right\}^2 \quad (6.26)$$

The maximum of the above four Equations (6.23)-(6.26) is selected to be  $r_{max}$ . Finally, the NGP volume fraction required in the RUC can be calculated as follows:

Length of RUC ( $l_{RUC}$ ) =  $2 a_{cr}$ ; Width of RUC ( $w_{RUC}$ ) =  $2 r_{max}$ ; Depth of RUC ( $d_{RUC}$ ) =  $W_{NGP} + r_{max}$

Hence, volume of RUC ( $V_{RUC}$ ) =  $4 a_{cr} r_{max} (W_{NGP} + r_{max})$

Volume of NGP ( $V_{NGP}$ ) =  $2 a_{cr} W_{NGP} t_{NGP}$

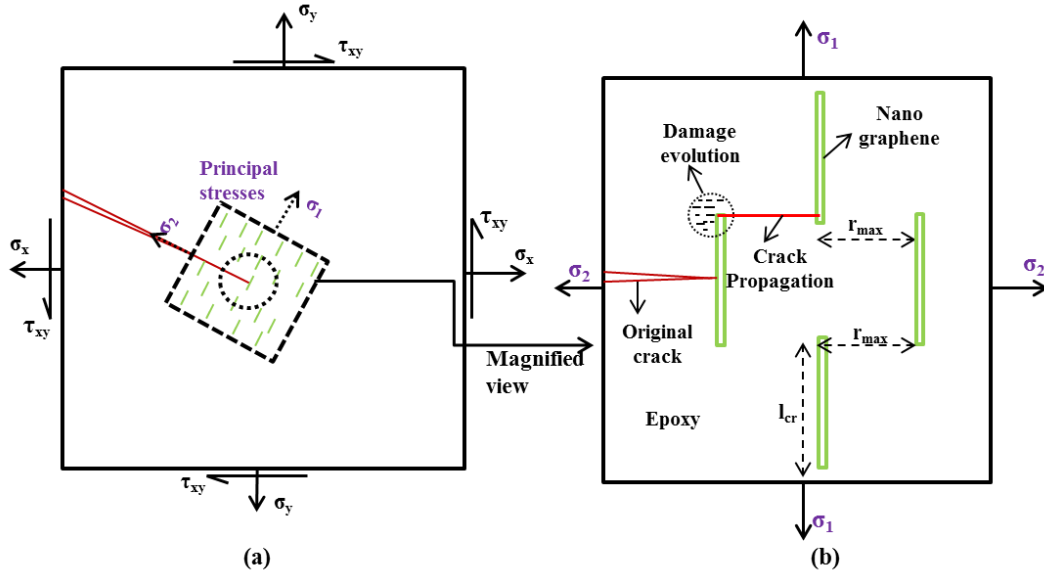


**Figure 6.4** Schematic of crack propagation and damage evolution in presence of NGP

$$\text{Hence, Volume fraction } (V_F) = \frac{V_{NGP}}{V_{RUC}} = \frac{n_{NGP} W_{NGP} t_{NGP}}{2r_{max} (W_{NGP} + r_{max})}$$

Where,  $n_{NGP}$  is the number of NGPs in the RUC;  $W_{NGP}$  is the average width of the NGPs;  $t_{NGP}$  is the thickness of the NGPs.

Weight% of NGP can then be calculated as,

$$Wt(\%) = \left( V_F \cdot \frac{\rho_{NGP}}{\rho_{EPON}} \right) \times 100$$

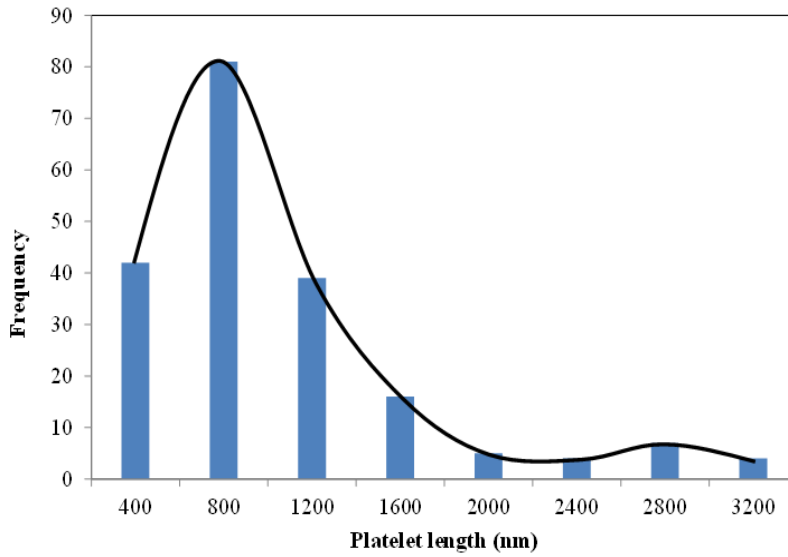
### 6.2.3 Damage evolution

Fig. 6.4(a) shows a specimen with an arbitrary crack orientation with NGPs reinforcing the matrix. NGPs are assumed to be perfectly aligned in this case. Fig. 6.4 (b) shows a magnified view of a small element in the specimen in the NGP reference frame. The figure depicts an RUC

type (Fig. 6.3) view, with each NGP at a distance of  $r_{\max}$  from each other. The figure shows a crack deflection when it encounters an NGP and an evolving damage in the matrix with crack nucleation followed by formation of larger cracks. This crack moves through the matrix until it encounters another NGP, and the damage propagates.

For the above assumption to be accurate the length of the nano-particle has to be less than  $a_{cr}$  as discussed above. For an epoxy (for example, EPON 862), the critical crack length can be calculated by using  $K_{IC}=0.78 \text{ MPa}\cdot\text{m}^{1/2}$ , and  $\sigma_{th} =275 \text{ MPa}$  [31,136], which gives an approximate value of  $a_{cr}=2560 \text{ nm}$ .

To have confidence in the proposed theory, the solutions of un-passivated NGPs using the dispersion process as in Chapter 3 were prepared. The solutions were dropped on copper grids for analysis under the TEM. A statistical study of size of 200 platelets was done, which has been presented in Fig. 6.5 as a frequency distribution. As can be seen more than 90% of the platelets lie within the 2560nm critical size calculated. Fig. 6.6 plots the cumulative probability of the size of the NGP size. As can be seen from the plot, there is more than 90% probability of the NGPs to lie below the critical size calculated, which ensures confidence in the presented model as a reinforcing phenomenon due to the presence of NGPs.



**Figure 6.5** Platelet length distributions

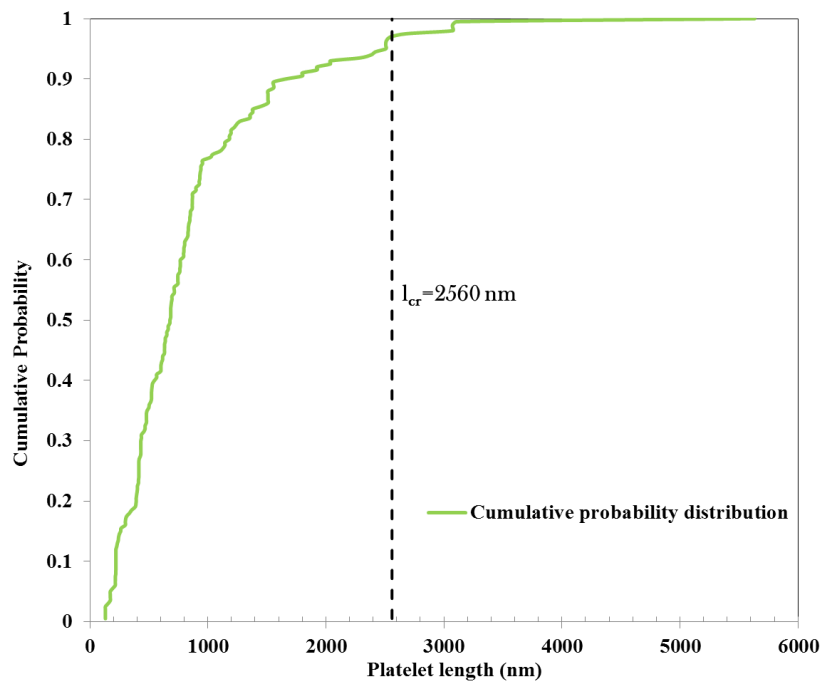


**Figure 6.6** Cumulative probability of platelet length distribution

#### 6.2.4 Computation in Matlab

A general code for using the above methodology was programmed in Matlab to study the length scale requirement for the nano particle for any arbitrary crack angle. The code can be modified for any epoxy matrix by changing the fracture toughness and theoretical strength. The code gives

a complete sweep of the nano particle length ( $l_{cr}$ ) for a crack angle from  $0^\circ$  to  $360^\circ$ . A nominal value for the nanoparticle location  $\beta$  was calculated for each crack location using  $\beta_{nominal} = \alpha - 90^\circ$ . The angle  $\beta$  was then swept for  $\pm 45^\circ$  around  $\beta_{nominal}$  to generate a critical length curve for varying nano particle orientations for same  $\alpha$  (crack location). Any arbitrary loading (normal, shear or a combination of both) can be applied to the cases studied.

Some important points to note regarding the computation are as follows:

- (1) The positive part of the solution (6.11) is considered, since the negative part blows up the solution.
- (2) The value of the denominator  $c_2(\beta)$  can tend to zero, which can drive  $F(\beta)$  to infinity.

Assume  $\lim_{F(\beta) \rightarrow \infty} \bar{\theta} = \cos^{-1}(\frac{1}{3})$  from Equation (6.11).

- (3) Since  $c_2(\beta)$  is the local  $\sigma_{22,o}$ , the cases for which it goes negative (compressive loading) are not permissible. These areas are shown as ‘red crosses’ in the plot region. As an assumption,  $c_2(\beta)$  tending to zero is also included in this region.

- (4) The code can be fed any arbitrary loading  $\sigma_x$ ,  $\sigma_y$  and  $\tau_{xy}$ .

### 6.2.5 Case study: Compact Tension test

Consider Fig. 6.7, for a specimen of width  $2h$  and applied global loading  $P$ ,

$$\begin{aligned} K_I &= \sigma_o \sqrt{\pi a} \\ K_{II} &= \tau_o \sqrt{\pi a} \end{aligned} \tag{6.27}$$

Where far field normal  $\sigma_o$  and shear stress  $\tau_o$  can be assumed as, ( $M$  is moment at the crack-tip)

$$\sigma_o = \frac{M h/2}{I} = \frac{6P(a_o - r_o)}{bh^2} \quad (6.28)$$

$$\tau_o = \frac{P}{bh}$$

Where,  $b$  is the thickness of the specimen.

For principal stress direction near crack tip, Equations (6.27) and (6.28) can be used to get,

$$\frac{6(a_o - r_o)}{h} \sin \frac{\bar{\theta}}{2} (1 + \cos \bar{\theta}) = \cos \frac{\bar{\theta}}{2} (1 - 3 \cos \bar{\theta}) \quad (6.29)$$

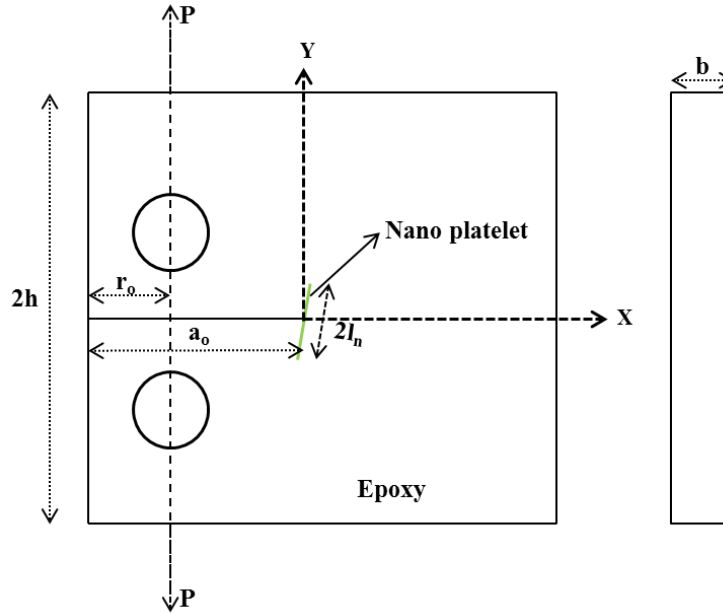


**Figure 6.7** Schematic of the CT specimen with nano platelet

Rewriting Eqn. (6.30) as,

$$\tan \frac{\bar{\theta}}{2} \frac{(1 + \cos \bar{\theta})}{(1 - 3 \cos \bar{\theta})} = \frac{h}{6(a_o - r_o)} \quad (6.30)$$

This equation can be solved for principal axis location, if the size of the CT specimen is known.

Using Eqn. 6.13 to solve for  $K_{IC, \text{matrix}}$ , and substituting Eqns. (6.27) and (6.28), for critical state,

$$K_{IC,matrix} = \frac{1}{2} \sqrt{\pi l_{cr}} (1 + \cos \bar{\theta}) \left( \sigma_{th} \cos \frac{\bar{\theta}}{2} - 3\tau_o \sin \frac{\bar{\theta}}{2} \right) \quad (6.31)$$

Hence,

$$l_{cr} = \frac{4K_{IC,matrix}^2}{\pi(1 + \cos \bar{\theta})^2 \left( \sigma_{th} \cos \frac{\bar{\theta}}{2} - 3\tau_o \sin \frac{\bar{\theta}}{2} \right)^2} \quad (6.32)$$

Asssuming,  $\frac{\tau_o}{\sigma_{th}} = \frac{P/bh}{6P(a_o - r_o)/bh^2}$  from (6.28) and substituting in (6.32), we get,

$$l_{cr} = \frac{4K_{IC}^2}{\pi(1 + \cos \bar{\theta})^2 \sigma_{th}^2 \left( \cos \frac{\bar{\theta}}{2} - \frac{h}{2(a_o - r_o)} \sin \frac{\bar{\theta}}{2} \right)^2} \quad (6.33)$$

Using the values from the experimental data from Kumar et al [31], for addition of 0.5 wt% of graphene nano platelets to EPON 862 matrix at fracture, we can approximate the values of the loading for the code input as,

$$\begin{aligned} \sigma_x &= \frac{6 \times 260.35 \times 0.46}{0.25 \times 0.6^2} = 12.375 MPa \\ \tau_{xy} &= \frac{260.35}{0.25 \times 0.6} = 2.69 MPa \\ \sigma_y &= \frac{6P(\frac{1}{2}a_o - r_o + h)}{b(2h - a_o)^2} = 26.62 MPa \end{aligned}$$

Where,  $P = P_{max} = 260.35$  N from Kumar et al [31].

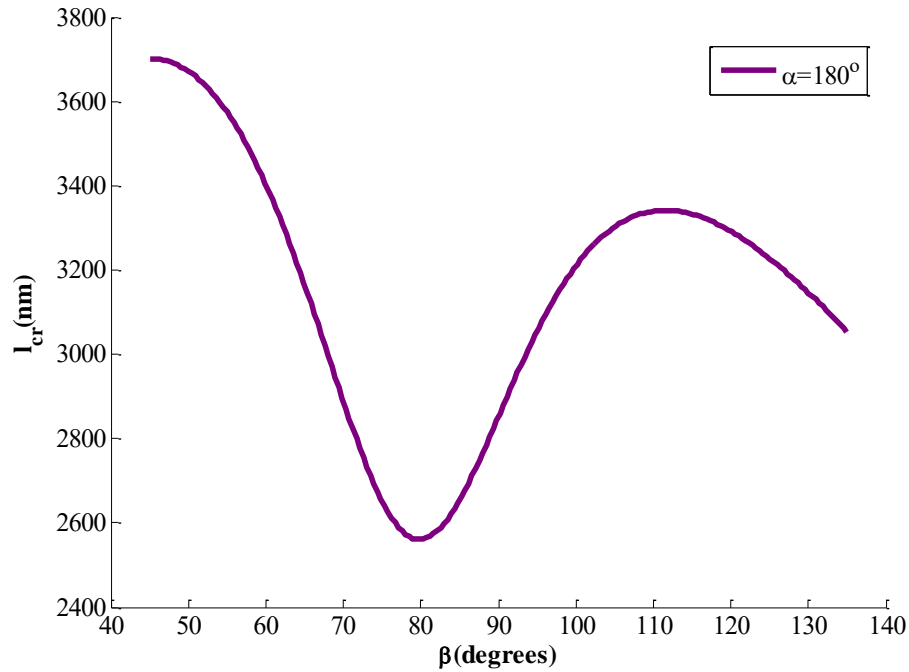


**Figure 6.8** Critical nano particle length variation with nano particle orientation

Since the crack angle,  $\alpha = 180^\circ$  for this particular case, the case results can be displayed using the general code for getting the critical nano particle size estimates. Fig. 6.8 gives the smallest nano particle size required for varying nano particle orientations for a fixed crack angle of  $180^\circ$  for maximum toughness enhancements. Fig. 6.9 shows the variation of the principal axis position with respect to the nano particle orientation  $\beta$ . For this special case the minimum value of  $l_{cr} = 2560$  nm calculated in Section 6.2.3 occurs at  $\beta = 79.82^\circ$ .

The above computations present a special case of a CT specimen for a particular loading. Since, the code can be changed to incorporate any type of matrix, or nano particle, the code in itself is very powerful in predicting the length requirements of the nano particle (NGPs in our case) for varying nano particle orientations. This opens up the discussion of alignment of nano particles and tailoring of the properties of the matrix and in turn composites in a particular direction.

Since the focus of this dissertation is on graphene, the next section discusses yet another important topic, the alignment of NGPs in an epoxy matrix.

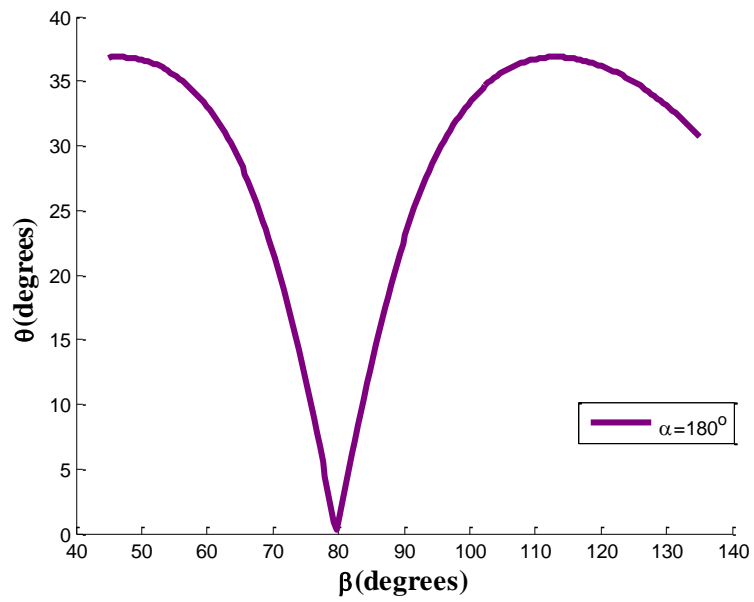


**Figure 6.9** Principal axis variation with nano particle orientation

## CHAPTER 7

### MULTISCALE MODELING OF NANO GRAPHENE/CARBON FIBER REINFORCED EPON 862 COMPOSITES

#### **7.1 Summary**

The bottleneck for inserting new and improved polymer matrix composites (PMC) is the overwhelming amount of testing required to incorporate new material into the Design Allowables Database. This extensive testing is a direct consequence of the system designer's need to address uncertainty and reduce risk, specifically, how variations in the constituent materials, the processing, the manufacturing process, and end-use scenarios propagate into performance and failure of a component. The development of the Design Allowables Database requires evaluation of multiple batches of composites with the associated construction of very large mechanical and other physical properties databases. Also, to quantify uncertainty in the structural performance (i) numerous subcomponents may have to be fabricated requiring expensive tooling and (ii) one must then perform expensive tests on these elements to determine their long-term performance. Moreover, additional time and cost are incurred if there are any complications (complications are typical) such as tooling rework, large error bands in mechanical properties, or processing complications.

In this context, Integrated Computational Materials Science and Engineering (ICMSE) provides a methodology to support materials development without recourse to expensive trial-and-error approach to materials fabrication and characterization. The motivation for the proposed research is that design requirements and knockdown factors are limiting our ability to exploit advanced

composite and nanostructured composite materials for system-level payoffs. The challenge in achieving these goals stems from our current inability to accurately predict end-of-life properties, damage tolerance, and durability of multi-functional PMCs.

A multi-scale physics-based modeling approach, in which individual roles of constituent materials and their interfaces are recognized, is necessary to accurately represent the material anisotropy, to the level of fidelity required for predicting the response of PMC aircraft structures and thereby provide progressive failure prediction capability. In this approach schematically depicted in Fig. 7.1, nanoscale (atomistic) simulations provide input data for the micro-mechanical response, which, in turn provides input to a three dimensional ply-level analysis capable of modeling the spatial variability of material properties and multi-functionality in the material and also account for the ply-level stresses that could ultimately initiate failure in an aircraft structure. Details regarding the implementation of this hierarchical mechanism-based progressive failure prediction model are presented in the following sections.

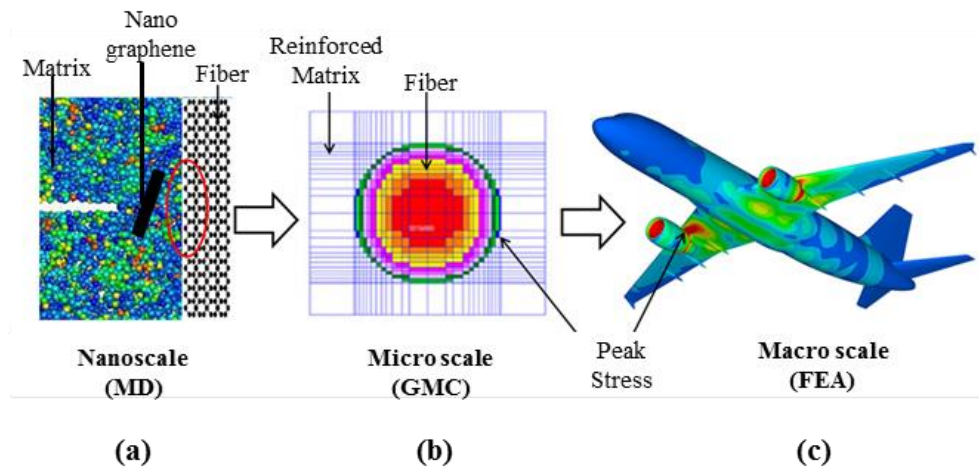


**Figure 7.1** Schematic of a nano-micro-macro hierarchical multiscale model

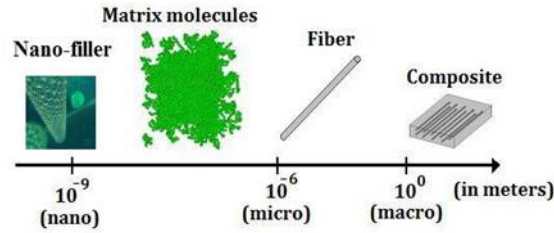


**Figure 7.2** Length scales involved in multi-scale modeling

## 7.2 Atomistic Level Analysis using Molecular Dynamics (MD)

The nanoscale interaction between polymer molecules and nanoparticles is a key factor in determining the macroscale strength of advanced composites. In recent years numerous efforts have been directed towards modeling nanocomposites in order to better understand the reasons behind the enhancement of mechanical properties, even with the slight addition (<1 wt%) of nanoparticles. In order to better understand the local influence of nanoparticle on the failure response of the polymer, a nanoscale analysis is required. The bond-order based ReaxFF [137] force field is used, that allows for bond-breakage. ReaxFF can effectively simulate bond formation and breakage, which is a more accurate representation of the polymer fracture process. Based on data obtained from the Density Functional Theory (DFT), ReaxFF models the breakage of covalent bonds within a polymer network by reducing the bond order of the covalent bonds. When the bond order between two adjacent atoms reduces to zero, a complete bond separation is implied. The open-source MD software LAMMPS was used, in conjunction with ReaxFF, to model the interaction between polymer and nanographene platelets. A novel repeating volume element (RVE) based approach termed Nanoscale Informed Damage Mechanics (NIDM) developed by Roy et. al [138] was employed to obtain the elastic stiffness tensor as well as the damage-induced inelastic behavior of the polymer matrix, with and without the reinforcing effect of the nanographene platelet. To our knowledge this novel approach has not been attempted for

polymer matrix composites to date, and it was used to provide input of material properties for higher length-scale models as discussed in the following sections.

A key element of this chapter is the integrated coupling of multi-scale computations spanning a wide range of spatial and temporal scales, with an emphasis on assessing the effects of evolution of damage entities in the composite structure on relevant aspects of multi-functionality as depicted in Fig. 7.2. Data obtained from lower length scale calculations (i.e., MD) feeds into hierarchical repeating unit cell (RUC) based multiscale progressive failure models of nanoparticle reinforced composites as shown in Fig. 7.1(b).

### **7.3 Micro-mechanics Level Analysis using the Generalized Method of Cells**

An efficient semi-analytical multiscale homogenization procedure using the Generalized Method of Cells (GMC) micromechanical theory [139, 140], as implemented in the NASA-developed code MAC/GMC (Micromechanics Analysis Code with GMC) [141, 142], can be extended and utilized in the design and analysis of multifunctional nanocomposites. Toughness, strength, and stiffness data from nanoscale (NIDM simulations) are input to MAC/GMC which is then used to obtain homogenized RUC properties at the microscale, fully accounting for stress amplification due to the presence of the carbon fiber within the resin matrix as well as the reinforcing effect of the nanoparticles present in the matrix.

Such properties are used to feed into successively higher length scale RUCs containing microscale features (i.e., continuous fibers, effective matrix, fiber/matrix interface, as shown schematically in Fig. 7.2) and/or mesoscale structures (individual or woven fiber tows, effective matrix, etc.). Fig. 7.3 shows two of the many choices of RUCs available in MAC/GMC to model the micro scale sub-cells, e.g., doubly periodic (2-D) or triply periodic (3-D), depending on the application.

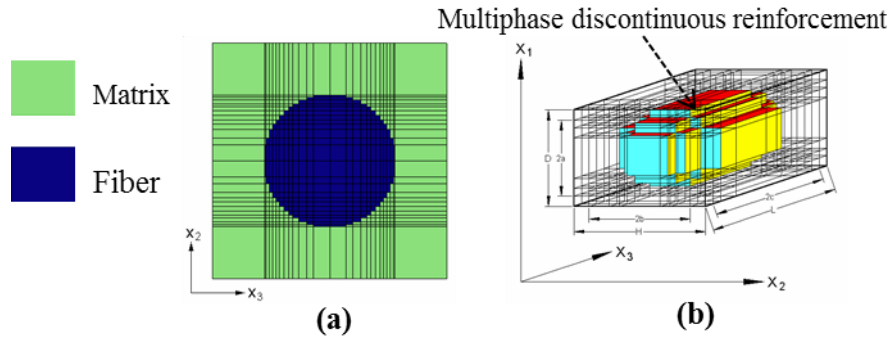


**Figure 7.3** MAC/GMC RUCs (a) Doubly periodic (b) triply periodic

Homogenized ply-level properties obtained from the highest length scale RUC are then used to establish finite element stiffness properties for use in global structural models. Analogously, finite element integration point stresses obtained from a global structural analysis are mapped onto the highest length scale RUC for use in an iterative progressive failure analysis using MAC/GMC. Local field quantities obtained within a given RUC are used to establish boundary conditions for use in progressive failure analysis at the next lower length scale RUC. This multiscale modeling methodology involves a robust local-to-global iteration strategy, where a hierarchy of RUCs may be used to explicitly model composite material structure, morphology, and failure over a range of length scales. The effect of local damage or failure at a given length scale is automatically propagated at each load or time step to the global finite element scale through the change in homogenized micro-scale properties.

In GMC for continuous (or discontinuous) fibrous composites, the RUC can consist of an arbitrary number of phases. Hence GMC is capable of modeling a multiphase composite. This generalization extends the modeling capability of the method of cells to include the following: 1) inelastic thermomechanical response of multiphased metal matrix composite, 2) modeling of various fiber architectures (including both shape and packing arrangements), 3) modeling of

porosities and damage, and 4) the modeling of interfacial regions around inclusions including interfacial degradation [141].

The basic homogenization approach employed in the micromechanical analysis consists essentially of four steps. First, the RVE of the periodic composite structure is identified. Here, it should be recalled that the RVE represents the smallest section of the composite structure that captures the full physics of the problem (e.g., packing, fiber-fiber interactions etc.), whereas the RUC is the smallest repeating unit cell that is derived purely from the geometry and/or symmetry of the structure. Second, the macroscopic or average stress and strain state in terms of the individual microscopic (subcell) stress and strain states is defined. Third, the continuity of tractions and displacements are imposed at the boundaries between the constituents. These three steps, in conjunction with microscale equilibrium, establish the relationship between micro (subcell) total, thermal and inelastic strains and macro (composite) strains via relevant concentration tensors. In the fourth and final step, the homogenized macro constitutive equations of the composite RVE are determined. These four steps form the basis of the micro-to-macro mechanics analysis which describes the behavior of a heterogeneous media.

The resulting micromechanical analysis establishes the overall (macro) behavior of the multi-phase composite and is expressed as a constitutive relation between the volume averaged stress ( $\bar{\sigma}$ ), kinematic strain ( $\bar{\epsilon}$ ), thermal strain ( $\bar{\epsilon}^T$ ), and inelastic strains ( $\bar{\epsilon}^I$ ), in conjunction with the effective elastic stiffness tensor,  $B^*$  [142].

Hence,

$$\bar{\sigma} = B^* (\bar{\epsilon} - \bar{\epsilon}^I - \bar{\epsilon}^T) \quad (7.1)$$

where, for the most general case of a discontinuous reinforcement, with  $N_\alpha$  by  $N_\beta$  by  $N_\gamma$  number of subcells in the RUC, the volume averaged effective elastic stiffness matrix  $B^*$ , is given by,

$$\tilde{\mathbf{B}}^* = \frac{1}{dhl} \sum_{\alpha=1}^{N_\alpha} \sum_{\beta=1}^{N_\beta} \sum_{\gamma=1}^{N_\gamma} d_\alpha h_\beta l_\gamma \mathbf{C}^{(\alpha\beta\gamma)} \mathbf{A}^{(\alpha\beta\gamma)} \quad (7.2)$$

where  $d_\alpha, h_\beta, l_\gamma$  are the subcell depth, height, and length, respectively. The matrix  $\mathbf{C}^{(\alpha\beta\gamma)}$  represents the elastic stiffness tensor of the fiber, and each matrix subcell obtained from the nano scale using the NIDM model for a specific wt% of randomly oriented NGPs. The volume averaged composite inelastic strain vector is defined as:

$$\tilde{\boldsymbol{\varepsilon}}^I = \frac{-\mathbf{B}^{*-1}}{dhl} \sum_{\alpha=1}^{N_\alpha} \sum_{\beta=1}^{N_\beta} \sum_{\gamma=1}^{N_\gamma} d_\alpha h_\beta l_\gamma \mathbf{C}^{(\alpha\beta\gamma)} (\mathbf{D}^{(\alpha\beta\gamma)} \boldsymbol{\varepsilon}_s^I - \tilde{\boldsymbol{\varepsilon}}^{I(\alpha\beta\gamma)}) \quad (7.3)$$

The volume averaged thermal strain vector is defined as,

$$\tilde{\boldsymbol{\varepsilon}}^T = \frac{-\mathbf{B}^{*-1}}{dhl} \sum_{\alpha=1}^{N_\alpha} \sum_{\beta=1}^{N_\beta} \sum_{\gamma=1}^{N_\gamma} d_\alpha h_\beta l_\gamma \mathbf{C}^{(\alpha\beta\gamma)} (\mathbf{D}^{(\alpha\beta\gamma)} \boldsymbol{\varepsilon}_s^T - \tilde{\boldsymbol{\varepsilon}}^{T(\alpha\beta\gamma)}) \quad (7.4)$$

where  $\tilde{\boldsymbol{\varepsilon}}$  is the uniformly applied macro level strain,  $\boldsymbol{\varepsilon}_s^I$  and  $\boldsymbol{\varepsilon}_s^T$  are the inelastic and thermal subcell strains. In the above equations, matrix notation is employed, and,

$$\begin{aligned} \bar{\boldsymbol{\sigma}} &= \{\bar{\sigma}_{11}, \bar{\sigma}_{22}, \bar{\sigma}_{33}, \bar{\sigma}_{23}, \bar{\sigma}_{13}, \bar{\sigma}_{12}\} \\ \bar{\boldsymbol{\varepsilon}} &= \{\bar{\varepsilon}_{11}, \bar{\varepsilon}_{22}, \bar{\varepsilon}_{33}, 2\bar{\varepsilon}_{23}, 2\bar{\varepsilon}_{13}, 2\bar{\varepsilon}_{12}\} \\ \boldsymbol{\varepsilon}_s^I &= \{\bar{\boldsymbol{\varepsilon}}^{I(111)}, \dots, \bar{\boldsymbol{\varepsilon}}^{I(N_\alpha N_\beta N_\gamma)}\} \end{aligned} \quad (7.5)$$

It should be noted that a key step in the construction of this macro constitutive law is the derivation of the appropriate elastic concentration matrices  $\mathbf{A}^{(\alpha\beta\gamma)}$  and  $\mathbf{D}^{(\alpha\beta\gamma)}$  at the subcell level.

#### 7.4 Nano scale averaging law

A key aspect of the multiscale simulations is information transfer from various length scales. Molecular simulations of epoxy materials with and without nano particles as reinforcements using MD provide us with material definitions to be transferred to a higher length scale (micro or macro). When going to a higher length scale it is necessary to consider the orientation of the nano-particles or inclusions within the matrix. In previous chapters, epoxy reinforced with NGP

was used as our case of interest. Since during high shear mixing, the orientation of the platelets can be random, an anisotropic system (polymer system with NGP) at the nano scale will have to be converted to an averaged isotropic system, accounting for the random orientation of the NGPs. A general graphene platelet orientation in the epoxy matrix is depicted in Fig. 7.4.

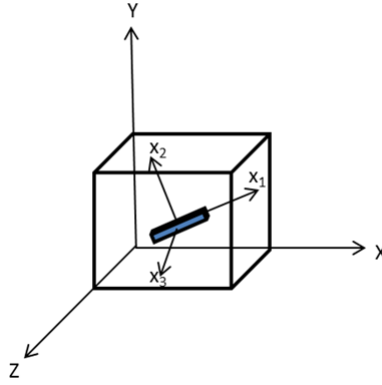


**Figure 7.4** Nano scale RVE with nano-graphene platelet

Assuming a set of Euler rotations which transforms the local  $x_1, x_2, x_3$  in the plane of the platelet to the global X, Y, Z axes (Fig. 7.5); the rotation matrix from local to global axes can be expressed as [143],

$$A = \begin{bmatrix} \cos \phi \cos \psi - \sin \phi \cos \gamma \sin \psi & \sin \phi \cos \psi + \cos \phi \cos \gamma \sin \psi & \sin \gamma \sin \psi \\ -\cos \phi \sin \psi - \sin \phi \cos \gamma \cos \psi & -\sin \phi \sin \psi + \cos \phi \cos \gamma \cos \psi & \sin \gamma \cos \psi \\ \sin \phi \sin \gamma & -\cos \phi \sin \gamma & \cos \gamma \end{bmatrix} \quad (7.6)$$

Then the orientation average of the stiffness tensor can be defined using the rotation matrix terms as [143],

$$\bar{C}_{ijkl}^{global} = \frac{\int_{-\pi}^{\pi} \int_0^{\pi} \int_0^{\pi/2} a_{ip} a_{jq} a_{kr} a_{ls} C_{pqrs}^{local} \lambda(\phi, \psi) \sin \gamma d\phi d\gamma d\psi}{\int_{-\pi}^{\pi} \int_0^{\pi} \int_0^{\pi/2} \lambda(\phi, \psi) \sin \gamma d\phi d\gamma d\psi} \quad (7.7)$$

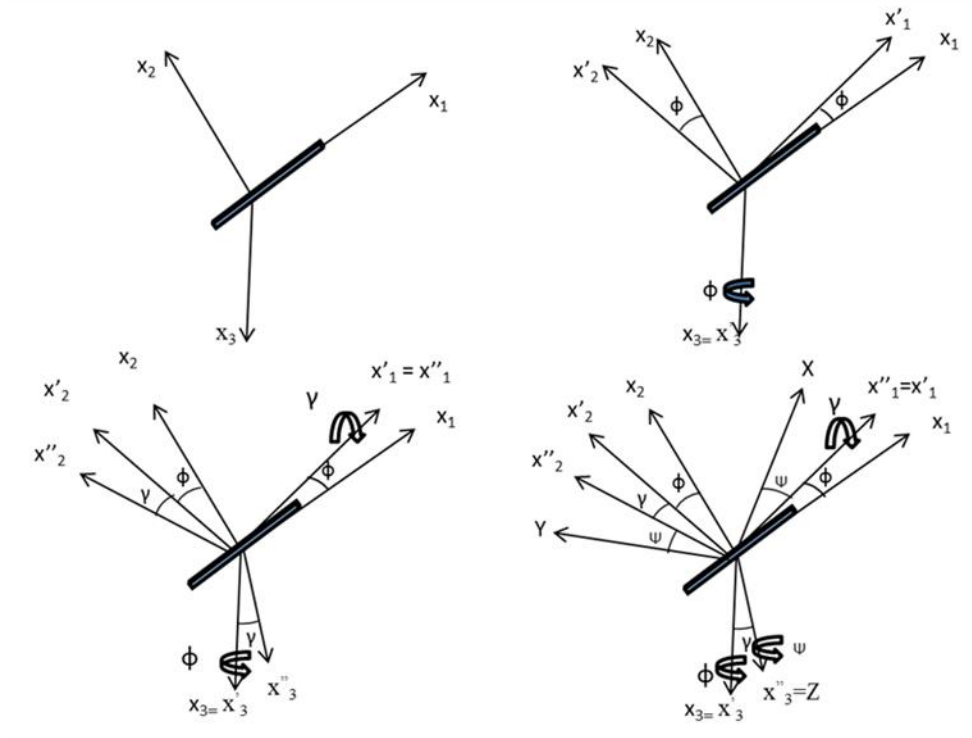


**Figure 7.5** Euler rotations for local to global transformation

where,  $\lambda(\phi, \psi) = e^{-s_1 \phi^2} e^{-s_2 \psi^2}$ ;  $s_1, s_2 = 0$  for a random orientation.

### 7.5 Three-Dimensional Ply-Level Analysis Using Finite Element Analysis and Multiscale coupling

The nanoscale modeling and the micromechanical level of modeling were developed and implemented within a synergistically coupled framework, developed at NASA, named MAC/GMC [142]. As mentioned earlier, data obtained from lower length scale calculations (i.e. NIDM) was used as an input for the hierarchical RUC based multiscale model of nanoparticle reinforced composites (GMC), which in turn provides input data to the macro scale FEA model.

One example of the hierarchical coupling methodology is Abaqus/MAC-GMC coupling for modeling continuous carbon fiber reinforced polymer nano-composites. A FORTRAN subroutine, FEAMAC developed by NASA acts a gateway between macro scale (Abaqus) and

micro scale (GMC) for a coupled simulation. Fig. 7.6 shows the transfer of information between the macro and the micro scale. At each time step of a macro scale simulation, global stresses are computed at element integration point, which is then transferred to the GMC model for the computation of local stresses based on the constitutive definition using Eqns. 7.1-7.4. The material properties for the resin subcells in an RUC are obtained from the nanoscale using NIDM.

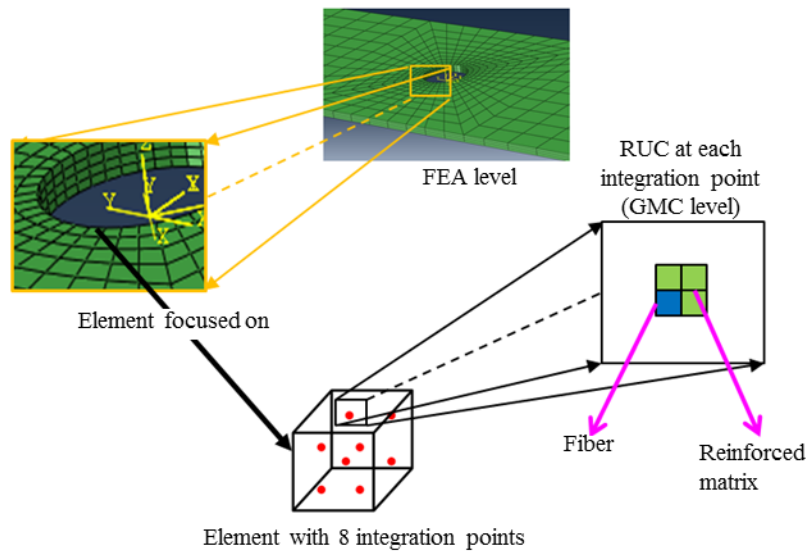


**Figure 7.6** Micro-macro coupling (MAC-GMC/Abaqus)

Any damage arising in the micro scale is propagated onto the next macro scale time-step through the degradation of element stiffness. This allows for damage evolution at micro and nano scales due to applied stresses at the macro scale since the constitutive material model can be directly formulated for the polymer matrix is directly formulated using MD simulations in conjunction with NIDM [138].

### 7.6 Results from Multi scale simulation of Open-hole Tension specimen

For highlighting the key aspects of the hierarchical methodology explained above, a test case is presented for better insight into the multiscale problem. Fig. 7.7 shows an example of an open-

hole tension (OHT) specimen for progressive failure modeling. The composite specimen is a  $[45/0/-45/90]_{2s}$  laminate with EPON 862 matrix and IM7 carbon fiber with 2.4 wt% of NGP as the nanoscale matrix reinforcement. The laminate size is 64mm×16mm with thickness of 0.5mm and the hole size is 3.175mm in diameter. Each modeling scale was defined using the following steps:

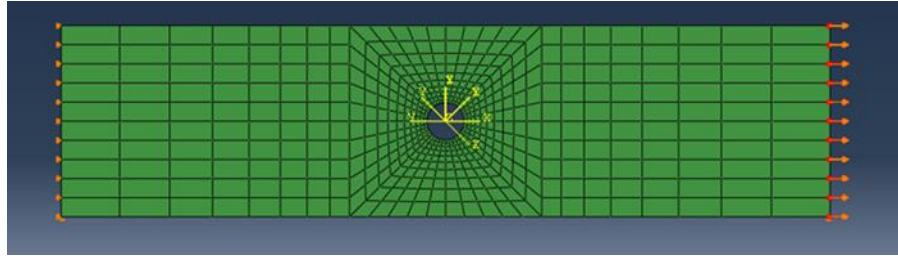


**Figure 7.7** OHT FEA model and boundary conditions in laminate

(1) Nano-scale stiffness and damage parameters for unreinforced (neat resin) and NGP reinforced EPON 862 (2 aspect ratio (AR) NGP, wt%=2.4) was obtained using tensile and shear simulations performed using MD with a Nano Informed Damage Mechanics method (NIDM) [138].

(2) As explained in Section 7.2, for incorporation of the above properties in the micro scale model (GMC), the stiffness parameters have to be homogenized assuming a random orientation of the nanographene in the EPON 862 matrix. From [138], the NGP reinforced polymer RVE comes out to be an orthotropic matrix which when reduced using the above tensor law (Eqns. 7.6-7.7), gives rise to an isotropic matrix. This is logical since the platelets are randomly oriented in the matrix. If the orthotropic matrix from [138] is given by,

$$C = \begin{bmatrix} C_{11} & C_{12} & C_{13} & 0 & 0 & 0 \\ C_{12} & C_{22} & C_{12} & 0 & 0 & 0 \\ C_{13} & C_{12} & C_{11} & 0 & 0 & 0 \\ 0 & 0 & 0 & G_{12} & 0 & 0 \\ 0 & 0 & 0 & 0 & G_{13} & 0 \\ 0 & 0 & 0 & 0 & 0 & G_{12} \end{bmatrix} \quad (7.8)$$

The orientation average counterpart using Eqns. 7.6-7.7 can be found to be,

$$\bar{C} = \begin{bmatrix} aA + bB + dD & gA + dB - bD & gA + dB - bD & 0 & 0 & 0 \\ gA + dB - bD & aA + bB + dD & gA + dB - bD & 0 & 0 & 0 \\ gA + dB - bD & gA + dB - bD & aA + bB + dD & 0 & 0 & 0 \\ 0 & 0 & 0 & g(A-B) + aD & 0 & 0 \\ 0 & 0 & 0 & 0 & g(A-B) + aD & 0 \\ 0 & 0 & 0 & 0 & 0 & g(A-B) + aD \end{bmatrix} \quad (7.9)$$

where,  $A = 2C_{11} + C_{22}$ ;  $B = 2C_{12} + C_{13}$ ;  $D = 2G_{12} + G_{13}$  and  $a, b, d, g$  are integration constants.

(3) The homogenized EPON 862 properties using the orientation average above were incorporated in a 2x2 RUC model in GMC as depicted in Fig. 7.6 where one subcell was used to model the fiber, and the remaining three subcells were used to model the matrix. Table 7.1 shows the constitutive models used at the GMC level. Damage initiation at the micro scale was modeled using a maximum stress failure criterion for the matrix subcell, and a maximum strain failure criterion for the fiber subcell (failure at a strain of .015). The maximum stress estimates for the matrix subcell are directly obtained from the critical stress at the initiation of damage as predicted by the NIDM based MD simulations in [138]. A subcell was assumed to lose its load carrying capacity at the onset of damage. Table 7.2 shows the stress base failure criterion for the baseline and reinforced matrix used.

**Table 7.1** RUC level properties of subcells

<b>Subcell component</b>	<b><math>E_A</math> (GPa)</b>	<b><math>E_T</math> (GPa)</b>	<b><math>\nu_A</math></b>	<b><math>\nu_T</math></b>	<b><math>G_A</math> (GPa)</b>	<b><math>\alpha_A</math> (<math>10^{-6}/^\circ\text{C}</math>)</b>	<b><math>\alpha_T</math> (<math>10^{-6}/^\circ\text{C}</math>)</b>
<b>Matrix (baseline)</b>	2.96	2.96	0.33	0.33	1.35	45	45
<b>Reinforced matrix</b>	3.59	3.59	0.36	0.36	1.5	45	45
<b>IM7 fiber</b>	276	7.6	0.33	0.33	14.9	-0.64	9.74

(4) An OHT specimen undergoing tensile loading was modeled in the Abaqus finite element software as depicted in Fig. 7.6, and was iteratively coupled with GMC to model the microscale RUC. The iterative coupling was not extended to the nanoscale in the interest of computational efficiency. In addition to evolving damage within the RUC, a cohesive damage model available in Abaqus was employed to model macro-scale interlaminar delamination

**Table 7.2** Stress based failure criterion for baseline and reinforced matrices

<b>Subcell component</b>	<b><math>\sigma_{11}</math>(MPa)</b>	<b><math>\sigma_{22}</math>(MPa)</b>
<b>Matrix(baseline)</b>	105.79	45.97
<b>Reinforced matrix</b>	121.02	56.755

occurring outside the micro scale RUC. Fig. 7.8(a) shows the load displacement plot for the OHT simulation under uniaxial tensile loading at room temperature. Four cases were studied, baseline matrix with and without delamination modeling and reinforced matrix with and without delamination modeling, to observe its influence on the predicted failure load. Fig. 7.8(b) is a

magnified view of Fig. 7.8(a) at the load drop, in order to provide a clearer view of the effects of nanographene and delamination on predicted peak load. As is evident from Fig. 7.8, the hierarchical multiscale model is able to capture small change in stiffness and failure strength (Fig. 7.8(b)), due to the presence of nano graphene. It is also evident that while the influence of nanographene platelets is somewhat significant in increasing the OHT strength of the composite, the inclusion of cohesive layers to model inter-ply delamination is not as significant for this case. Fig. 7.9 shows the evolution of von-Mises stress contours with applied strain in each individual lamina until maximum load is reached. Based on Figs. 7.8 and 7.9, the specimen failure is catastrophic, and occurs due to the failure of the load bearing fibers in the  $0^\circ$  layer once the failure strain is reached. For this simple case, the hierarchical multi-scale model predicts a 3.7% increase in OHT strength over baseline case with the addition of 2.4 wt% of NGP (with platelet  $AR = 2$ ) if delamination was not modeled using cohesive elements between lamina. The same model predicts a 4.1% increase in OHT strength over baseline case with the addition of NGP (with platelet  $AR = 2$ ) if delamination was modeled using cohesive elements between lamina. Hence, the three-level multiscale model predicts a slight increase in OHT strength of the laminate due to the presence of 2.4 wt% of NGP in EPON 862 matrix. It should be noted that the unrealistic average aspect ratio of 2 for the NGP was selected in order to keep the number of atoms in the MD simulations tractable. Also, the multiscale failure predictions in Figs. 7.8 and 7.9 have not been verified using actual OHT experiments.

The analysis presented in this chapter is a conceptual demonstration of the capabilities of multiscale modeling, but it is by no means an exhaustive study of all its feasibilities. Suffice it to say that multiscale modeling, whether it is hierarchical, concurrent, or a hybrid combination of these techniques, will continue to play a key role in progressive failure modeling of composite

materials for the foreseeable future, and that it has the potential to perform high fidelity *numerical experiments* thereby eliminating the need for costly trial-and-error approach to materials development and certification.

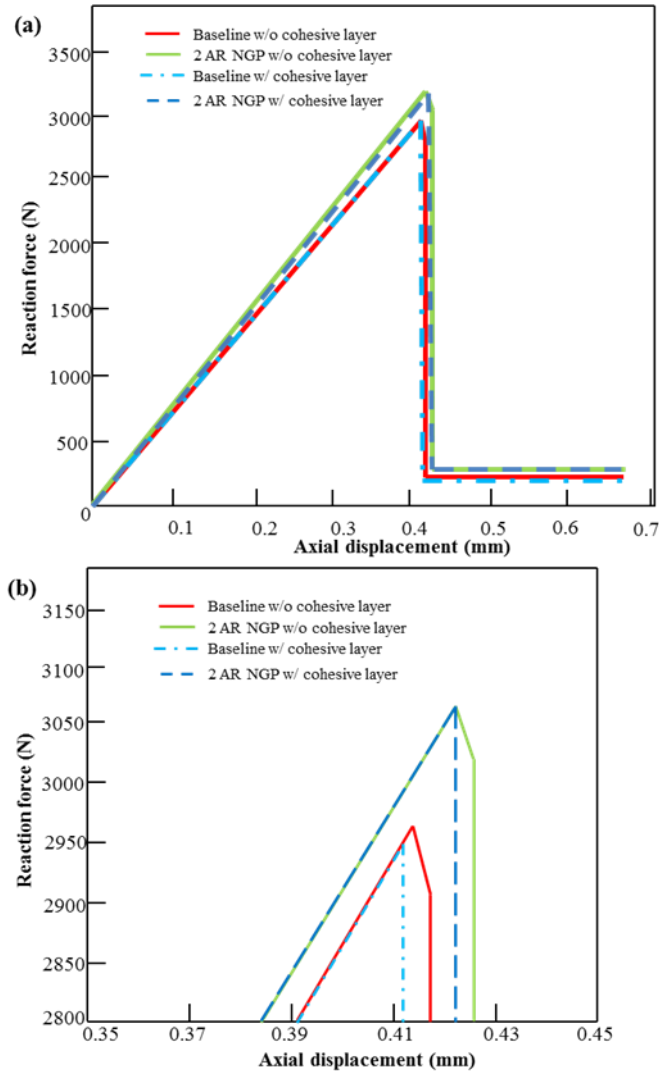


**Figure 7.8 (a)** Load displacement plot for multiscale OHT simulation for various cases **(b)** Magnified view at load drop

To achieve these objectives, some of the key issues that still need to be addressed are: (a) implementation of fully nonlinear material modeling capabilities in GMC so that damage initiation as well as damage evolution in each micro-scale subcell can be handled, (b)

implementation of probabilistic materials data input within the multi-scale modeling framework to incorporate variability in material properties as well as manufacturing defects all the way from macro-scale to the atomistic level, and (c) the computational time required to solve coupled three-level hierarchical multiscale problems is still very intensive and needs to be reduced through better implementation of massively parallel (cloud) computing.

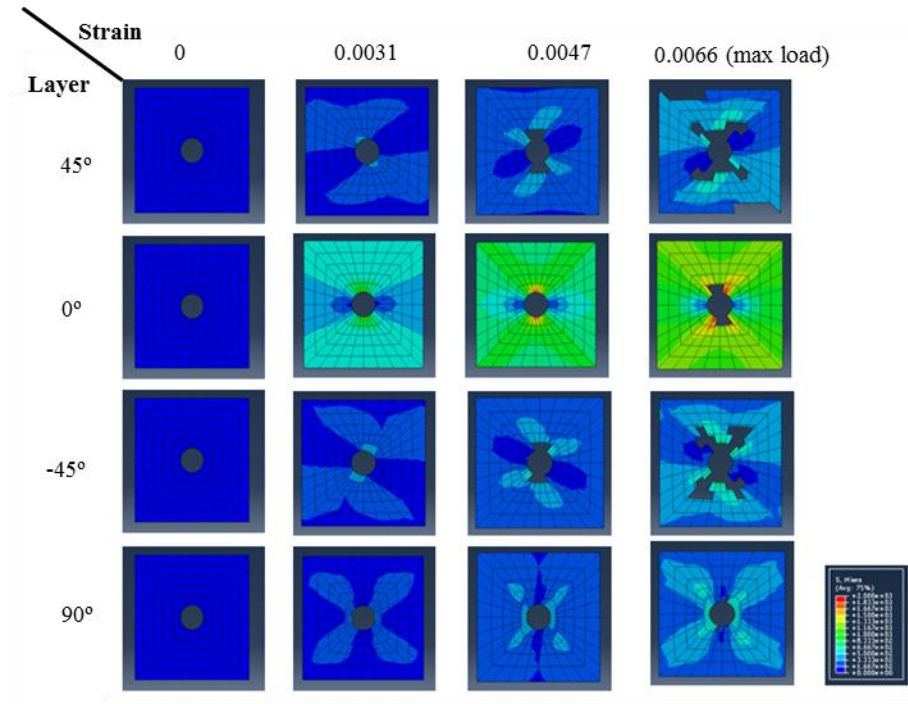


**Figure 7.9** von Mises stress contour for individual lamina in IM7/EPON 862 OHT simulation

## CHAPTER 8

### SUMMARY AND FUTURE WORK

This dissertation presents an extensive study of NGP reinforced EPON 862 thermoset epoxy polymer, from both experimental and modeling perspectives. The research presented herein ranges from moisture (barrier) properties of NGP reinforced polymers, to the influence of NGPs on the fracture properties of polymers and carbon fiber composites, in Mode I and mixed mode. Nanocomposite processing issues addressed include the dispersion of NGPs in an epoxy using hydrogen passivation, and tailoring of toughness in NGP composites by aligning the conductive graphene platelets to provide optimum fracture toughness.

Chapter 2 presents detailed experimental evidence of change in barrier properties of EPON 862 polymer when NGPs are added to this system. The saturation moisture uptake is reduced for NGP- reinforced polymers for very low wt% of NGP added to the system. Anomalous moisture absorption curves were observed for all cases, which were accurately modeled using a novel viscoelastic diffusion model.

Chapter 3 shows dramatic changes in Mode I fracture properties of NGP reinforced polymers at very low wt%. For only 0.5 wt% of NGP, an increase of 570% in fracture energy was observed. It was evident that presence of NGPs can influence the behavior of polymer matrices for better performance in fracture. The chapter also shows changes in the fracture properties due to hygrothermal aging of the specimens. An increase in fracture properties was observed after hygrothermal aging of the specimens, on account of matrix plasticization due to moisture ingress.

Chapter 4 studies nanocomposite processing using hydrogen passivation of NGPs to improve dispersion of platelets in the epoxy. Hydrogen passivation shows tremendous potential for dispersing NGPs in epoxy using ultrasonication. Optical microscopy and TEM results show positive results for improved dispersion of NGPs in ethanol and EPON 862.

Chapter 5 shows the use of HP-NGPs to study the mixed mode fracture behavior of NGP reinforced polymers. An increase of 158% in  $K_{IIC}$  was observed for a pure Mode II case for only 0.5 wt% of NGP in the polymer. Fracture envelope presented in this chapter sheds light on the overall reinforcing effect of NGPs in the epoxy matrix across various mode mixities. The chapter also shows DCB test results for EPON 862/IM7 carbon fiber laminates with the EPON 862 reinforced with HP-NGP. NGPs show remarkable potential to be used in composite structures in this context, since only 0.5 wt% of NGP in the matrix improves the initiation fracture toughness of the laminates by 48%. The crack-growth resistance behavior of the NGP reinforced specimens shows even greater improvement than the unreinforced specimens, because 0.5wt% NGP causes an increase in resistance to the crack growth by more than 100%.

Nanoscale toughness enhancement mechanisms due to the presence of NGPs in the epoxy are presented in Chapter 6. The chapter presents a theory for mode switch from brittle fracture to damage and aims to predict the orientation, length scale and the amount of NGP required for having significant effect on the fracture properties of epoxies. The orientation control of NGP in the epoxy is sought as an important factor in this chapter. Alignment studies using different electrodes, electric field intensities and frequencies are presented. These studies will form a basis for producing high quality aligned NGP polymer composites in the future.

Chapter 7 introduces the concept of multiscale modeling using a hierarchical approach starting from MD (nano) to GMC (micro) to Abaqus (macro). A case study is presented which shows

changes in the OHT strength of laminates when reinforced with NGPs modeled from MD and incorporated in GMC.

Future work entails fatigue characterization of NGP reinforced composites for fatigue crack propagation. The methodology proposed in Chapter 6 for alignment of NGPs in a polymer can be employed to produce aligned NGP specimens which can be used for both electrical and structural applications. Better multiscale failure models need to be implemented at the GMC scale for accurate prediction of local stresses and strains.

## REFERENCES

- [1] Boeing Incorporation Archive, Aero Magazine, A Quarterly Publication, Quarter 04, Issue 24. [http://www.boeing.com/commercial/aeromagazine/articles/qtr\\_4\\_06/article\\_04\\_2.html](http://www.boeing.com/commercial/aeromagazine/articles/qtr_4_06/article_04_2.html), 2006 (accessed 06.28.16).
- [2] Airbus XWB 350, Innovation. <http://www.a350xwb.com/innovation/>, 2016 (accessed 06.28.2016).
- [3] BMW USA, Carbon fiber reinforced performance. <http://www.bmwusa.com/bmw/bmwi>, 2015 (accessed 06.28.2016).
- [4] M. Moffat, Braving New Worlds: To Conquer, to Endure, J. Am. Phys. Ther. Assoc. 84 (2004) 1056-1086.
- [5] A.S. Argon, R.E. Cohen, Toughenability of polymers, Polymer 44 (2003) 6013–6032.
- [6] R.A. Pearson, A.Y. Yee, Toughening mechanisms in elastomer-modified epoxies: Part 3 The effect of cross-link density, J. Mater. Sci. 24 (1989) 2571-2580.
- [7] A.C. Garg, Y.W. Mai, Failure Mechanisms in toughened epoxy resins - A review, Compos. Sci. Technol. 31(3) (1988) 179–223.
- [8] N. Domun, H. Hadavinia, T. Zhang, T. Sainsbury, G.H. Liaghata, S. Vahida, Improving the fracture toughness and the strength of epoxy using nanomaterials – a review of the current status, Nanoscale 7 (2015) 10294–10329.
- [9] D.R. Tenney, J.G. Davis, R.B. Pipes, N. Johnston, NASA Composite Materials Development: Lessons Learned and Future Challenges, NATO RTO AVT-164 Workshop on Support of Composite Systems (2009) 58 pages.
- [10] R.A. Pearson, A.Y. Yee, Toughening mechanisms in thermoplastic-modified epoxies: 1. Modification using poly(phenylene oxide), Polymer 34(17) (1993) 3658-3670.
- [11] G. Ragosta, M. Abbate, P. Musto, G. Scarinzi, L. Mascia, Epoxy-silica particulate nanocomposites: Chemical interactions, reinforcement and fracture toughness, Polymer 46 (2005) 10506–10516.

- [12] Q. Wang, X.H. Han, A. Sommers, Y. Park, C. T'Joel, A. Jacobi, A review on application of carbonaceous materials and carbon matrix composites for heat exchangers and heat sinks, *Int. J. Refrig.* 35 (2012) 7-26.
- [13] H. Liu, L. C. Brinson, Reinforcing efficiency of nanoparticles: A simple comparison for polymer nanocomposites, *Compos. Sci. Technol.* 68 (2008) 1502-1512.
- [14] B.S.R. Reddy, *Advances in Diverse Industrial Applications of Nanocomposites*, InTech, Croatia, 2011
- [15] S. H. Lee, E. N. R. Cho, S. H. Jeon, J. R. Youn, Rheological and electrical properties of polypropylene composites containing functionalized multi-walled carbon nanotubes and compatibilizers, *Carbon* 45(14) (2007) 2810-2822.
- [16] V. Vahedi, P. Pasbakhsh, S-P Chai, Toward high performance epoxy/halloysite nanocomposites: New insights based on rheological, curing and impact properties, *Materials & Design*, 48 (2015) 42–53.
- [17] H. Hu, X. Wang, J. Wang, L. Wan, F. Liu, H. Zheng, R. Chen, C. Xu, Preparation and properties of graphene nanosheets–polystyrene nanocomposites via in situ emulsion polymerization, *Chem. Phys. Lett.* 484 (2010) 247–253.
- [18] Y.F. Zhao, M. Xiao, S.J. Wang, X.C. Ge, Y.Z. Meng, Preparation and properties of electrically conductive PPS/expanded graphite nanocomposites, *Compos. Sci. Technol.* 67 (2007) 2528–2534.
- [19] G. Eda, M. Chhowalla, Graphene-based Composite Thin Films for Electronics, *Nano Letters* 9 (2009) 814–818.
- [20] C. Bao, L. Song, W. Xing, B. Yuan, C.A. Wilkie, J. Huang, Y. Guo, Y. Hu, Preparation of graphene by pressurized oxidation and multiplex reduction and its polymer nanocomposites by masterbatch-based melt blending, *J. Mater. Chem.* 22 (2012) 6088-6096.
- [21] Z. Jin, K. Pramoda, G. Xu, S.H. Goh, Dynamic mechanical behavior of melt-processed multi-walled carbon nanotube/poly(methyl methacrylate) composites, *Chem. Phys. Lett.* 337(1–3) (2001) 43–47.
- [22] R.E. Gorga, R.E. Cohen, Toughness enhancements in poly(methyl methacrylate) by addition of oriented multiwall carbon nanotubes”, *J. Polym. Sci. B Polym. Phys.* 42(14) (2004) 2690–2702.
- [23] B. Shen, W. Zhai, C. Chen, D. Lu, J. Wang, W. Zheng, Melt Blending In situ Enhances the Interaction between Polystyrene and Graphene through  $\pi$ - $\pi$  Stacking, *ACS Appl. Mater. Interfaces* 3 (2011) 3103–3109.

- [24] K. Mukhopadhyay, C.D. Dwivedi, G.N. Mathur, Conversion of carbon nanotubes to carbon nanofibers by sonication, *Carbon* 40(8) (2002) 1373–1376.
- [25] F.H. Gojny, M.H. Wichmann, B. Fiedler, K. Schulte, Influence of different carbon nanotubes on the mechanical properties of epoxy matrix composites – A comparative study, *Compos. Sci. Technol.* 65 (2005) 2300–2313.
- [26] M.S.P Shaffer, A.H. Windle, Fabrication and Characterization of Carbon Nanotube/Poly (vinyl alcohol) Composites, *Adv. Mater.* 11(11) (1999) 937-941.
- [27] J. Jang, J. Bae, S-H Yoon, A study on the effect of surface treatment of carbon nanotubes for liquid crystalline epoxide–carbon nanotube composites, *J. Mater. Chem.* 13 (2003) 676-681.
- [28] U. Khan, P. May, A. O’Neill, J.N. Coleman, Development of stiff, strong, yet tough composites by the addition of solvent exfoliated graphene to polyurethane, *Carbon* 48 (2010) 4035-4041.
- [29] R. Verdejo, M.M. Bernal, L.J. Romasanta, M.A.L. Manchado, Graphene filled polymer nanocomposites, *J. Mater. Chem.* 21 (2011) 3301-3310.
- [30] M.R. Loos, L.A.F. Coelho, S.H. Pezzin, S.C. Amico, The effect of acetone addition on the properties of epoxy, *Polímeros, Ciência e Tecnologia* 18 (1) (2008) 76-80.
- [31] A. Kumar, S. Li, S. Roy, J.A. King, G.M. Odegard, Fracture properties of nanographene reinforced EPON 862 thermoset polymer system, *Compos. Sci. Technol.* 144 (2015) 87-93.
- [32] M. Trujillo, M.L. Arnal, A.J. Müller, E. Laredo, S. Bredeau, D. Bonduel, P. Dubois, Thermal and Morphological Characterization of Nanocomposites Prepared by in-Situ Polymerization of High-Density Polyethylene on Carbon Nanotubes, *Macromolecules* 40 (2007) 6268–6276.
- [33] S.M. Kwon, H.S. Kim, S.J. Myung, H.J. Jin, Poly(methyl methacrylate)/multiwalled carbon nanotube microspheres fabricated via in-situ polymerization, *J. Polym. Sci. B Polym. Phys.* 46 (2008) 182–189.
- [34] W.H. Song, Q.P. Ni, Z. Zheng, L.Y. Tian, X.L. Wang, The preparation of biodegradable polyurethane/carbon nanotube composite based on in situ cross-linking, *Polym. Adv. Technol.*, 20 (2009) 327–331.
- [35] B. Chen, J.R.G. Evans, Elastic moduli of clay platelets, *Scr. Mater.* 54 (2006) 1581-1585.
- [36] Y. Kojima, A. Usuki, M. Kawasumi, A. Okada, Y. Fukushima, T. Kurauchi, O. Kamigaito, Mechanical properties of nylon 6-clay hybrid, *J. Mater. Res.* 8(5) (1993) 1185-1189.
- [37] T. Pinnavaia, G. Beall, *Polymer-Clay Nanocomposites*, Wiley, New York, 2000.

- [38] E.P. Giannelis, Polymer Layered Silicate Nanocomposites”, *Adv. Mater.* 8(1) (1996) 29-35.
- [39] T.D. Fornes, P.J. Yoon, H. Keskkula, D.R. Paul, Nylon 6 nanocomposites: the effect of matrix molecular weight, *Polymer* 42 (2001) 9929-9940.
- [40] A.J. Blumstein, Polymerization of adsorbed monolayers. II. Thermal degradation of the inserted polymer, *J. Polym. Sci. A Polym. Chem.* 3(7) (1965) 2665-2672.
- [41] M-L Chan, K-T Lau, T-T Wong, M.P. Ho, D. Hui, Mechanism of reinforcement in a nanoclay/polymer composite, *Composites Part B* 42 (2011) 1708–1712.
- [42] S.R. Ha, K.Y. Rhee, Effect of surface modification of clay using 3-amino propyl triethoxysilane on the wear behavior of clay/epoxy nanocomposites, *Colloids Surf. A Physicochem. Eng. Asp.* 322 (2008) 1–5.
- [43] T. Lan, T.J. Pinnavaia, Clay-Reinforced Epoxy Nanocomposites, *Chem. Mater.* 6 (1994) 2216-2219.
- [44] J-C Lin, Compression and wear behavior of composites filled with various nanoparticles, *Composites Part B* 38 (2007) 79–85.
- [45] M. Bashar, P. Mertiny, U. Sundararaj, Effect of Nanocomposite Structures on Fracture Behavior of Epoxy-Clay Nanocomposites Prepared by Different Dispersion Methods, *J. Nanomater.* 312813 (2014) 12 pages.
- [46] B. Qi, Q.X. Zhang, M. Bannister, Y-W Mai, Investigation of the mechanical properties of DGEBA-based epoxy resin with nanoclay additives, *Compos. Struct.* 75 (2006) 514–519.
- [47] O. Becker, R. Varley, G. Simon, Morphology, thermal relaxations and mechanical properties of layered silicate nanocomposites based upon high-functionality epoxy resins, *Polymer* 43 (2002) 4365–4373.
- [48] L. Wang, K. Wang, L. Chen, Y. Zhang, C. He, Preparation, morphology and thermal/mechanical properties of epoxy/ nanoclay composite, *Composites Part A* 37 (2006) 1890–1896.
- [49] E.T. Thostenson, W.Z. Li, D.Z. Wang, Z.F. Ren, T.W. Chou, Carbon nanotube/carbon fiber hybrid multiscale composites, *J. Appl. Phys.* 91(9) (2002) 6034-6037.
- [50] T.W. Ebbesen, P.M. Ajayan, Large-scale synthesis of carbon nanotubes, *Nature* 358 (1992) 220–222.
- [51] A. Thess, R. Lee, P. Nikolaev, H. Dai, P. Petit, J. Robert, C. Xu, Y. H. Lee, S.G. Kim, A.G. Rinzler, D.T. Colbert, G.E. Scuseria, D. Tománek, J.E. Fischer, R.E. Smalley, Crystalline ropes of metallic carbon nanotubes, *Science* 273 (1996) 483–487.

- [52] A. Oberlin, M. Endo, S. Koyama, Filamentous growth of carbon through benzene decomposition, *J. Cryst. Growth* 32 (1976) 335–349.
- [53] J.M. Tan, P. Arulselvan, S. Fakurazi, H. Ithnin, M.Z. Hussein, A Review on Characterizations and Biocompatibility of Functionalized Carbon Nanotubes in Drug Delivery Design, *J. Nanomater.* 917024 (2014) 20 pages.
- [54] L. Sun, G.L. Warren, J.Y. O'Reilly, W.N. Everett, S.M. Lee, D. Davis, D. Lagoudas, H.J. Sue, Mechanical properties of surface-functionalized SWCNT/epoxy composites, *Carbon* 46 (2008) 320–328.
- [55] T.H. Hsieh, A.J. Kinloch, A.C. Taylor, I. Kinloch, The effect of carbon nanotubes on the fracture toughness and fatigue performance of a thermosetting epoxy polymer, *Mater. Sci.* 46 (2011) 7525–7535.
- [56] L-C Tang, Y-J Wan, K. Peng, Y-B Pei, L-B Wu, L-M Chen, L-J Shu, J-X Jiang, G-Q Lai, Fracture toughness and electrical conductivity of epoxy composites filled with carbon nanotubes and spherical particles, *Composites Part A* 45 (2013) 95–101.
- [57] F.H. Gojny, M.H. Wichmann, U. Kopke, B. Fiedler, K. Schulte, Carbon nanotube-reinforced epoxy-composites: enhanced stiffness and fracture toughness at low nanotube content, *Compos. Sci. Technol.* 64 (2004) 2361–2371.
- [58] H.A. Perez, F. Aviles, M.A. Pat, V.A. Gonzalez, H.P. Franco, B.P. Perez, Effective properties of multiwalled carbon nanotube/epoxy composites using two different tubes, *Compos. Sci. Technol.* 68 (2008) 1422–1431.
- [59] F.H. Gojny, M.H. Wichmann, B. Fiedler, K. Schulte, Influence of different carbon nanotubes on the mechanical properties of epoxy matrix composites – A comparative study, *Compos. Sci. Technol.* 65 (2005) 2300–2313.
- [60] A. Hirsch, Functionalization of Single-Walled Carbon Nanotubes, *Angew. Chem. Int. Ed.*, 41(11) (2002), 1853–1859.
- [61] K. Balasubramanian, M. Burghard, Chemically Functionalized Carbon Nanotubes, *Small*, 1(2) (2005) 180–192.
- [62] R. Sattar, A. Kausar, M. Siddiq, Advances in thermoplastic polyurethane composites reinforced with carbon nanotubes and carbon nanofibers: A review, *J. Plast. Film Sheeting* 1 (2014) 1–40.
- [63] L. Liu, A.H. Barber, S. Nuriel, H. D. Wagner, Mechanical Properties of Functionalized Single-Walled Carbon-Nanotube/Poly(vinyl alcohol) nanocomposites, *Adv. Funct. Mater.* 15 (2005) 975-980.

- [64] H.Z. Geng, R. Rosen, B. Zheng, H. Shimoda, L. Fleming, J. Liu, O. Zhou, Fabrication and Properties of Composites of Poly(ethylene oxide) and Functionalized Carbon Nanotubes, *Adv. Mater.* 14 (2002),1387-1390.
- [65] J. Zhu, J. Kim, H. Peng, J.L. Margrave, V.N. Khabashesku, E.V. Barrera, Improving the Dispersion and Integration of Single-Walled Carbon Nanotubes in Epoxy Composites through Functionalization, *Nano Lett.* 3(8) (2003) 1107–1113.
- [66] Y. Geng, M.Y. Liu, J. Li, X.M. Shi, J.K. Kim, Effects of surfactant treatment on mechanical and electrical properties of CNT/epoxy nanocomposites, *Composites Part A* 39 (2008) 1876–1883.
- [67] P.C. Ma, J-K Kim, B.Z. Tang, Effects of silane functionalization on the properties of carbon nanotube/epoxy nanocomposites, *Compos. Sci. Technol.* 67 (2007) 2965–2972.
- [68] L-C Tang, H. Zhang, J-H Han, X.P. Wu, Z. Zhang, Fracture mechanisms of epoxy filled with ozone functionalized multi-wall carbon nanotubes, *Compos. Sci. Technol.* 72 (2011) 7–13.
- [69] E. Bekyarova, E.T. Thostenson, A. Yu, H. Kim, J. Gao, J. Tang, H.T. Hahn, T-W Chou, M.E. Itkis, R.C. Haddon, Multiscale Carbon Nanotube-Carbon Fiber Reinforcement for Advanced Epoxy Composites, *Langmuir* 23 (2007) 3970-3974.
- [70] A.Y. Boroujeni, M. Tehrani, A.J. Nelson, M. Al-Haik, Hybrid carbon nanotube–carbon fiber composites with improved in-plane mechanical properties, *Composites Part B* 66 (2014) 475–483.
- [71] V.P. Veedu, A. Cao, X. Li, K. Ma, C. Soldano, S. Kar, P. Ajayan, M.N. Ghasemi-Nejhad, Multifunctional composites using reinforced laminae with carbon-nanotube forests, *Nature Materials* 5 (2006) 457-462.
- [72] The University of Manchester, Home of Graphene, Explore, What can Graphene Do. <http://www.graphene.manchester.ac.uk/explore/what-can-graphene-do/>, (2016) (accessed on 06.29.2016).
- [73] J. Zhu, D. Yang, Z. Yin, Q. Yan, H. Zhang, Graphene and Graphene-Based Materials for Energy Storage Applications, *Small* 10(17) (2014) 3480–3498.
- [74] F-N Xiao, M. Wang, F-B Wang, X-H Xia, Graphene–Ruthenium (II) Complex Composites for Sensitive ECL Immunosensors, *Small*, 10(4) (2014) 706–716.
- [75] C-C Teng, C.C.M. Ma, C-H Lu, S-Y Yang, S.H. Lee, M-C Hsiao, M-Y Yen, K-C Chiou, T-M Lee, Thermal conductivity and structure of non-covalent functionalized graphene/epoxy composites, *Carbon* 49(15) (2011) 5107-5116.

- [76] J. Wang, H. Hu, X. Wang, C. Xu, M. Zhang, X. Shang, Preparation and mechanical and electrical properties of graphene nanosheets–poly(methyl methacrylate) nanocomposites via in situ suspension polymerization, *J. Appl. Polym. Sci.* 122 (2011) 1866-1871.
- [77] X. Zhao, Q. Zhang, D. Chen, P. Lu, Enhanced Mechanical Properties of Graphene-Based Poly (vinyl alcohol) Composites, *Macromolecules* 43 (2010) 2357-2363.
- [78] M. Koo, J-S Bae, S.E. Shim, D. Kim, D.G. Nam, J.W. Lee, G.W. Lee, J.H. Yeum, W. Oh, Thermo-dependent characteristics of polyimide–graphene composites, *Colloid Polym. Sci.* 289 (13) (2011) 1503-1509.
- [79] I.P. Blanco, C.E. Hoppe, M.A.L. Quintela, J. Rivas, Control on the dispersion of gold nanoparticles in an epoxy network, *J. Non-Cryst. Solids* 353 (2007) 826-828.
- [80] G. Subramanian, M.J. Andrews, Preparation of SWNT-reinforced composites by a continuous mixing process, *Nanotechnology*, 16 (6) (2005) 836-840.
- [81] Z. Spitalsky, D. Tasis, K. Papagelis, C. Galiotis, Carbon nanotube–polymer composites: Chemistry, processing, mechanical and electrical properties, *Prog. Polym. Sci.* 35 (3) (2010) 357-401.
- [82] J. Suhr, W. Zhang, P.M. Ajayan, N.A. Koratkar, Temperature-activated interfacial friction damping in carbon nanotube polymer composites, *Nano Lett.* 6 (2006) 219-223.
- [83] Z.C. Tu, Z.C. Ou-yang, Single-walled and multiwalled carbon nanotubes viewed as elastic tubes with the effective Young's moduli dependent on layer number, *Phys. Rev. B* 65 (2002) 233407 1-4.
- [84] C.A. Cooper, D. Ravich, D. Lips, J. Mayer, H.D. Wagner, Distribution and alignment of carbon nanotubes and nanofibrils in a polymer matrix, *Compos. Sci. Technol.* 62 (2002) 1105-1112.
- [85] U.K. Sur, Graphene: A Rising Star on the Horizon of Materials Science, *Int. J. Electrochem.* (2012) 237689 12 pages.
- [86] M. Alexandre, P. Dubois, Polymer-layered silicate nanocomposites: preparation, properties and uses of a new class of materials, *Mater. Sci. Eng. R* 28 (1-2) (2000) 1-63.
- [87] A. Yu, P. Ramesh, M.E. Itkis, E. Bekyarova, R.C. Haddon, Graphite Nanoplatelet–Epoxy Composite Thermal Interface Materials, *J. Phys. Chem. C*, 111 (21) (2007) 7565-7569.
- [88] J. Yu, P. Jiang, C. Wu, L. Wang, X. Wu, Graphene nanocomposites based on poly(vinylidene fluoride): Structure and properties, *Polym. Compos.* 32 (10) (2011) 1483-1491.
- [89] T. Ramanathan, A.A. Abdala, S. Stankovich, D.A. Dikin, M. Herrera-Alonso, R.D. Piner, D.H. Adamson, H.C. Schniepp, X. Chen, R.S. Ruoff, S.T. Nguyen, I.A. Aksay, R.K.

Prud'Homme, L.C. Brinson, Functionalized graphene sheets for polymer nanocomposites, *Nat. Nanotechnol.* 3 (2008) 327-331.

[90] J.A. King, D.R. Klimek, I. Miskioglu, G.M. Odegard, Mechanical properties of graphene nanoplatelet/epoxy composites, *J. Appl. Polym. Sci.* 128 (6) (2012) 4217–4223.

[91] X. Zhou, T. Wu, K. Ding, B. Hu, M. Hou, B. Han, Dispersion of graphene sheets in ionic liquid [bmim][PF6] stabilized by an ionic liquid polymer, *Chem. Commun.* 46 (2010) 386–388.

[92] A.J. Patil, J.L. Vickery, T.B. Scott, S. Mann, Aqueous Stabilization and Self-Assembly of Graphene Sheets into Layered Bio-Nanocomposites using DNA, *Adv. Mater.* 21 (2009) 3159–3164.

[93] D.W. Boukhvalov, M.I. Katsnelson, Chemical Functionalization of Graphene with Defects, *Nano Lett.* 8 (12) (2008) 4373–4379.

[94] H. Kim, S. Kobayashi, M.A. AbdurRahim, M.J. Zhang, A. Khusainova, M.A. Hillmyer, A.A. Abdala, C.W. Macosko, Graphene/polyethylene nanocomposites: Effect of polyethylene functionalization and blending methods, *Polymer* 52 (8) (2011) 1837-1846.

[95] M.A. Rafiee, J. Rafiee, I. Srivastava, Z. Wang, H. Song, Z-Z Yu, N. Koratkar, Fracture and Fatigue in Graphene Nanocomposites, *Small* 6 (2) (2010) 179-183.

[96] M.A. Rafiee, J. Rafiee, I. Srivastava, Z. Wang, H. Song, Z-Z Yu, N. Koratkar, Enhanced Mechanical Properties of Nanocomposites at Low Graphene Content, *ACS Nano* 3 (12) (2009) 3884-3890.

[97] Y. Yang, W. Rigdon, X. Huang, X. Li, Enhancing graphene reinforcing potential in composites by hydrogen passivation induced dispersion, *Nature Scientific Reports* 3 (2013) 2086.

[98] H. Kim, A.A. Abdala, C.W. Macosko, Graphene/Polymer Nanocomposites, *Macromolecules* 43 (2010) 6515–6530.

[99] A.S. Wajid, H.S.T. Ahmed, S. Das, F. Irin, A.F. Jankowski, M.J. Green, High- Performance Pristine Graphene/Epoxy Composites With Enhanced Mechanical and Electrical Properties, *Macromol. Mater. Eng.* 298 (2013) 339–347.

[100] J. Du, H.M. Cheng, The Fabrication, Properties, and Uses of Graphene/Polymer Composites, *Macromol. Chem. Phys.* 213 (2012) 1060–1077.

[101] X. Sun, H. Sun, H. Li, H. Peng, Developing Polymer Composite Materials: Carbon Nanotubes or Graphene, *Adv. Mater.* 25 (2013) 5153–5176.

[102] V. Mittal, Functional Polymer Nanocomposites with Graphene: A Review, *Macromol. Mater. Eng.* 299 (2014) 906–931.

- [103] M.M. Shokrieh, S.M. Ghoreishi, M. Esmkhani, Z. Zhao, Effects of graphene nanoplatelets and graphene nanosheets on fracture toughness of epoxy nanocomposites, *Fatigue Fract. Eng. M.* 37 (2014) 1116–1123.
- [104] J.J. Liang, Y. Huang, L. Zhang, Y. Wang, Y.F. Ma, T.Y. Guo, Y.S. Chen, Molecular-Level Dispersion of Graphene into Poly(vinyl alcohol) and Effective Reinforcement of their Nanocomposites, *Adv. Funct. Mater.* 19 (2009) 2297-2302.
- [105] D.R. Bortz, E.G. Heras, I. Martin-Gullon, Impressive Fatigue Life and Fracture Toughness Improvements in Graphene Oxide/Epoxy Composites, *Macromolecules* 45 (2012) 238–245.
- [106] S. Roy, W. Xu, S.J. Park, K.M. Liechti, Anomalous Moisture Diffusion in Viscoelastic Polymers: Modeling and Testing, *Journal of Applied Mechanics* 67 (2) (1999) 391-396.
- [107] L.W. Cai, Y. Weitsmann, Non-Fickian Moisture Diffusion in Polymeric Composites, *J. Compos. Mater.* 28 (2) (1994) 130-154.
- [108] H.L. Frisch, Isothermal Diffusion in Systems with Glasslike Transitions, *J. Chem. Phys.* 41 (12) (1964) 3379-3683.
- [109] J. Crank, *The Mathematics of Diffusion*, second ed., Oxford University Press, Oxford, 1975.
- [110] L-C Tang, Y-J Wan, D. Yan, Y-B Pei, L. Zhao, Y-B Li, L-B Wu, J-X Jiang, G-Q Lai, The effect of graphene dispersion on the mechanical properties of graphene/epoxy composites, *Carbon* 60 (2013) 6-27.
- [111] W. Liu, S.V. Hoa, M. Pugh, Water uptake of epoxy–clay nanocomposites: Model development, *Compos. Sci. Technol.* 68 (2008) 156-163.
- [112] A. Kumar, S. Roy, Modeling of anomalous moisture diffusion in nanographene reinforced thermoset polymers, *Compos. Struct.* 122 (2015) 1–7.
- [113] American Society for Testing and Materials, Standard Test Method for Water Absorption of Plastics, ASTM D570-98 e1 (2010).
- [114] J.A. King, D.R. Klimek, I. Miskioglu, G.M. Odegard, Mechanical properties of graphene nanoplatelet/epoxy composites, *J. Appl. Polym. Sci.* 128 (2013) 4217–4223.
- [115] H.S. Carslaw, J.C. Jaeger, *Conduction of heat in solids*, second ed., Oxford University Press, Oxford, 1959.
- [116] J.C. Lagarias, J.A. Reeds, M.H. Wright, P.E. Wright, Convergence Properties of the Nelder-Mead Simplex Method in Low Dimensions, *Siam J. Optim.* 9 (1) (1998) 112-147.

- [117] XG Sciences Incorporation, XG Sciences Company and Materials Overview. <http://xgsciences.com/wp-content/uploads/2012/11/XGS-Company-and-Materials-Overview-Q4-2012.pdf>, 2012 (accessed on 06.28.13).
- [118] S. Roy, K. Narasimhan, Characterization and Modelling of Hygrothermal Effects in Thermoplastic Nanocomposites, *Polym. Polym. Compos.* 19 (7) (2011) 527-541.
- [119] Miller Stephenson Incorporation, Technical Data Sheet, Epoxy Resins. <http://www.miller-stephenson.com/miller/pdf/Resins%20Epirez.pdf>, 2012 (accessed on 08.08.14).
- [120] American Society for Testing and Materials, Standard Test Methods for Plane-Strain Fracture Toughness and Strain Energy Release Rate of Plastic Materials, ASTM 5045-14 (2014).
- [121] K.T. Faber, A.G. Evans, Crack Deflection Processes-I. Theory, *Acta Metall.* 31 (4) (1983) 565-576.
- [122] C. Park, J. Wilkinson, S. Banda, Z. Ounaies, K.E. Wise, G. Sauti, P.T. Lillehei, J.S. Harrison, Aligned Single-Wall Carbon Nanotube Polymer Composites Using an Electric Field, *J. Polym. Sci. B Polym. Phys.* 44 (12) (2006) 1751-1762.
- [123] X.Q. Chen, T. Saito, H. Yamada, K. Matsushige, Aligning single-wall carbon nanotubes with an alternating-current electric field, *Appl. Phys. Lett.* 78 (2001) 3714-3716.
- [124] G. Chen, H. Wang, W. Zhao, Fabrication of highly ordered polymer/graphite flake composite with eminent anisotropic electrical property, *Polym. Adv. Technol.* 19 (2008) 1113–1117.
- [125] N. Romyen, S. Thongyai, P. Prasertdam, Alignment of Carbon Nanotubes in Polyimide under Electric and Magnetic Fields, *J. Appl. Polym. Sci.* 123 (2012) 3470–3475.
- [126] M.S. Kumar, S.H. Lee, T.Y. Kim, S.M. Song, J.W. Yang, K.S. Nahm, E-K Suh, DC electric field assisted alignment of carbon nanotubes on metal electrodes, *Solid-State Electronics* 47 (2003) 2075–2080.
- [127] C.A. Martin, J.K.W. Sandler, A.H. Windle, M-K Schwarz, W. Bauhofer, K. Schulte, M.S.P. Shaffer, Electric field-induced aligned multi-wall carbon nanotube networks in epoxy composites, *Polymer* 46 (2005) 877–886.
- [128] G.H. Kim, Y.M. Shkel, Polymeric composites tailored by electric field, *J. Mater. Res.*, 19 (4) (2004) 1164-1174.
- [129] R.B. Ladani, S. Wu, A.J. Kinloch, K. Ghorbani, J. Zhang, A.P. Mouritz, C.H. Wang, Improving the toughness and electrical conductivity of epoxy nanocomposites by using aligned carbon nanofibers, *Composites Science and Technology* 117 (2015) 146-158.

- [130] Wang H, Zhang H, Zhao W, Zhang W, Chen G, “Preparation of polymer/oriented graphite nanosheet composite by electric field-inducement”, *Compos. Sci. Technol.* 68 (2008) 238–243.
- [131] S. Wu, R.B. Ladani, J. Zhang, E. Bafekrpour, K. Ghorbani, A.P. Mouritz, A.J. Kinloch, C.H. Wang, Aligning multilayer graphene flakes with an external electric field to improve multifunctional properties of epoxy nanocomposites, *Carbon* 94 (2015) 607–618.
- [132] American Society for Testing and Materials, Standard Test Method for Mode I Interlaminar Fracture Toughness of Unidirectional Fiber-Reinforced Polymer Matrix Composites ASTM D5528-13 (2013).
- [133] M.Y. He, A.W. Hutchinson, Asymmetric Four-Point Crack Specimen, *J. Appl. Mech.-T. ASME* 67 (2000) 207-208.
- [134] S.H.Cheng, C.T. Sun, Size-Dependent Fracture Toughness of Nanoscale Structures: Crack-Tip Stress Approach in Molecular Dynamics, *J. Nanomech. Micromech* 4 (2014) A4014001 1-8.
- [135] J.G. Williams, *Fracture mechanics of polymers*, Ellis Horwood Ltd., London, 1984.
- [136] T. Hobbiebrunken, B. Fiedler, M. Hojo, M. Tanaka, Experimental determination of the true epoxy resin strength using micro-scaled specimens, *Composites Part A* 38 (2007) 814–818.
- [137] A.C.T. Van Duin, S. Dasgupta, F. Lorant, W.A. Goddard, ReaxFF: A reactive force field for hydrocarbons, *J. Phys. Chem. A* 105(41) (2001) 9396-9409.
- [138] S. Roy, A. Srivastav, Multiscale Modeling of Progressive Failure in Polymer Nanocomposites Using Nanaoscale Informed Damage Mechanics, *Mechanics of Advanced Materials and Structures* (2015) doi: 10.1080/15376494.2015.1101513.
- [139] M. Paley, J. Aboudi, Micromechanical analysis of composites by the generalized cell model, *Mech Mat* 14 (1992) 127-139.
- [140] J. Aboudi, Micromechanical Analysis of Thermo-Inelastic Multiphase Short-Fiber Composites, *Composites Engineering* 5 (7) (1995) 839-850.
- [141] S.M. Arnold, T.E. Wilt, A.F. Saleeb, M.G. Castelli, An Investigation of Macro and Micromechanical Approaches for a Model MMC System, *NASA CP 19117 II* (1993) 52.1-52.12.
- [142] S.M. Arnold, B.A. Bednarczyk, T.E. Wilt, D. Trowbridge, *Micromechanics Analysis Code with Generalized method of cells (MAC/GMC) User Guide Version 3.0*, NASA/TM 1999-209070 (1999).
- [143] G.M. Odegard, T.S. Gates, K.E. Wise, C. Park, E.J. Siochi, Constitutive modeling of nanotube–reinforced polymer composites, *Compos. Sci. Technol.* 63 (11) (2003) 1671-1687.

## APPENDIX

### A. Constant boundary condition solution

Assume,

$$C_H(z, T) = 1 + v(z, T) \quad (\text{A.1})$$

The initial and boundary conditions can be written as,

$$C_H(0, T) = C_H(2L, T) = 1, \quad C_H(z, 0) = C_{in} \quad (\text{A.2})$$

The reduced governing equation (11) can then be written as,

$$\frac{\partial v}{\partial T} = \frac{\partial^2 v}{\partial z^2} \quad (\text{A.3})$$

$$\begin{aligned} v(z, 0) &= C_{in} - 1 \\ v(0, T) &= v(2L, T) = 0 \end{aligned} \quad (\text{A.4})$$

Hence,  $v(z, T)$  is evaluated by solving the above equation,

$$v(z, T) = \frac{2}{\pi} (1 - C_{in}) \sum_{n=1}^{\infty} \frac{((-1)^n - 1)}{n} e^{-\frac{n^2 \pi^2 T}{4L^2}} \sin \frac{n\pi z}{2L} \quad (\text{A.5})$$

$C_H(z, T)$  can now be expressed as,

$$C_H(z, T) = 1 + \frac{2}{\pi} (1 - C_{in}) \sum_{n=1}^{\infty} \frac{((-1)^n - 1)}{n} e^{-\frac{n^2 \pi^2 T}{4L^2}} \sin \frac{n\pi z}{2L} \quad (\text{A.6})$$

**B. Time varying Prony series boundary condition solution**

Assume

$$\hat{C}(z, T; \beta_r) = u(z, T) + w(z, T; \beta_r) \quad (\text{B.1})$$

The initial and boundary conditions can be written as,

$$\begin{aligned} \hat{C}(0, T) = \hat{C}(2L, T) &= (1 - e^{-\beta_r t(T)}) \\ \hat{C}(z, 0) &= C_{in} \end{aligned} \quad (\text{B.2})$$

Where,

$$\begin{aligned} \frac{\partial u}{\partial T} &= \frac{\partial^2 u}{\partial z^2} \\ u(0, T) = u(2L, T) &= 0 \\ u(z, 0) &= C_{in} \end{aligned} \quad (\text{B.3})$$

And,

$$\begin{aligned} \frac{\partial w}{\partial T} &= \frac{\partial^2 w}{\partial z^2} \\ w(0, T) = w(2L, T) &= (1 - e^{-\beta_r \sum_{m=0}^M p_m T^m}) = \phi(T) \\ w(z, 0) &= 0 \end{aligned} \quad (\text{B.4})$$

Solution to  $u(z, T)$  is exactly similar to  $v(z, T)$  in Appendix A.

$$u(z, T) = \frac{2}{\pi} (-C_{in}) \sum_{n=1}^{\infty} \frac{((-1)^n - 1)}{n} e^{-\frac{n^2 \pi^2 T}{4L^2}} \sin \frac{n\pi z}{2L} \quad (\text{B.5})$$

$w(z, T; \beta_r)$  is evaluated using the Duhamel's Integral

$$w(z, T; \beta_r) = \int_0^T \phi(\lambda) \left[ \frac{\partial F_1(z, T - \lambda)}{\partial T} + \frac{\partial F_2(z, T - \lambda)}{\partial T} \right] d\lambda \quad (\text{B.6})$$

Where,

$$\begin{aligned}
F_1(z, T - \lambda) &= 1 - \frac{z}{2L} - \frac{2}{\pi} \sum_{n=1}^{\infty} \frac{1}{n} e^{-\frac{n^2 \pi^2 (T - \lambda)}{4L^2}} \sin \frac{n\pi z}{2L} \\
F_2(z, T - \lambda) &= \frac{z}{2L} + \frac{2}{\pi} \sum_{n=1}^{\infty} \frac{1}{n} (-1)^n e^{-\frac{n^2 \pi^2 (T - \lambda)}{4L^2}} \sin \frac{n\pi z}{2L}
\end{aligned} \tag{B.7}$$

Thus,

$$w(z, T; \beta_r) = -\frac{\pi}{2L^2} \sum_{n=1}^{\infty} n((-1)^n - 1) e^{-\frac{n^2 \pi^2 T}{4L^2}} \sin \frac{n\pi z}{2L} \int_0^T e^{-\frac{n^2 \pi^2 \lambda}{4L^2}} \phi(\lambda) d\lambda \tag{B.8}$$

Evaluation of  $\int_0^T e^{-\frac{n^2 \pi^2 \lambda}{4L^2}} \phi(\lambda) d\lambda$  is done by breaking the integral into 2 parts,

$$\frac{4L^2}{n^2 \pi^2} \left( e^{-\frac{n^2 \pi^2 T}{4L^2}} - 1 \right) - \int_0^T e^{-\beta_r \sum_{m=0}^{N'} p_m' \lambda^m} d\lambda$$

Where,

$$\begin{aligned}
p_m' &= p_m, m \neq 1 \\
p_1' &= p_1 - \frac{n^2 \pi^2}{4L^2 \beta_r}
\end{aligned}$$

If we denote  $I(T) = \int_0^T e^{-\beta_r \sum_{m=0}^{N'} p_m' \lambda^m} d\lambda$

And assume,

$$\begin{aligned}
\sum_{m=0}^{N'} p_m' \lambda^m &= x \\
\sum_{m=1}^{N'} m p_m' \lambda^{m-1} d\lambda &= dx
\end{aligned} \tag{B.9}$$

Thus the equation is simplified to,

$$I(T) = T e^{-\beta_r \sum_{m=0}^{N'} p_m ' T^m} + \beta_r \int_{p_o'}^{\sum_{m=0}^{N'} p_m ' T^m} e^{-\beta_r x} \lambda(x) dx \quad (\text{B.10})$$

An expression for  $\lambda(x)$  is required, for the full solution of this problem. Comparison of Equation (B.10) with Equation (13) indicates that  $\lambda$  can be expressed as,

$$\lambda(x) = D_o ' x + \sum_{k=1}^N D_k ' \left( x + \frac{1}{\beta_k} (e^{-\beta_k x} - 1) \right) \quad (\text{B.11})$$

Where  $D_k ' \neq D_k$ .

Equation (B.11) can then be solved to obtain,

$$\begin{aligned} I(T) &= \int_0^T e^{-\beta_r \sum_{m=0}^{N'} p_m ' \lambda^m} d\lambda \\ &= T e^{-\beta_r \sum_{m=0}^{N'} p_m ' T^m} - \frac{1}{\beta_r} \left\{ e^{-\beta_r \sum_{m=0}^{N'} p_m ' T^m} \left( 1 + \beta_r \sum_{m=0}^{N'} p_m ' T^m \right) - e^{-\beta_r p_o} (1 + \beta_r p_o) \right\} \sum_{k=0}^N D_k ' + \\ &e^{-\beta_r \sum_{m=0}^{N'} p_m ' T^m} \left\{ \sum_{k=1}^N \frac{D_k '}{\beta_k} \left( 1 - \frac{e^{-\beta_k \sum_{m=0}^{N'} p_m ' T^m}}{\left( \frac{\beta_k}{\beta} + 1 \right)} \right) \right\} - e^{-\beta_r p_o} \left\{ \sum_{k=1}^N \frac{D_k '}{\beta_k} \left( 1 - \frac{e^{-\beta_k p_o}}{\left( \frac{\beta_k}{\beta} + 1 \right)} \right) \right\} \end{aligned} \quad (\text{B.12})$$

Substituting  $I(T)$ ,  $\hat{C}(z, T; \beta_r)$  can be finally written combining  $u(z, T)$  and  $w(z, T; \beta_r)$

$$\begin{aligned} \hat{C}(z, T; \beta_r) &= -\frac{2C_{in}}{\pi} \sum_{n=1}^{\infty} \frac{((-1)^n - 1)}{n} e^{-\frac{n^2 \pi^2 T}{4L^2}} \sin \frac{n\pi z}{2L} - \\ &\frac{\pi}{2L^2} \sum_{n=1}^{\infty} n((-1)^n - 1) e^{-\frac{n^2 \pi^2 T}{4L^2}} \sin \frac{n\pi z}{2L} \left[ \frac{4L^2}{n^2 \pi^2} \left( e^{-\frac{n^2 \pi^2 T}{4L^2}} - 1 \right) - I(T) \right] \end{aligned} \quad (\text{B.13})$$